Investigation of Photon Condensation in a Four-Site Lattice Unit Cell

Dissertation
zur
Erlangung des Doktorgrades (Dr. rer. nat.)
der
Mathematisch-Naturwissenschaftlichen Fakultät
der
Rheinischen Friedrich-Wilhelms-Universität Bonn

von
Andreas Redmann
aus
Bonn

Bonn 2025

Angefertigt mit Genehmigung der Mathematisch-Naturwissenschaftlichen Fakultät der Rheinischen Friedrich-Wilhelms-Universität Bonn

Gutachter/Betreuer: Prof. Dr. Martin Weitz
Gutachter: Prof. Dr. Daqing Wang

Tag der Promotion: 16.06.2025
Erscheinungsjahr: 2025

Abstract

Since the first experimental realization of Bose-Einstein condensation in ultracold, dilute atomic gases in 1995, a broad research field exploring the physics of various intriguing quantum phenomena has developed. The Bose-Einstein condensate is a collective state occupied by many thousand atoms, forming a giant, coherent matter wave, which is formed due to quantum statistics and makes quantum effects observable at the macroscopic scale. One application of atomic Bose-Einstein condensates widely studied is to load them into periodic lattice potentials, mimicking the highly ordered crystal structure in solids. Effects as Bloch oscillations or the Mott-insulator transition known from solid state theory can be investigated in a very clean and highly controllable experimental environment.

Apart from material particles, Bose-Einstein condensation can also be realized with gases of photons or photon-like quasiparticles in highly reflective microresonators. However, in contrast to atoms, where thermalisation is achieved by contact interactions, photonic condensates need to be coupled to a material component to exchange energy and thereby reach thermal equilibrium. The radiative coupling to a fluorescent dye solution inside the microcavity, where the broadband absorption and emission coefficients are connected by a Boltzmann-like frequency scaling, can provide such a thermalisation mechanism for photons. The short spacing of the cavity mirrors restricts the longitudinal mode number and provides a well-defined low energy cutoff. The potential energy of trapped, two-dimensional photon gases in the transverse direction is determined by the local optical cavity length, so that the trapping potential can be engineered via surface structuring of the cavity mirrors. In this way variable potentials can be provided, where the corresponding ground states can be directly populated by photon condensation upon reaching a critical photon number in the cavity.

The present thesis investigates Bose-Einstein condensation of photons into the ground state provided by a square lattice potential in the form of a unit cell with four sites, which is imprinted onto one of the cavity mirrors using a static structuring technique. The lattice structure is surrounded by a shallow harmonic potential, to provide a suitable density of states such that a Bose-Einstein condensate can exist. The eigenstates of the trapping potential are thoroughly characterized numerically as well as experimentally by selectively exciting the individual states and analysing the spectral photon distribution. Spatial and spectral photon distributions are recorded for different total photon numbers in the dye microcavity and good agreement with theoretical Bose-Einstein distributions at room temperature is found. It is verified that the condensate is indeed formed in the delocalized ground state of the lattice potential and the condensate is probed for phase coherence between lattice sites in a Mach-Zehnder type, multi-path interferometer. Remaining small deviations between the experiment and the theoretical expectations in terms of the precise photon distributions, photon numbers and finite saturation of the excited states are analysed and explained by taking into account the driven-dissipative nature of the microcavity environment. The experiments are performed in a regime where cavity loss and photon reabsorption occur on a comparable timescale. The rates of these competing processes can be experimentally tuned by varying the cavity cutoff. Close to equilibrium conditions can be obtained, when photon reabsorption is much faster than the loss of photons from the cavity, which corresponds to the regime of good thermalisation. In further work carried out in this thesis, the pump power required to reach the threshold for condensation or lasing-like behaviour is investigated theoretically and experimentally as a function of the cavity cutoff wavelength. It is found for the experimental parameters, that the cutoff wavelength at which the pump threshold reaches its minimum value is almost identical to the point, where the absorption rate of photons is the same as the cavity loss rate, i.e. at the crossover between condensation and lasing-like behaviour.

Publications

Parts of this work have been published:

- A. Redmann, C. Kurtscheid, N. Wolf, F. Vewinger, J. Schmitt, and M. Weitz, *Bose-Einstein Condensation of Photons in a Four-Site Quantum Ring*, Physical Review Letters **133**, 093602 (2024)
  DOI: `https://doi.org/10.1103/PhysRevLett.133.093602`

Other publications related to the work in this thesis:

- C. Kurtscheid, D. Dung, A. Redmann, E. Busley, J. Klaers, F. Vewinger, J. Schmitt, and M. Weitz, *Realizing Arbitrary Trapping Potentials for Light via Direct Laser Writing of Mirror Surface Profiles*, Europhysics Letters **130**, 5 (2020)
  DOI: `https://doi.org/10.1209/0295-5075/130/54001`
- E. Busley, L. Espert Miranda, A. Redmann, C. Kurtscheid, K. K. Umesh, F. Vewinger, M. Weitz, and J. Schmitt, *Compressibility and the Equation of State of an Optical Quantum Gas in a Box*, Science **375**, 1403-1406 (2022)
  DOI: `https://doi.org/10.1126/science.abm2543`
- C. Kurtscheid, A. Redmann, F. Vewinger, J. Schmitt, and M. Weitz, *Thermodynamics and State Preparation in a Two-State System of Light*, arXiv preprint, arXiv:2411.14838 (2024)
  DOI: `https://doi.org/10.48550/arXiv.2411.14838`

Contents

1 Introduction **1**

2 Theoretical Principles **3**
2.1 The Photon Gas . . . 3
2.2 Photons in a High Finesse Dye-Filled Microcavity . . . 5
2.3 Photon Dispersion in Optical Microcavities . . . 10
2.4 Non-Equilibrium Model of Photon Condensation . . . 15
2.5 Creation of Potentials for Photon Gases . . . 23

3 Experimental Setup **27**
3.1 Pumping of Dye Molecules . . . 27
3.2 Analysis of the Microcavity Emission . . . 28
3.3 Measurement of Spatial and Spectral Density Distributions . . . 29
3.4 Average Photon Number in the Cavity . . . 33

4 Condensation Threshold **35**
4.1 Pump Threshold for Photon Condensation . . . 35
4.2 Measurement of the Pump Threshold . . . 38

5 A Four-Site Lattice Unit Cell for Photons **43**
5.1 Bosons in Periodic Potentials . . . 43
5.2 A Four-Site Unit Cell for Experiments with Photons . . . 47
5.3 Creation and Numerical Characterization of the Surface Structure . . . 48
5.4 Experimental Characterization of the Trapping Potential . . . 50
5.5 Numerical Fit Functions for the Photon Density Distributions . . . 53

6 Photon Condensation in a Four-Site Lattice Unit Cell **57**
6.1 Experimental Parameters . . . 57
6.2 Spatial Photon Distributions . . . 58
6.3 Broadband Spectral Photon Distributions . . . 60
6.4 Small Photon Number Distributions . . . 61
6.5 Photon Population per State . . . 63
6.6 Phase Coherence of the Microcavity Emission . . . 66

7 Conclusion and Perspective **69**

A Appendix **73**
A.1 Connection Between Pump Rate and Pump Power . . . 73
A.2 Emission Rate into the Cavity - Fermi's Golden Rule . . . 73

References **77**

Chapter 1 | Introduction

Interaction between light and matter is an omnipresent phenomenon in our daily lives. The appearance of objects to the human eye for example, is determined by absorption and reflection of light of certain colours. Sunlight is the basis of photosynthesis when absorbed by plants, it can be converted into electricity via solar panels and it significantly impacts the seasonal and long term climate. Smartphone displays use pixel arrays of organic light emitting diodes to generate light and light ranging technologies are crucial for self-driving cars.

Many technologies known today are the result of long-time ongoing research of light-matter interaction, which has fascinated humankind since the times of ancient Greece, when philosophers speculated about the principles of vision being due to light rays emitted from the eye. During the era of Renaissance, Kepler revised this concept and argued, that light rays are scattered from objects into all directions, of which some are captured and focused to an image by the eye's pupil. He would, together with the work of Snell, lay out the principles of modern optics by explaining the refraction of light. Young's double-slit experiment later demonstrated that light behaves as a wave and soon afterwards, in 1818, Fresnel developed a theory that could explain interference and diffraction of light. After Maxwell unified electricity and magnetism, showing that light is an electromagnetic wave, major advances toward theories and revolutionary technologies followed in the 1900s. The invention of the laser in 1960 [1] opened up unprecedented opportunities for precision spectroscopic studies of atomic and molecular structure. Laser radiation is also important for the manipulation of the external degrees of freedom of atoms, allowing e.g. for laser cooling, and further evaporative cooling, which culminated in the observation of Bose-Einstein condensation (BEC) in dilute alkali vapours [2, 3]. BEC is an effect leading to the macroscopic ground state accumulation of massive particles below a critical temperature predicted by Einstein [4], for which work of Bose on the quantum statistics of massless particles (photons) [5] was fundamental. Bose-Einstein condensation is accompanied by the emergence of coherence among the condensing particles, so that quantum effects can be observed at the macroscopic scale.

After the first demonstration, BEC was subsequently realized for many different kinds of atoms [6, 7], composite molecules of fermionic atomic pairs [8] and other exotic species like exciton-polaritons in microcavities [9], which are strongly coupled, hybrid light-matter quasiparticles. However, despite Bose's idea emanated from the statistics of photons, BEC of pure photons remained elusive for a long time, since photons can not thermalize by contact interaction. This is where light-matter interaction is required so that a matter component can mediate the thermalisation by radiative coupling to the photon gas. In 2010, BEC of photons in two dimensions was then realized for the first time [10, 11]. The experiments are carried out at room temperature in a dye-filled microcavity, where the photon density can be controlled, independently from the temperature, by an external pump source, and thermalisation is achieved by processes of photon absorption and emission via the dye molecules [12]. In contrast to atomic BECs, the coupling of photons to a thermal bath of photo-excitable dye molecules leads to grand-canonical statistical conditions for the photon BEC [13], which appears in fluctuations of the photon number. The statistical and thermodynamic properties were thoroughly characterized [14–16] and experiments were soon also performed in other laboratories [17, 18]. The research field was also successfully extended to other platforms. Thermalisation and BEC of photons was studied in erbium-doped fibres [19, 20] and recently photon BEC was reported in an optically pumped semiconductor quantum well microcavity [21] as well as, particularly promising from a technological point of view, in a conventional electrically pumped vertical cavity surface emitting laser [22].

Atomic BECs are typically generated in magnetic or optical dipole traps after which they can be adiabatically loaded into traps of different geometry. In particular, a lot of interest has been devoted to periodic potentials [23], mimicking the crystalline structure of solids, which are generated by interfering laser beams [24]. The physics of bosons in lattice structures features a rich plethora of phenomena, for example the transition between a superfluid and a Mott-insulating phase [25], and cold atoms in optical lattices are also used in the search for the mechanism of high temperature superconductivity. Other experiments implemented Josephson junctions to investigate the Josephson DC and AC effects with two atomic BECs separated by a weak potential barrier [26, 27] or by applying a potential gradient to atoms confined to a one-dimensional lattice [28]. Josephson junctions can serve as extremely sensitive sensors for the measurements of tiny voltages and they are also highly relevant as qubits for quantum computing [29]. The Josephson effects were also studied for polaritons in naturally occurring disorder potential wells [30] or in micropillars, etched into the microcavity [31]. Other research investigated Bloch-oscillations in one-dimensional optical lattices [32] or waveguide arrays [33]. For photon BEC experiments, reversible periodic lattice structures can be generated by admixing a thermosensitive polymer into the dye solution. In this way, a direct control of the trapping potential is obtained upon local heating of the polymer with a focused laser beam [34]. Static potentials can instead be imprinted by microstructuring the mirror surfaces before assembling the microcavity [35, 36]. The preparation of trapping potentials highlights a fundamental difference between photonic and atomic condensates. While the trapping geometry can be modified during the coherence and holding times of cold atoms, photonic condensates are directly generated in complex ground states with only minor adjustability of the potential geometry on the time scale of a few 100 ns [34]. The static mirror structuring technique was successfully employed to study photon BEC in the symmetric superposition ground state of a double well potential [37] and, in conjunction with the reversible heat-based polymer method, to demonstrate arrays of controllable Josephson junctions [38].

Naturally, photonic condensates occur in a driven-dissipative environment and are thus in a dynamical state where losses are compensated by pumping [39]. The successful thermalisation of light requires that thermalisation by radiative contact to the thermalisation medium is much faster than losses from the cavity. How thermalisation is obtained has been thoroughly studied under quasi-continuous pumping and for pulsed excitation by following the time evolution of the photon distribution [10, 40]. Other than analysing the photon distribution in the cavity, an unbiased indicator to assess whether the experimental parameters support the efficient thermalisation of photons, is obtained by identifying the cavity cutoff of minimum pump power required to reach the condensation threshold. The timescales of the competing processes of cavity losses and photon reabsorption can be tuned by varying the cutoff of the microcavity, which allows to change between the regimes of good and poor thermalisation. The first part of the thesis focuses on this aspect and presents an analysis of the threshold pump power, which allows to identify the transition point between the two regimes. The second part of the thesis is dedicated to the design and characterization of a lattice unit cell for photons with four sites. A photon BEC is created in the lattice structure with the ground state energy set close to the crossover point between good and poor thermalisation conditions, and the photon gas is analysed regarding its characteristic properties of thermal equilibrium, with a few discernible features, which are attributed to the open nature of the photon-cavity environment.

Chapter 2 | Theoretical Principles

This chapter introduces the main concepts of Bose-Einstein condensation (BEC) of an ideal gas. The relevant processes related to electronic transitions in fluorescent dye molecules are explained, which provide the basis for a thermalisation mechanism of photons at a fixed temperature with independently adjustable photon density. The platform of a dye-filled microcavity is presented, which enables the successful realization of photon BEC into a ground state at non-zero energy. The example of photon BEC in a harmonic oscillator potential is discussed and a general method to study the eigenmodes of a custom shaped cavity geometry is introduced. The chapter concludes with a description of the dye microcavity system in terms of driven-dissipative rate equations and the basic principles of a permanent mirror structuring technique, used in this work to tailor a potential structure with the ground state provided by a lattice unit cell with four sites.

2.1 | The Photon Gas

The physical system of a light field confined to an empty container with volume V and the walls coupled to an outside reservoir at temperature T is referred to as a photon gas. From a thermodynamic point of view, such a collection of photons can be treated as a conventional gas of particles. However, unlike atomic gases, for which equilibrium is established by particle-particle interactions, the intrinsically non-interacting nature of light necessitates a thermal contact to matter, so that thermal equilibrium in the radiation field can be achieved [41]. The most common example of a photon gas in thermal equilibrium is blackbody radiation, where a thermal contact is established via absorption and emission of photons in the container walls. Blackbody radiation however behaves fundamentally differently from atomic gases. In particular, the photon number N is not conserved, as photons can be thermally created or destroyed in order to maintain the dynamical balance between absorption and emission in the container.

In equilibrium, all net flows of energy or particles, which are exchanged continuously between the light field and the matter in thermal contact, come to rest. Building on this principle, the container can be modified by replacing the walls with highly reflective mirrors and filling it with a material, which exhibits broadband ground and excited states. A thermalisation mechanism for light is then obtained by absorption and emission processes on this material and, most importantly, the photon number can be decoupled from the temperature so that N and T are independently tunable. In this way, the photon gas becomes formally equivalent to an ideal gas of material particles and Bose-Einstein condensation becomes possible.

2.1.1 | The Ideal Bose Gas

The ideal Bose gas is a quantum mechanical system made up of many non-interacting particles, which is characterized by a total symmetric wave function w.r.t. the exchange of any two quantum numbers (e.g. momentum, position or spin projection of two particles). This is a direct consequence of the integer spin of bosons. For a Bose gas at temperature T in a volume V, the average population of a quantum state at energy ϵ is given by the Bose-Einstein distribution [5]

$$n_{\mu,T}(\epsilon) = \frac{g(\epsilon)}{e^{\frac{\epsilon-\mu}{k_\mathrm{B}T}} - 1}\,, \tag{2.1}$$

with the level degeneracy $g(\epsilon)$, the thermal energy $k_\mathrm{B}T$ and the chemical potential μ, which is defined as the change of the internal energy U related to a change in the particle number, i.e. $\mu = (\mathrm{d}U/\mathrm{d}N)_{V,T}$ [42]. In a closed system of constant volume and known energy levels, the chemical potential is implicitly determined by the total particle number N and the temperature T via the relation

$$N = \sum_{\epsilon} n_{\mu,T}(\epsilon)\,. \tag{2.2}$$

In order to always have positive, non-diverging particle numbers, the chemical potential is required to be smaller than the lowest energy in the system, i.e. $\mu < \epsilon_0$, with the ground state energy ϵ_0. Without loss of generality, one can set $\epsilon_0 = 0$. For high temperatures or small particle numbers, the Bose-Einstein distribution becomes the Boltzmann distribution

$$|\mu(N,T)|/k_BT \gg 1 \quad \longrightarrow \quad n_{\mu,T}(\epsilon) = g(\epsilon)\,e^{-\frac{\epsilon-\mu}{k_\mathrm{B}T}}\,, \tag{2.3}$$

which is the regime where quantum effects are of little importance and the system is properly described as a classical gas of particles.

2.1.2 | Bose-Einstein Condensation

A unique feature of bosons and their statistical nature is, that there is no fundamental limit for the maximum number of particles occupying a single quantum state. This characteristic is especially pronounced at small temperatures, where it leads to the coherent amplification of the ground state occupation through bosonic stimulation [43], resulting in the quantum mechanical phase transition to Bose-Einstein condensation. Assume that the temperature is continuously lowered for a gas of bosons in thermal equilibrium with particle number N. Correspondingly, the chemical potential continuously increases, i.e. it becomes less negative, which makes the particles preferentially occupy energy states of lower energy. Once the temperature is below a system specific critical temperature, the particles start to accumulate in the ground state. This marks the phase transition to the Bose-Einstein condensate.

Interestingly, this effect occurs at non-zero temperature, which is due to the quantum nature of indistinguishable particles and the constructive interference of the different wave packets. The transition (or critical) temperature can be obtained by calculating the (critical) particle number in all excited states by setting $\mu = 0$. For a continuum of energy states with separation $\Delta\epsilon \ll k_\mathrm{B}T$, the level degeneracy can be replaced by a general density of states $g(\epsilon) = C_\alpha\,\epsilon^{\alpha-1}$ [44], that varies with a power of the energy where C_α is a constant. The excited state particle number is then found from the integral

$$N_\mathrm{c} = N_\mathrm{exc}(\mu = 0, T_\mathrm{c}) = C_\alpha \int_{\epsilon>0}^{\infty} \frac{\epsilon^{\alpha-1}}{e^{\epsilon/k_\mathrm{B}T_\mathrm{c}} - 1}\,\mathrm{d}\epsilon = C_\alpha \Gamma(\alpha)\zeta(\alpha)(k_\mathrm{B}T_\mathrm{c})^\alpha\,. \tag{2.4}$$

Here, $\Gamma(\alpha)$ and $\zeta(\alpha)$ are the gamma and Riemann zeta function respectively. For Bose-Einstein condensation to occur at a finite temperature, the critical particle number must not be infinite, which crucially depends on the density of states and is thus determined by the dimensionality and confinement of the gas. One finds that Bose-Einstein condensation can exist for $\alpha > 1$, i.e. when the density of states increases with energy. Equation (2.4) can be considered as a relation that defines a critical temperature for constant particle number or a critical particle number for constant temperature. While atomic Bose-Einstein condensates are realized by cooling the gas to near absolute zero temperature, the extremely small effective photon mass in microcavity experiments allows to achieve the required densities for Bose-Einstein condensation of photons already at room temperature.

2.1.3 | Blackbody Radiation

Thermal light that is emitted from a medium that can absorb and emit radiation over all frequencies, is called blackbody radiation. The most famous example of blackbody radiation is arguably the isotropically distributed cosmic microwave background over all space at a temperature of 2.7 K. In a laboratory, blackbody radiation can be produced for example from a small opening of a cavity with absorbing and emitting walls at temperature T. The spectral photon density distribution is given by Planck's law [45]

$$n(\omega) = \frac{\omega^2}{\pi^2 c^3} \frac{1}{e^{\hbar\omega/k_\mathrm{B}T} - 1} \,. \tag{2.5}$$

Importantly, the photon density of blackbody radiation is determined exclusively by the temperature, which is due to the vanishing chemical potential of the photon gas. This is because the internal energy remains unchanged despite the presence of thermal emission and absorption events, i.e. $\mathrm{d}U = \mu_\gamma \, \mathrm{d}N_\gamma = 0$ with $\mathrm{d}N_\gamma \neq 0$, so that $\mu_\gamma = 0$. Following Planck's empirically found radiation law, Albert Einstein later worked out the physical grounds by imposing the balance between absorption and emission (spontaneous and stimulated) processes in the walls of the cavity [46]. The ratio between the equilibrium populations of two energy levels $|2\rangle$ and $|1\rangle$ separated by $\hbar\omega$ is given by the Boltzmann factor

$$\frac{N_2}{N_1} = \frac{1}{e^{\hbar\omega/k_\mathrm{B}T} - 1} \tag{2.6}$$

and together with the density of states in the three dimensional cavity, $g(\omega) = \omega^2/\pi^2 c^3$, the result is Planck's law. Einstein's derivation is based however on the assumption of a collection of atoms in the cavity walls that are ideal two-level systems, which then requires, that the absorption and emission cross sections are equal, i.e. $\sigma_\mathrm{a}(\omega) = \sigma_\mathrm{e}(\omega)$. The situation is different for materials with separate bands of energy states that are subject to an internal thermalisation mechanism and thus exhibit broadband absorption and emission spectra. Coupling the photon gas to such media can allow for a non-zero chemical potential for photons [47, 48]. A vanishing chemical potential is thus not a general property of a photon gas, but it is determined by the environment that is interacting with the radiation field.

2.2 | Photons in a High Finesse Dye-Filled Microcavity

In contrast to a cavity with absorbing and emitting walls at temperature T, one could instead think of a cavity with perfectly reflecting walls. This cavity however merely serves as a container for light and it can not thermally interact with photons trapped inside the cavity. Achieving equilibrium in the radiation field then relies on another matter component, which is assumed to homogeneously fill the cavity and which is resonantly coupled to the photons by absorption and emission. This material should be characterized by a spectral gap, such that photons of smaller energy, for example ambient

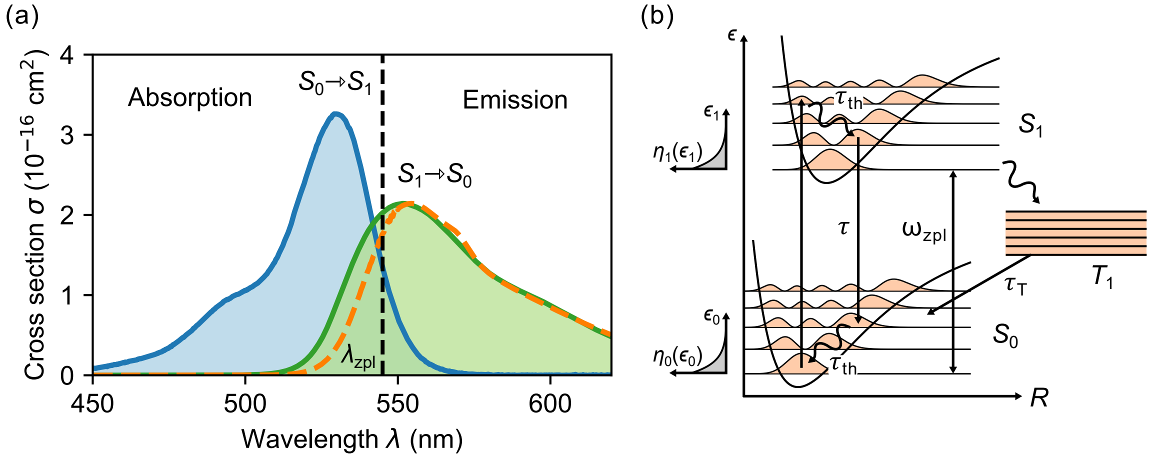

Figure 2.1: **(a)** Cross sections in Rhodamine 6G for absorption (blue) and emission (green), as provided from the PhotochemCAD database[1]. The two middle peaks are at the energies corresponding to the strongest transitions between the S_0 and S_1 electronic states. The orange dashed curve gives the calculated emission cross section from the Kennard-Stepanov relation (eq. (2.11)) with $\lambda_{zpl} = 545\,\mathrm{nm}$. **(b)** Jablonski energy diagram of the electronic level structure in organic molecules including a sketch of the rovibronic substructure. S-states are singlet states and T_1 is a triplet state. According to the Franck-Condon principle optical transitions are vertical lines, i.e. they occur at fixed internuclear distance R.

blackbody radiation, can not interact with it. It is thus a non-thermal, luminescent light source and photons in the cavity are generated by an external pumping mechanism. While in principle all materials with electronic transitions between discrete energy levels exhibit this property, the interesting ones from the perspective of establishing thermal equilibrium in the photon gas, are materials involving quasi-continuous and well-separated energy bands, like a lot of semiconductors or fluorescent dye molecules. The principle of achieving a thermalized photon gas with tunable photon number inside a dye-filled high finesse microcavity, independent from the temperature, will be introduced in the following sections.

2.2.1 | Optical Properties of Organic Dyes

Organic dyes are carbon based molecules that exhibit several electronic energy levels, which are nearly continuous bands composed of closely spaced rotational and vibrational (rovibronic) sub-levels [49]. The electronic singlet ground state S_0 is coupled to the first excited singlet state S_1 by transitions between these manifolds of sub-levels in or near the visible spectral range. The spectral width of the absorption and emission bands reflects the width of the homogeneously broadened singlet states and is typically about 50 THz in bandwidth, as shown in fig. 2.1(a) for Rhodamine 6G, which is one of the most widely used organic dyes, for lasers as well as for photon condensates.

Fig. 2.1(b) shows a simplified energy diagram of the two singlet states. The energy separating the rovibronic ground states of the two bands is given by $\hbar\omega_{zpl}$, with the zero-phonon line frequency ω_{zpl}. Electronic transitions between the singlet states occur on a timescale of fs, so that the position of the nuclei remain unchanged during absorption and emission of photons. This is known as the

---

[1] The data can be downloaded from the online repository at `https://omlc.org/spectra/PhotochemCAD/html/083.html` [50]. The absorption spectrum in this reference is given in terms of molar extinction coefficients ε measured in methanol, which can be converted to absorption cross sections by $\sigma_a = \varepsilon/10 \cdot \ln(10)/N_A/1.36$ [49], with Avogadro's constant N_A and the refractive index of methanol 1.36. The emission cross section is obtained from the line shape function in eq. (2.48) with a quantum yield of $\Phi = 0.95$.

Franck-Condon principle [51, 52], which implies that electronic transitions are vertical transitions in the energy diagram. Following the absorption of a photon, the excited electronic state of the molecule will typically be in one of the many available rovibronic sub-states. Frequent collisions of the excited molecule with surrounding particles now lead to a rapid relaxation and excessive excitation energy is released into the solvent bath as heat. This process of thermalisation takes place on a timescale τ_{th} on the order of a few ps [53]. As the excited state radiative lifetime (~ ns) exceeds the thermalisation time by orders of magnitude, the fluorescence photon will be emitted from an electronic state, which is denoted to be in local thermodynamic equilibrium [54]. The electron distribution function over the rovibronic sub-states with energies ϵ_1 can therefore very well be approximated by a Boltzmann distribution, i.e.

$$\eta_1(\epsilon_1) = C_1 \cdot g_1(\epsilon_1)\exp(-\epsilon_1/k_{\mathrm{B}}T) \tag{2.7}$$

with the density of states $g_1(\epsilon_1)$, a normalization factor C_1 ($\cong$ partition function) and temperature T of the dye solution [55]. After emission of the fluorescence photon, the molecule will most likely be in one of the excited rovibronic sub-levels in S_0. Photon emission therefore generally occurs at smaller frequencies compared to absorption, which is a phenomenon known as the Stokes shift [56]. The electronic ground state is now subject to the same relaxation mechanism as the excited state S_1. Correspondingly, the electron in the ground state will also be Boltzmann distributed, i.e.

$$\eta_0(\epsilon_0) = C_0 \cdot g_0(\epsilon_0)\exp(-\epsilon_0/k_{\mathrm{B}}T)\,. \tag{2.8}$$

Using these electron distribution functions, frequency dependent cross sections for stimulated emission and absorption of photons at frequency ω can be defined by

$$\sigma_{\mathrm{e}}(\omega) = \int \sigma_{\mathrm{e}}(\epsilon_1,\omega)\eta_1(\epsilon_1)\,\mathrm{d}\epsilon_1 \quad \text{and} \quad \sigma_{\mathrm{a}}(\omega) = \int \sigma_{\mathrm{a}}(\epsilon_0,\omega)\eta_0(\epsilon_0)\,\mathrm{d}\epsilon_0\,. \tag{2.9}$$

The integrals account for all possible transitions from the various sub-levels that contribute to the total cross section at frequency ω. If the ground and excited states can be described by very similar interatomic potential curves, it is reasonable to assume that the partition functions C_0, C_1 coincide [49]. Naturally, for energies ϵ_1 and ϵ_0 which are coupled by photons of frequency ω, energy conservation demands that $\epsilon_1 = \epsilon_0 + \hbar(\omega - \omega_{\mathrm{zpl}})$ and the transition cross sections have to be equal, so that

$$\sigma_{\mathrm{e}}(\epsilon_1,\omega)g_1(\epsilon_1) = \sigma_{\mathrm{a}}(\epsilon_0,\omega)g_0(\epsilon_0)\,. \tag{2.10}$$

Combining equations (2.7)-(2.10) and using $\mathrm{d}\epsilon_1 = \mathrm{d}\epsilon_0$, the obtained result is

$$\frac{\sigma_{\mathrm{e}}(\omega)}{\sigma_{\mathrm{a}}(\omega)} = \exp\left(-\frac{\hbar(\omega-\omega_{\mathrm{zpl}})}{k_{\mathrm{B}}T}\right) = \exp\left(-\frac{\hbar\delta}{k_{\mathrm{B}}T}\right), \tag{2.11}$$

with the detuning $\delta = \omega - \omega_{\mathrm{zpl}}$ of the photon frequency w.r.t. the zero-phonon line. This relation is known as the *Kennard-Stepanov relation* for fluorescent dye molecules [57–60]. The same principles however equivalently apply for other materials with homogeneously broadened energy levels that are in local thermal equilibrium with their environment, for example semiconductors [61], or solid-state media like rare-earth doped glasses [62, 63]. In fig. 2.1(a) the Kennard-Stepanov relation was employed to calculate the emission cross section of Rhodamine 6G from the measured absorption cross section, which is shown as the dashed curve overlapped with the emission spectrum. As is evident, the Kennard-Stepanov relation is very well fulfilled for wavelengths larger than 550 nm, which is the relevant spectral region for photon condensate experiments.

2.2.2 | Other Spectral Features of Organic Dyes

Fluorescent dye molecules also exhibit higher excited singlet states than S_1, which correspond to separate peaks in the absorption spectrum (not shown in fig. 2.1). Excited molecules however quickly relax to S_1 by nonradiative internal conversion, so that the emission of fluorescence photons will occur exclusively from the S_1 state [49]. According to Hund's Rule, there is an excited triplet state (state T_1 in fig. 2.1(b)) with lower energy than S_1 which can be occupied by the electron following a spin flip [64], a process called intersystem crossing which exhibits a higher likelihood in organic materials with large spin-orbit coupling. As optical transitions between triplet and singlet states are forbidden by the spin selection rule $\Delta S = 0$, the triplet state exhibits a lifetime τ_T usually orders of magnitude longer than the fluorescence lifetime ($\tau_T \approx 1\,\mu\mathrm{s}$ for Rhodamine 6G [65]). The relaxation of $T_1 \rightarrow S_0$ then predominantly occurs via radiationless intersystem crossing [66], however with a small probability, the transition can also occur radiatively, a process called phosphorescence. Despite occurring at relatively small rates ($\sim 10^6/\mathrm{s}$ [67]), the coupling of $S_1 \rightarrow T_1$ imposes severe limitations for the continuous wave operation of dye laser systems, due to the long-lived metastable triplet states which effectively reduce the available dye molecule concentration over time. While for conventional lasers with long cavities this problem is usually solved by continuously flushing fresh dye molecules through the laser cavity [68], in experiments on photon condensates with microcavities cycles of short-term illumination ($\sim 500\,\mathrm{ns}$) and small repetition rates ($\sim 50\,\mathrm{Hz}$) are used, so that the dye molecules can relax back to the electronic ground state before the experiment is repeated.

If a particular optical transition probability, which is proportional to the overlap of initial and final state electronic wave functions, is very strong in absorption, the reciprocal transition will have a large probability in emission as well. Therefore very similar features from the $S_0 \leftrightarrow S_1$ transition can be observed in the absorption and emission spectra, making them essentially a mirror-image of each other [69]. The slightly shifted potential curve of the excited electronic state towards higher values of the generalized internuclear distance R (see fig. 2.1(b)), is the reason for a shift of the absorption peak towards higher energies w.r.t. the zero-phonon line and a shift of the emission peak towards lower energies. Due to the rapid internal thermalisation, fluorescence of excited molecules occurs with a frequency spectrum independent of the exciting photon's frequency, which is known as Kasha's rule [70].

2.2.3 | Fluorescence Quantum Yield

Due to the nonradiative transitions by intersystem crossing, there are decay channels of the excited singlet state that do not result in the emission of a fluorescence photon. To quantify the percentage of excited molecules, which decay non-radiatively, it is convenient to define a fluorescence quantum yield Φ as the number of photons emitted divided by the number of photons absorbed [49]. An expression for Φ is therefore obtained by taking the ratio of the emission rate and the total decay rate. This results in

$$\Phi = \frac{\Gamma_\mathrm{r}}{\Gamma_\mathrm{r} + \Gamma_\mathrm{nr}} = \frac{\tau}{\tau_\mathrm{r}} \tag{2.12}$$

with the emission rate Γ_r, the nonradiative decay rate Γ_nr and the radiative and total lifetime of the excited singlet state τ_r and τ respectively. For Rhodamine 6G dissolved in ethylene glycol, the typical solution used for experiments on photon condensates, experimentally determined values are $\tau = 4\,\mathrm{ns}$ and $\Phi = 0.95$ [71, 72], which corresponds to a radiative decay rate of $\Gamma_\mathrm{r} = 237.5\,\mathrm{MHz}$ and a nonradiative decay rate of $\Gamma_{\mathrm{nr}} = 12.5\,\mathrm{MHz}$.

2.2.4 | Photons as an Ideal Bose Gas

Consider now a cavity with perfectly reflecting walls, filled with a Rhodamine 6G dye solution. In the presence of photons within the dye spectral bandwidth, the continuous cycles of absorption and emission can be considered as chemical reactions of the form

$$\downarrow + \gamma \leftrightarrow \uparrow , \tag{2.13}$$

where γ is a photon and $\downarrow$ ($\uparrow$) denotes a ground (excited) state molecule, respectively. In equilibrium, the internal energy remains constant in the presence of the continuing exchange of excitations in terms of photons and excited molecules, which implies

$$\mathrm{d}U = \mu_\uparrow \,\mathrm{d}M_\uparrow + \mu_\downarrow \,\mathrm{d}M_\downarrow + \mu_\gamma \,\mathrm{d}N_\gamma = 0\,, \tag{2.14}$$

with the chemical potentials of excited $\mu_\uparrow$ and ground state molecules $\mu_\downarrow$ and of photons μ_γ [48] and $M_\downarrow + M_\uparrow = M$ is the total number of molecules. The change of the photon number is directly linked to the change of the molecular state, i.e. $\mathrm{d}N_\gamma = -\mathrm{d}M_\uparrow = \mathrm{d}M_\downarrow$, so that the number of excitations is conserved. Consequently this implies that

$$\mu_\gamma = \mu_\uparrow - \mu_\downarrow \tag{2.15}$$

i.e. a non-zero chemical potential for the photons is obtained. The same conclusion can also be obtained by applying the detailed balance condition for absorption and emission (spontaneous and stimulated) with the photon number $n(\omega)$ at frequency ω, which gives

$$n(\omega)\cdot\left[\sigma_\mathrm{e}(\omega)M_\uparrow - \sigma_\mathrm{a}(\omega)M_\downarrow\right] + \sigma_\mathrm{e}(\omega)M_\uparrow \overset{!}{=} 0 \tag{2.16}$$

$$\Rightarrow n(\omega) = \frac{1}{e^{\frac{\hbar(\omega-\omega_{\mathrm{zpl}})}{k_\mathrm{B}T}}\frac{M_\downarrow}{M_\uparrow} - 1}\,, \tag{2.17}$$

where the Kennard-Stepanov relation (2.11) was used. Equating this expression to the Bose-Einstein distribution implies for the chemical potential

$$\mu_\gamma = \hbar\omega_{\mathrm{zpl}} + k_\mathrm{B}T\ln(M_\uparrow/M_\downarrow)\,, \tag{2.18}$$

so that the photon chemical potential is linked to the relative excitation level $M_\uparrow/M_\downarrow$ in the molecules [73]. In an experiment, the chemical potential and correspondingly the photon number can then be controlled by the power of an external pump source. This result illustrates, how the photon gas can formally behave like an ideal Bose gas. Thermal equilibrium in the radiation field is achieved due to the internal relaxation mechanism in the dye molecules and a tunable chemical potential is obtained due to the bandgap between the electronic singlet states and the control of the relative molecular populations in ground and excited states. It then follows, that Planck's law is a special case of the Bose-Einstein distribution, in which only thermal excitations are present in the cavity [47], such that $M_\uparrow/M_\downarrow = \exp(-\hbar\omega_{\mathrm{zpl}}/k_\mathrm{B}T)$, i.e. $\mu_\gamma = 0$.

2.2.5 | Optical Gain in Organic Dyes

Consider an ensemble of dye molecules under continuous optical pumping. If a light beam at frequency ω with intensity $I(\omega)$ passes through the dye solution, it is going to be attenuated or amplified, depending on the relative excitation level. In the generalized Lambert-Beer's law

$$\frac{\mathrm{d}\,I(\omega)}{\mathrm{d}z} = \alpha(\omega)\,I(\omega)\,, \tag{2.19}$$

with the propagation direction z, $\alpha(\omega)$ takes the role of a gain coefficient [55]. With the population densities $\rho_{\uparrow/\downarrow} = M_{\uparrow/\downarrow}/V$, where V is the overlap volume between the molecules and the light beam, this gain coefficient is defined as

$$\alpha(\omega) = \rho_\uparrow \sigma_\mathrm{e}(\omega) - \rho_\downarrow \sigma_\mathrm{a}(\omega) = \sigma_\mathrm{e}(\omega)\left[\rho_\uparrow - \rho_\downarrow \frac{\sigma_\mathrm{a}(\omega)}{\sigma_\mathrm{e}(\omega)}\right]. \tag{2.20}$$

For the incoming light beam to be amplified, stimulated emission has to overcome absorption, so the gain coefficient needs to be positive, i.e. $\alpha(\omega) > 0$. This implies for the relative excitation level

$$\frac{M_\uparrow}{M_\downarrow} > \frac{\sigma_\mathrm{a}(\omega)}{\sigma_\mathrm{e}(\omega)} = e^{\hbar(\omega-\omega_\mathrm{zpl})/k_\mathrm{B}T}\,. \tag{2.21}$$

For frequencies $\omega < \omega_\mathrm{zpl}$ this condition can be fulfilled even for $M_\uparrow < M_\downarrow$, i.e. without a net population inversion between the two electronic states, which is a direct consequence of the rapid internal thermalisation of the molecular electronic states. In terms of the photon chemical potential, amplification of the light beam implies $\mu_\gamma > \hbar\omega$ [47]. Note that the divergence of the photon number in eq. (2.17) upon insertion of this condition comes from the fact that spontaneous emission was neglected here. In a real amplifying process, μ_γ gets very close to $\hbar\omega$, but does not exceed it.

The chemical potential increases from negative energies with increasing excitation levels. For photons confined to a perfectly reflecting cavity, the occupation in the lowest energy mode will thus be the first one to be amplified, once the chemical potential approaches the energy of this cavity mode. The similarity between the coherent amplification of photons in a single cavity mode and the formation of atomic Bose-Einstein condensates through stimulated scattering [43] illustrates an analogy between lasers and BEC [74–76], despite the intrinsic non-equilibrium character of lasers. A non-equilibrium model for photon condensation, which will be presented in sec. 2.4, will allow for a more detailed differentiation between the classification of the two systems.

2.3 | Photon Dispersion in Optical Microcavities

Experimentally the highly reflecting container for light described in the previous section is realized by a high finesse microcavity composed of two closely spaced mirrors with reflectivities $R \approx 99.998\%$. Such high reflectivities are achieved by using mirrors with multilayer stacks of dielectrics with alternating refractive indices, also called Bragg reflectors. These type of mirrors are widely used because they allow for the design of customized spectral regions of ultra high reflectivity (also referred to as stop bands) [77]. Fig. 2.2(a) shows the transmission profile of the two mirror coatings used in this thesis. The short spacing of the cavity mirrors of about $L_0 \approx 1.5\,\mu\mathrm{m}$ is important because the separation of longitudinal cavity modes, the free spectral range $\Delta\nu_\mathrm{FSR}$, is inversely proportional to the cavity length by $\Delta\nu_\mathrm{FSR} = c/2\tilde{n}L_0 \approx 70\,\mathrm{THz}$, with the refractive index $\tilde{n}$ of the medium between the mirrors ($\tilde{n} \approx 1.44$ for ethylene glycol), which is comparable to the dye spectral bandwidth. Microcavities

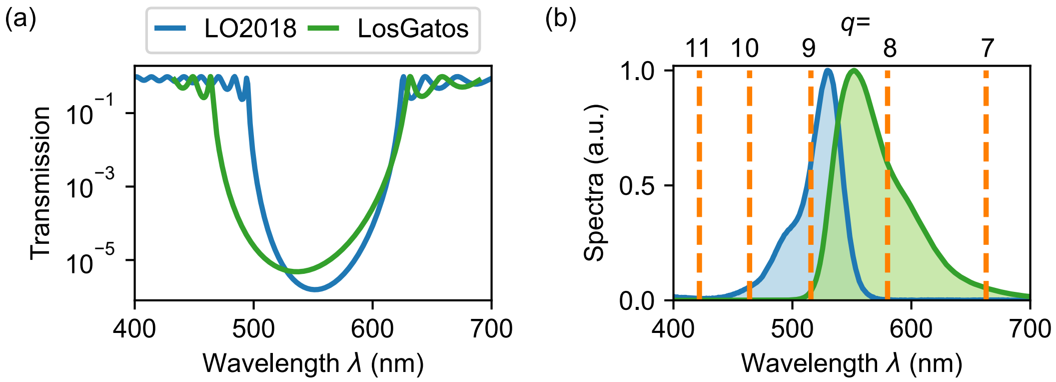

Figure 2.2: **(a)** The transmission profile of the two mirror coatings used in this thesis, as provided by the manufacturer. The coating by the company Laseroptik (*LO2018*) with the stop band centred at 550 nm is used for the experiments performed in microstructured potentials. The coating by the company Los Gatos Research (*LosGatos*) is centred at 530 nm and it is used for measurements of the pump threshold in this work. **(b)** Peak normalized absorption and emission spectra of Rhodamine 6G (cf. fig. 2.1(a)) together with the resonance wavelengths of a few longitudinal cavity modes at zero transverse momentum $k_r = 0$, which are labelled by the corresponding longitudinal mode number q. The cavity length in this example is $L_0 = 1.6\,\mu\mathrm{m}$.

can therefore be tuned such that only one longitudinal mode falls inside the mirror stop band while overlapping with the absorption and emission spectrum of the gain medium inside the cavity, see fig. 2.2(b). This implies a low energy cutoff for photons, below which no available cavity modes within the dye spectral bandwidth exist. In this way, an energetic ground state is realized and the previously described thermalisation mechanism could in principle continue indefinitely, i.e. it is not terminated when photons lose contact to the dye if they are red shifted out of the absorption bandwidth [78]. While the photons are restricted to only one longitudinal resonator mode, microcavities exhibit a spectrum of transverse eigenmodes, much like in macroscopic resonators. However due to the small cavity length, also these modes are separated by comparably large energy gaps, so that the total number of confined modes is much smaller than in large cavities. Photons are then effectively restricted to a transverse, two-dimensional (2D) plane with different transverse resonator modes [79].

2.3.1 | The Planar Microcavity

The most common microcavity of the Fabry-Perot type uses two plane mirrors to confine light along the cavity z-direction. Considering a single longitudinal mode with mode number q, the resonance condition is $\lambda_c = 2L_0/q\tilde{n}$ (λ_c is called the cutoff-wavelength) which implies for the longitudinal wave number $k_z = \pi q/L_0$. The cavity length L_0 is not necessarily equal to the physical distance between the two mirrors, considering that the optical field typically penetrates into a Bragg-reflector on a length scale of a few 100 nm (see the discussion in sec. 5.4.3). For incidence angles θ relative to the z-axis, the cavity is resonant for the wavelengths $\lambda = \lambda_c \cos\theta$ [80]. The energy is then, in terms of the transverse wave number k_r

$$E = \frac{\hbar c}{\tilde{n}}\sqrt{k_z^2 + k_r^2}\,. \tag{2.22}$$

For small angles in the paraxial approximation, $k_r \approx k_z\theta$, so that $k_r \ll k_z$. In this regime one finds

$$E \approx \frac{\hbar c}{\tilde{n}} k_z \left(1 + \frac{k_r^2}{2k_z^2}\right) = m_{\mathrm{ph}} \left(\frac{c}{\tilde{n}}\right)^2 + \frac{\hbar^2 k_r^2}{2m_{\mathrm{ph}}} \tag{2.23}$$

where the effective photon mass, $m_{\mathrm{ph}} = \tilde{n} q \pi \hbar / c L_0 \approx 7.8 \times 10^{-36}$ kg, was introduced, which is roughly five orders of magnitude lighter than the electron mass. In this way, it is evident that the dispersion relation is quadratic and continuous, which implies that photons in the transverse microcavity plane behave like massive particles in free space. Importantly, the low energy cavity cutoff provides a well defined ground state ($E \neq 0$) at the bottom of the dispersion relation ($k_r = 0$), which is essential, such that condensation into this ground state can occur.

2.3.2 | Arbitrary Cavity Geometry

The plane mirror cavity can also serve as a starting point for more elaborate cavity geometries, for which the dispersion relation is then extended by a potential energy term. Consider for example the situation sketched in fig. 2.3(a), where one of the cavity mirrors exhibits a non-uniform surface topography such that the longitudinal wave number k_z is a function of the local cavity length $L(r) = L_0 - \Delta L(r)$. Noting that $\Delta L(r) \ll L_0$, one can correspondingly write for the longitudinal wave number

$$k_z(r) = \frac{\pi q}{L_0 - \Delta L(r)} \approx \frac{\pi q}{L_0} + \frac{\pi q}{L_0}\frac{\Delta L(r)}{L_0} = k_z + \Delta k_z(r)\,. \tag{2.24}$$

Plugging this result into eq. (2.22) and keeping only terms to first order in $\Delta k_z(r)$, the result is

$$E \approx m_{\mathrm{ph}} \left(\frac{c}{\tilde{n}}\right)^2 \left[1 + \frac{\Delta L(r)}{L_0}\right] + \frac{\hbar^2 k_r^2}{2m_{\mathrm{ph}}} = m_{\mathrm{ph}} \left(\frac{c}{\tilde{n}}\right)^2 + \frac{\hbar^2 k_r^2}{2m_{\mathrm{ph}}} + V(r)\,, \tag{2.25}$$

where a trapping potential of the form $V(r) = m_{\mathrm{ph}} \left(\frac{c}{\tilde{n}}\right)^2 \frac{\Delta L(r)}{L_0}$ was defined. This result shows, that the mirror surface profile directly translates into the potential. This is the basis of engineering variable trapping potentials for photons inside the microcavity by tailoring the mirror geometry, a principle which will be made use of to create a periodic potential in this work.

2.3.3 | The Optical Schrödinger Equation

Upon closer inspection, the dispersion relation in eq. (2.25) can formally be obtained by solving the time-independent Schrödinger equation, which describes the transverse motion of a particle with mass m_{ph} in the potential $V(r)$ in two dimensions [81]. This result is also evident by considering the paraxial Helmholtz equation for monochromatic wave packets which can be cast into the form of a Schrödinger equation

$$i\hbar\frac{\partial}{\partial t}\Psi(r,t) = \left[-\frac{\hbar^2}{2m_{\mathrm{ph}}}\nabla_r^2 + V(r)\right]\Psi(r,t)\,, \tag{2.26}$$

where ∇_r^2 is the radial Laplace operator. Under the approximation of slowly varying and stationary field amplitudes $\psi(r)$, the solutions are of the form $\Psi(r,t) = \psi(r)e^{-i\omega t}$. The dispersion relation for

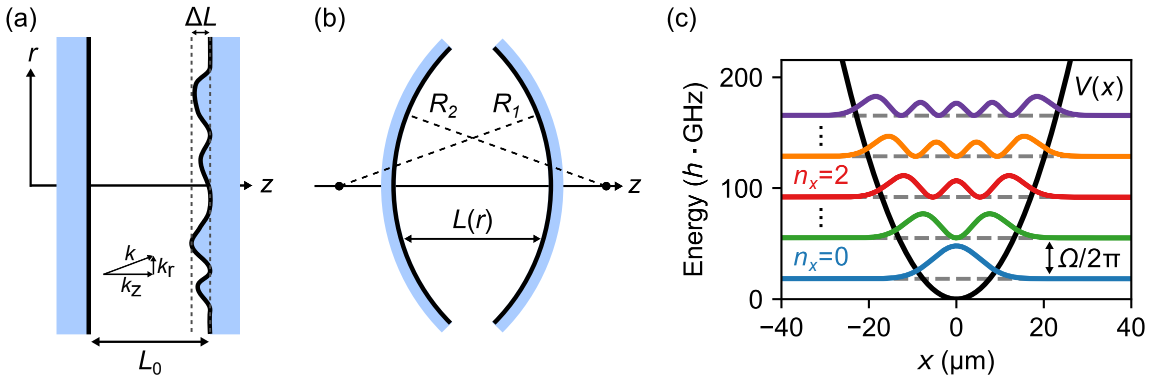

Figure 2.3: **(a)** Sketch of a microcavity of two mirrors separated by a distance L_0. The right mirror exhibits a surface profile which locally changes the cavity length by the amount $\Delta L(r)$. This modifies the boundary conditions for the longitudinal wave vector, k_z, of light confined between the mirrors and can be used to engineer the dispersion relation. **(b)** A microcavity built of two curved mirrors with radii of curvature R_1 and R_2. This configuration maps into a harmonic oscillator potential, which is illustrated in **(c)** for the situation in 1D. The potential is shown as the black line and the first five oscillator state densities ($|\psi_{n_x}(x)|^2$) are plotted by the coloured lines. They are vertically shifted by the corresponding resonance frequencies which are sketched by the dashed horizontal lines and they are each separated by the trapping frequency $\Omega/2\pi$ from neighbouring states along the energy axis. The used parameters to calculate the states are $q = 8$ and $R_1 = R_2 = 1$ m.

any cavity geometry can then be obtained by solving the eigenvalue equation

$$\hat{H}\psi(r) = E\psi(r) \quad \text{with} \quad \hat{H} = m_{\text{ph}}\left(\frac{c}{\tilde{n}}\right)^2 - \frac{\hbar^2}{2m_{\text{ph}}}\nabla_r^2 + V(r)\,, \tag{2.27}$$

where $\hat{H}$ denotes the Hamilton operator. The eigenvectors and eigenvalues then provide complete information about the cavity mode functions and the corresponding resonance frequencies. In contrast to the situation of freely moving photons in the transverse resonator plane ($V(r) = 0$), which can occupy a continuous spectrum of eigenstates, the resonance frequencies are now discretised for a finite size confining potential.

2.3.4 | Photons in a Harmonic Oscillator Potential

If the cavity is made of two spherically curved mirrors with radii of curvature R_1 and R_2 (fig. 2.3(b)), the local variation of the cavity length at position r close to the optical axis ($R_1, R_2 \gg r$), is given by $L(r) \approx L_0 - \frac{r^2}{2\tilde{R}}$, where $1/\tilde{R} = 1/R_1 + 1/R_2$ is the effective radius of curvature. In this case the mirror profile translates into $V(r) = \frac{1}{2}m_{\text{ph}}\Omega^2 r^2$, where $\Omega = c/\tilde{n}\sqrt{L_0\tilde{R}}$ denotes the angular trapping frequency of the resulting 2D harmonic oscillator potential. This is a particularly simple resonator geometry, as it allows to calculate the solutions of the Schrödinger equation analytically [82]. Owing to the radial symmetry of the problem, the wave functions in Cartesian coordinates are given by

$$\psi_{n_x,n_y}(x,y) = \psi_{n_x}(x)\cdot\psi_{n_y}(y) \quad \text{with} \quad n_x, n_y = 0, 1, 2, \ldots \tag{2.28}$$

$$\text{and} \qquad \psi_n(x) = \frac{1}{\sqrt{\sqrt{\pi}\,x_0\,2^n\,n!}}\exp\left(-\frac{1}{2}\frac{x^2}{x_0^2}\right)\cdot H_n\left(\frac{x}{x_0}\right)\,, \tag{2.29}$$

where n_x and n_y are the principal quantum numbers in x and y respectively. $x_0 = \sqrt{\hbar/m_{\mathrm{ph}}\Omega}$ is the harmonic oscillator length and H_n is the Hermite polynomial of order n. In analogy to the classical harmonic oscillator, where potential and kinetic energy are interchangeably converted from one to the other during half an oscillation period and the oscillation amplitude depends on the total energy of the particle as $r_{\mathrm{max}} = \sqrt{2E/m\Omega^2}$ (more energy means, that the particle can make it further up the potential hill), the transverse size of the quantum harmonic oscillator wave functions also increases with the square root of the photon energy. This is illustrated in fig. 2.3(c) which shows the five lowest energy solutions of the one-dimensional (1D) harmonic oscillator potential. The eigenenergies in 2D are given in terms of the quantum numbers n_x and n_y by

$$E_{n_x,n_y} = m_{\mathrm{ph}} \left(\frac{c}{\tilde{n}}\right)^2 + \hbar\Omega(n_x + n_y + 1) \tag{2.30}$$

and the degeneracy of a state with energy E is $g(E) = E/\hbar\Omega + 1$. This is a linear scaling with energy ($\alpha = 2$, see sec. 2.1.2) and thus it allows for Bose-Einstein condensation. An explicit calculation of the critical particle number at fixed temperature with the approximation that $\hbar\Omega \ll k_{\mathrm{B}}T$ yields

$$N_{\mathrm{c}} = 2\int_0^\infty \frac{E/\hbar\Omega + 1}{e^{E/k_{\mathrm{B}}T} - 1}\,\mathrm{d}E = \frac{\pi^2}{3}\left(\frac{k_{\mathrm{B}}T}{\hbar\Omega}\right)^2 \tag{2.31}$$

The factor of 2 accounts for the two orthogonal polarization states of light. Experiments on photon condensates are performed at room temperature, so $k_{\mathrm{B}}T \simeq h \cdot 6.3\,\mathrm{THz}$ and a typical trapping frequency for a cavity built of two mirrors with $R_1 = R_2 = 1\,\mathrm{m}$ is $\Omega \simeq 2\pi \cdot 41\,\mathrm{GHz}$, which gives a critical photon number of $N_{\mathrm{c}} \simeq 77\,000$ [10]. Experimentally the transition point from thermal to the condensed phase is reached by increasing the photon number in the cavity.

2.3.5 | Bose-Einstein Condensation in Potentials of Finite Size and Depth

The estimation for the critical photon number given in the previous section is only valid for trap depths that extend up to energies much larger than thermal energy. Especially in experiments working with tailored microtraps for light, the achievable trap depths are often smaller than $k_{\mathrm{B}}T$ [34, 37, 83, 84]. In this case an estimation for the critical photon number can be obtained by computing the finite sum over all confined states, which can amount to photon numbers in the single digit domain upon reaching criticality [83], but the transition from the non-degenerate to the condensed regime in such small systems is softened considerably. These experiments are far from the thermodynamic limit ($N \longrightarrow \infty$, $V \longrightarrow \infty$) and it is up for debate, if the resulting accumulation of photons in the ground state should be referred to as a second order phase transition to a Bose-Einstein condensate. In the limit of very large occupations however, i.e. when the chemical potential is very close to the ground state energy, the population in the excited states saturates for any finite size and depth potential, regardless of the potential geometry. This was recently confirmed by the experimental demonstration of a BEC-like phase transition for photons in a finite size two-dimensional box potential, where condensation could not be observed in an infinite size box [84] and it holds true even in the limit of just two confined energy levels, i.e. only a single excited state can show saturation [85]. After all, as mentioned in sec. 2.1.2, the density of states governs if the macroscopic ground state occupation would hold in the thermodynamic limit. The phase transition behaviour of photon gases in tailored microtraps with harmonic oscillator density of states was recently studied for the dimensional crossover from 2D to 1D and evidence was found for a phase transition in 2D while the 1D case exhibits a crossover [86, 87].

2.4 | Non-Equilibrium Model of Photon Condensation

The previously described system of a photon gas confined to a cavity with perfectly reflecting walls is only an idealized picture. A real cavity always exhibits finite losses as there is a small probability for photons to not being reflected from the mirrors but being e.g. transmitted instead. Moreover, an optical cavity is not a closed container, so photons can be radiated into free space after being absorbed by a molecule or photons are lost due to the finite quantum yield of the dye. In order to maintain a constant excitation level in the cavity, the dye solution is continuously pumped. Photon condensates are therefore intrinsically driven-dissipative systems in which a steady state is established [39]. A general model for photon condensation should therefore capture all the relevant processes of pumping, absorption and emission of photons from and into the manifold of resonator modes as well as cavity losses and photon emission into free space. Such a model can be derived on the grounds of the Jaynes-Cummings Hamiltonian [88, 89]. However, the description can be simplified tremendously when only the average populations are of interest, as this allows to neglect cross correlations between different modes. The interaction between photons and molecules is assumed to be in the weak coupling regime, which is well justified, given the dephasing of excited electronic states due to the rapid internal thermalisation. The resulting rate equations were first introduced in [12] and have been further developed to also account for spatial inhomogeneities in the cavity [90]. They were employed to successfully model the temporal evolution, the fluctuation dynamics and the response of the condensate to external perturbations as well as for the analysis of the spatial photon distribution [40, 90–95]. The rate equations will be introduced in the next sections, to provide a basis for the interpretation of the findings in this work.

2.4.1 | Rate Equations - Spatially Homogeneous Cavity

The most commonly used form of the rate equations as usually given in textbooks [96, 97] can be expressed for a cavity with homogeneous mode and molecular excitation profiles. The number of photons n_m in mode m and the number of excited dye molecules $M_\uparrow$ obey a set of first-order nonlinear differential equations [89]

$$\frac{\partial n_m}{\partial t} = -\kappa_m n_m + \Gamma_{21,m}(n_m + 1)M_\uparrow - \Gamma_{12,m} n_m (M - M_\uparrow) \tag{2.32}$$

$$\frac{\partial M_\uparrow}{\partial t} = -\Gamma_\downarrow M_\uparrow + \Gamma_\uparrow (M - M_\uparrow)\,. \tag{2.33}$$

Here M is the total molecule number in the cavity, κ_m is the cavity loss rate for mode m and $\Gamma_{12,m}$ ($\Gamma_{21,m}$) is the rate of absorption (emission) per molecule for mode m. In particular, also spontaneous emission into the cavity modes is included in this model (by the term $\Gamma_{21,m}M_\uparrow$), an aspect which is crucial to properly describe the system in the regime of small photon numbers $n_m < 1$. The molecular decay rate $\Gamma_\downarrow$ is given by

$$\Gamma_\downarrow = \Gamma_{\mathrm{sp}} + \sum_m \Gamma_{21,m}(n_m + 1)\,, \tag{2.34}$$

which summarizes the losses by spontaneous emission into free space as well as due to a finite quantum yield in Γ_{sp}. The total excitation rate for the molecules $\Gamma_\uparrow$ is given by

$$\Gamma_\uparrow = \Gamma_{\mathrm{p}} + \sum_m \Gamma_{12,m} n_m\,, \tag{2.35}$$

which includes reabsorption of cavity photons and pumping at a rate Γ_p.

2.4.2 | Rate Equations - Spatially Inhomogeneous Cavity

While the above presented model includes most of the essential aspects for calculating the photon population in a multimode cavity, it does not allow to account for spatial inhomogeneities of the molecular excitation profile or of different resonator modes. Experiments have shown however, that especially the focus size and position of the pump beam can be essential to understand the resulting photon distributions [17, 85], and it is also of relevance for this work.

A more refined model replaces the number of molecules by a constant molecule density $\rho(\mathbf{x}) \equiv \rho_\mathbf{x}$ and the excited state molecule number is replaced by an excitation density $\rho_\uparrow(\mathbf{x})$, which is a function of the position $\mathbf{x} = (x, y)^\mathrm{T}$ in the cavity. The resonator mode profiles $|\psi_m(\mathbf{x})|^2$ are taken into account for the calculation of absorption and emission rates to ensure that photons can only be absorbed or emitted from molecules at position $\mathbf{x}'$ from or into mode m if at this point $|\psi_m(\mathbf{x}')|^2 \neq 0$, see fig. 2.4(a) for an illustration. The transversal coordinates are here of interest only, because the system is restricted to a single longitudinal mode and variations of the field distribution along the cavity axis are neglected. The rate equation for the photon number then correspondingly changes to

$$\frac{\partial n_m}{\partial t} = -\kappa_m n_m + \int \left[\Gamma_m^-(n_m+1)|\psi_m(\mathbf{x})|^2 \rho_\uparrow(\mathbf{x}) - \Gamma_m^+ n_m |\psi_m(\mathbf{x})|^2 \left(\rho_\mathbf{x} - \rho_\uparrow(\mathbf{x})\right)\right] \mathrm{d}\mathbf{x}\,. \tag{2.36}$$

Here $\rho_\mathbf{x}$, $\rho_\uparrow(\mathbf{x})$ and $|\psi_m(\mathbf{x})|^2$ are densities in units of $1/\mathrm{m}^2$ and $\Gamma_m^\pm$ are the absorption and emission rates per molecule per unit area with units of m^2/s. Defining the spatial excitation profile by $f(\mathbf{x}) := \rho_\uparrow(\mathbf{x})/\rho_\mathbf{x}$, one can write

$$\rho_\uparrow(\mathbf{x}) = \rho_\mathbf{x} f(\mathbf{x})\,, \quad \rho_\mathbf{x} - \rho_\uparrow(\mathbf{x}) = \rho_\mathbf{x}(1 - f(\mathbf{x}))\,. \tag{2.37}$$

This allows to simplify the notation, so that

$$\frac{\partial n_m}{\partial t} = -\kappa_m n_m + \Gamma_m^- \rho_\mathbf{x}(n_m+1) f_m - \Gamma_m^+ \rho_\mathbf{x} n_m (1 - f_m) \tag{2.38}$$

$$\text{with} \quad f_m = \int |\psi_m(\mathbf{x})|^2 f(\mathbf{x})\,\mathrm{d}\mathbf{x}\,. \tag{2.39}$$

Here f_m is a measure for the overlap of the excitation profile with mode m and $\Gamma_m^+\rho_\mathbf{x} := \Gamma_{12,m}$ ($\Gamma_m^-\rho_\mathbf{x} := \Gamma_{21,m}$) is the total absorption (emission) rate for mode m. Using the total rates for up and down-transitions in the molecules

$$\Gamma_\uparrow = \left[\Gamma_\mathrm{p}(\mathbf{x}) + \sum_m \Gamma_m^+ n_m |\psi_m(\mathbf{x})|^2\right] \quad \text{and} \quad \Gamma_\downarrow = \left[\Gamma_\mathrm{sp} + \sum_m \Gamma_m^-(n_m+1)|\psi_m(\mathbf{x})|^2\right], \tag{2.40}$$

with the position dependent pump rate $\Gamma_\mathrm{p}(\mathbf{x})$ which is determined by the pump beam profile, one can correspondingly write for the rate concerning the spatial excitation profile

$$\frac{\partial f(\mathbf{x})}{\partial t} = -\Gamma_\downarrow f(\mathbf{x}) + \Gamma_\uparrow\left(1 - f(\mathbf{x})\right)\,. \tag{2.41}$$

In this model, photons are delocalized within the cavity modes, i.e. they are not defined as functions of $\mathbf{x}$ directly. The probability distribution of a photon in mode m is given by $|\psi_m(\mathbf{x})|^2$. In general this set of nonlinear equations needs to be solved numerically. However with a few simplifying approximations,

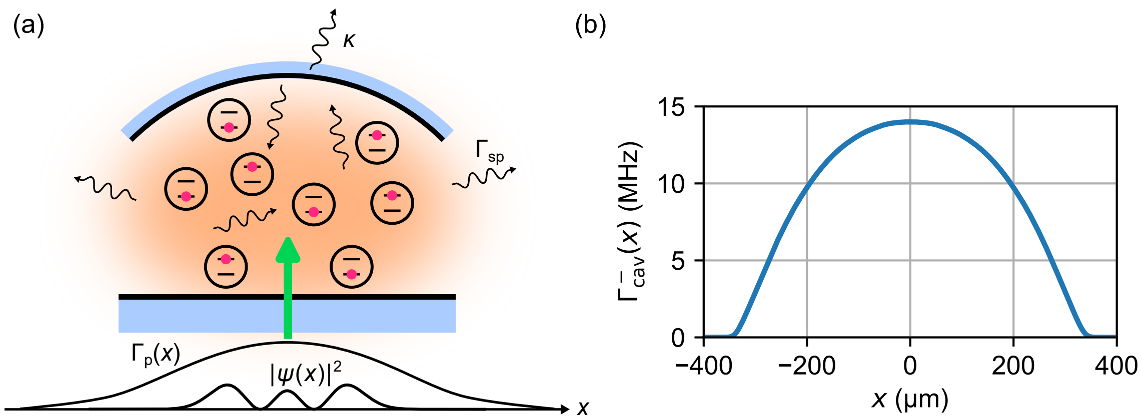

Figure 2.4: **(a)** Schematic of the dye-filled microcavity. An external pump beam excites molecules in the cavity at rate $\Gamma_\mathrm{p}(\mathbf{x})$. Molecular excitations can then be converted into cavity photons by emission (spontaneous or stimulated) into a cavity mode with the density profile $|\psi(\mathbf{x})|^2$, if there is a finite overlap between the molecule and the cavity mode. Photons can also be radiated out of the cavity at rate Γ_sp. Photons populating the cavity can either be reabsorbed by ground state molecules or they leave the cavity at rate κ. **(b)** Numerically calculated total spontaneous emission rate per molecule into the cavity as a function of x for $y = 0$, for typical experimental parameters of $q = 8$, $\lambda_c = 580\,\mathrm{nm}$ and two mirrors with $R = 1$ m, yielding a harmonic oscillator potential with trapping frequency $\Omega = 2\pi \cdot 36.9\,\mathrm{GHz}$. The calculation takes the first 1000 oscillator levels into account.

a semi-analytical expression can be obtained for the limiting case of small photon numbers. In order to motivate these approximations, it is important to understand the competing rates in the model, which will be discussed in the next sections.

2.4.3 | Absorption and Emission Rates

In order to calculate the absorption rate of a photon in mode m, consider Lambert-Beer's law, which states that a stream of n photons propagating through an absorbing medium with number density $\rho = N_\mathrm{A} \cdot C$ (N_A: Avogadro constant, C: molar concentration) and absorption cross section σ_a is attenuated along the propagation direction z according to

$$\frac{\partial n}{\partial z} = -n\rho\sigma_\mathrm{a}\,. \tag{2.42}$$

Changing coordinates from space to time by $\partial z/\partial t = c/\tilde{n}$, with the refractive index $\tilde{n}$ of the medium, allows to formulate this expression in terms of an absorption rate Γ_{12}, i.e.

$$\frac{\partial n}{\partial t} = -n\frac{\rho\sigma_\mathrm{a}c}{\tilde{n}} = -n\Gamma_{12}\,. \tag{2.43}$$

When the absorbing medium is confined to a volume V, so that the number density in this volume is $\rho = M/V$, the absorption rate per absorber is

$$\frac{\Gamma_{12}}{M} = \frac{\sigma_\mathrm{a}c}{\tilde{n}V}\,. \tag{2.44}$$

If the photons and the absorbers are inside a cavity mode, the volume would be given by the mode volume, which is commonly defined, for a homogeneously filled cavity, in terms of the mode profile by

$$V_m = \frac{\int |\psi_m(\mathbf{x})|^2 \,\mathrm{d}V}{\max\left[|\psi_m(\mathbf{x})|^2\right]} = \frac{L_0 \cdot \int |\psi_m(\mathbf{x})|^2 \,\mathrm{d}\mathbf{x}}{\max\left[|\psi_m(\mathbf{x})|^2\right]} = \frac{L_0}{\max\left[|\psi_m(\mathbf{x})|^2\right]}, \tag{2.45}$$

with the cavity length L_0 and mode index m [98]. Here it was used that $\int |\psi_m(\mathbf{x})|^2 \,\mathrm{d}\mathbf{x} = 1$, since the mode functions are normalized. If one is interested in the absorption rate in mode m at position $\mathbf{x}$, one can analogously write for the local absorption rate per molecule

$$\Gamma_{12,m}(\mathbf{x}) = \frac{\sigma_{\mathrm{a},m} c}{\tilde{n} V_m(\mathbf{x})} = \frac{\sigma_{\mathrm{a},m} c}{\tilde{n} L_0} |\psi_m(\mathbf{x})|^2 =: \Gamma_m^+ |\psi_m(\mathbf{x})|^2 . \tag{2.46}$$

This result provides a simple expression for the absorption rate per molecule at position $\mathbf{x}$ in terms of the mode profile, absorption cross section and cavity length. The density $\rho_\mathbf{x}$ is related to the volume density by $\rho_\mathbf{x} = L_0 \cdot \rho$, i.e. all molecules along the cavity length are effectively concentrated in the two-dimensional transverse resonator plane. The result of eq. (2.46) can be inserted into eq. (2.38) for a validity check of the derived absorption rate. In the case of $\kappa_m = 0$ and $f_m = 0$, i.e. zero cavity losses and zero molecular excitations, one finds that $\partial n_m / \partial t = -n_m \Gamma_m^+ \rho_\mathbf{x} = -n_m \Gamma_{12,m}$, which was the starting point of the derivation.

Regarding the emission rate for mode m, it can be expressed in an equivalent manner to the absorption rate, when the absorption cross section is replaced by the emission cross section $\sigma_{\mathrm{e},m}$, i.e.

$$\Gamma_{21,m}(\mathbf{x}) = \frac{\sigma_{\mathrm{e},m} c}{\tilde{n} V_m(\mathbf{x})} = \frac{\sigma_{\mathrm{e},m} c}{\tilde{n} L_0} |\psi_m(\mathbf{x})|^2 =: \Gamma_m^- |\psi_m(\mathbf{x})|^2 . \tag{2.47}$$

The measured fluorescence spectrum $L(\lambda)$ (also called line shape function) and the excited state lifetime τ are related to the emission cross section by the relation [99–101]

$$L(\lambda_m) = \frac{8\pi\tau\tilde{n}^3}{\lambda_m^4} \frac{\sigma_{\mathrm{e},m} c}{\tilde{n}} \quad \text{with} \quad \int L(\lambda)\,\mathrm{d}\lambda = \Phi , \tag{2.48}$$

which can be derived from Fermi's golden rule (see appx. A.2), for an emitter with a bandwidth much larger than the cavity linewidth, as is the case for the dye-filled microcavities. Normalization of the line shape function requires that the integral over the emission bandwidth is equal to the quantum yield Φ. The emission cross section can hence be calculated, if the quantum yield is known. The spontaneous emission rate of a single emitter into the cavity mode scales with V_m^{-1}, so the mode volume should be relatively small in order to efficiently channel spontaneously emitted photons into the mode. The cavity resonance enhancement known from the Purcell effect [102], proportional to the cavity quality factor Q, is however absent, which is due to the large emission bandwidth of the dye.

An alternative and direct way to calculate the emission rate, is by use of the previously derived Kennard-Stepanov relation. If this relation is fulfilled and the quantum yield is equal to unity, the emission rates obtained by the two methods of course have to coincide. For a quantum yield $\Phi \lesssim 1$, the Kennard-Stepanov relation has to be modified accordingly, so that

$$\frac{\Gamma_{21,m}}{\Gamma_{12,m}} = \Phi \cdot \exp\left(-\frac{\hbar\delta_m}{k_\mathrm{B} T}\right), \quad \text{with} \quad \delta_m = \omega_m - \omega_\mathrm{zpl} . \tag{2.49}$$

Apart from a finite quantum yield, real emission spectra also show other deviations from this relation, which can be seen from fig. 2.1(a), where the emission cross section is calculated from (2.49) (dashed) and from the relation given in (2.48) (solid). As is evident the two curves are not identical, however the good agreement for wavelengths larger than 550 nm shows that it is well justified to make use of the Kennard-Stepanov relation.

2.4.4 | Coupling Efficiency of Spontaneous Emission

As discussed in the previous section, the emission rate (and also the absorption rate) of a molecule into a cavity mode inversely depends on the mode volume (see eq. (2.47)), which is a consequence of the modified density of states inside the cavity [103]. The emission rate out of the cavity will be modified as well, because the emitter can only interact with a subset of the free-space modes, which is in a geometrical picture determined by the solid angle over which the background of free-space modes is accessible. However, as most wavelength-sized optical cavities cover only a rather small fraction of the free-space solid angle of 4π, it is usually a good approximation to set $\Gamma_{\text{sp}} = \tau^{-1} = 250\,\text{MHz}$ [104, 105]. The total spontaneous lifetime was used here explicitly, so that the spontaneous decay rate also includes nonradiative transitions.

For small photon numbers, i.e. when stimulated emission can be neglected, the rate for downward transitions given in eq. (2.40) reads

$$\Gamma_{\downarrow}(\mathbf{x}) = \Gamma_{\text{sp}} + \sum_m \Gamma_m^- |\psi_m(\mathbf{x})|^2 =: \Gamma_{\text{sp}} + \Gamma_{\text{cav}}^-(\mathbf{x}) \,. \tag{2.50}$$

Using this equation, one can define a spontaneous emission factor β_{sp}, as the ratio of the emission rate into the cavity by the total emission rate, similar to the standard definition used for microlasers [106, 107]. Taking into account the dependence on the position $\mathbf{x}$ in the cavity, gives

$$\beta_{\text{sp}}(\mathbf{x}) = \frac{\Gamma_{\text{cav}}^-(\mathbf{x})}{\Gamma_{\downarrow}(\mathbf{x})} \approx \frac{\Gamma_{\text{cav}}^-(\mathbf{x})}{\Gamma_{\text{sp}}} \,, \tag{2.51}$$

where the approximation made in the second step is valid for $\Gamma_{\text{sp}} \gg \Gamma_{\text{cav}}^-(\mathbf{x})$. With the help of eq. (2.47), a numerical calculation for the first 1000 modes in a two-dimensional harmonic oscillator potential (covering $\sim 37\,\text{THz}$ of spectral bandwidth) with the cutoff wavelength of $\lambda_c = 580\,\text{nm}$ and longitudinal mode number $q = 8$, reveals that the maximum of $\beta_{\text{sp}}(\mathbf{x})$ is found at $\mathbf{x} = 0$, see fig. 2.4(b). The total emission rate into the cavity at this point is $\Gamma_{\text{cav}}^-(0) \approx 14\,\text{MHz}$, which amounts to a total fraction of spontaneously emitted photons into the cavity of $\beta_{\text{sp}}(0) \approx 6\%$. This result agrees with what has been reported by other authors [90, 108, 109]. Intuitively it is expected that $\beta_{\text{sp}}(\mathbf{x})$ is largest in the cavity centre, because the total cavity mode density is at a maximum at this point. For excited molecules located further away from the cavity centre, the spontaneous emission factor continuously decreases. The approximation of $\Gamma_{\downarrow}(\mathbf{x}) \approx \Gamma_{\text{sp}}$ is decently accurate if stimulated emission is not dominant. It will be used later to derive an expression for the photon distribution in the limit of small photon numbers and for the condensation pump threshold.

2.4.5 | Cavity Loss Rate

The cavity loss rate κ_m measures the number of photons lost from the cavity per unit time. Neglecting all other contributions than mirror transmission, the loss rate for a cavity with length L_0 and two equal mirrors with power reflectivity $R_m = 1 - T_m$ (transmission T_m) for $T_m \ll 1$ can be approximated by [110]

$$\kappa_m = \frac{c}{\tilde{n}L_0}(1 - R_m) = \frac{c}{\tilde{n}L_0}T_m \,. \tag{2.52}$$

In a real cavity, the equality of $R_m + T_m = 1$ is only approximately fulfilled, which is due to scattering losses or absorption of light in the mirrors. Assuming that these effects are small however, eq. (2.52) usually gives a good estimate of the actual cavity loss rate. With $L_0 \approx 1.5\,\mu\mathrm{m}$, $\tilde{n} = 1.44$ and $T_m \approx 20\,\mathrm{ppm}$, typical values are $\kappa_m \approx 3\,\mathrm{GHz}$.

2.4.6 | Steady State and Equilibrium Solutions of the Rate Equations

For experiments which are performed under constant pumping, the photon number and molecular excitation density in the cavity assume a steady state. The coupled set of rate equations can be solved for this case by setting all derivatives to zero, which gives the steady state solutions in terms of the (mode dependent) absorption and emission rates $\Gamma_{12,m}$ and $\Gamma_{21,m}$, the cavity loss rates κ_m and the modal overlap integrals f_m with the molecular excitation profile $f(\mathbf{x})$

$$n_m = \frac{1}{\frac{\Gamma_{12,m}}{\Gamma_{21,m}}\frac{1-f_m}{f_m} - 1 + \frac{\kappa_m}{\Gamma_{21,m}f_m}} \quad \text{and} \quad f(\mathbf{x}) = \frac{1}{\frac{\Gamma_{\downarrow}(\mathbf{x})}{\Gamma_{\uparrow}(\mathbf{x})} + 1} \,. \tag{2.53}$$

Upon use of the Kennard-Stepanov relation and comparison with the Bose-Einstein distribution, an expression for the chemical potential can be derived

$$\mu_m = \hbar\omega_{\mathrm{zpl}} - \hbar\omega_{\mathrm{c}} - k_{\mathrm{B}}T \ln\left(\frac{1-f_m}{f_m} + \frac{\kappa_m}{\Gamma_{12,m}f_m}\right) , \tag{2.54}$$

which generally is a function of energy and thus the mode number m. This result is similar to the one derived in eq. (2.18), however with a finite ground state energy $\hbar\omega_{\mathrm{c}}$ and including a correction due to loss from the cavity. Assuming $\kappa_m \ll \Gamma_{12,m}$, i.e. photons in the cavity are absorbed much faster than they are lost by mirror transmission, and a homogeneous excitation profile so that f_m is mode-independent, the chemical potential becomes uniform

$$\mu = \hbar\omega_{\mathrm{zpl}} - \hbar\omega_{\mathrm{c}} + k_{\mathrm{B}}T \ln\left(\frac{\rho_{\uparrow}}{\rho_{\downarrow}}\right) , \tag{2.55}$$

where $\rho_{\uparrow}$ and $\rho_{\downarrow}$ are the total densities of excited and ground state molecules. The chemical potential is controlled by the relative excitation level in the dye molecules, as was also concluded in section 2.2.4. When BEC is approached, the chemical potential assumes the threshold value $\mu \longrightarrow 0$, so that the equilibrium critical excitation fraction is given by

$$f_{\mathrm{th}}(\mathbf{x}) \equiv f_{\mathrm{th}} = \frac{1}{1 + e^{\hbar(\omega_{\mathrm{zpl}} - \omega_{\mathrm{c}})/k_{\mathrm{B}}T}} \,. \tag{2.56}$$

2.4.7 | Small Photon Numbers

In the case that the photon number in the cavity is small ($n_m \lesssim 1$), so that the background decay rate greatly outweighs the emission rate into the cavity, it is justified to approximate $\Gamma_{\downarrow}(\mathbf{x}) \approx \Gamma_{\mathrm{sp}}$. The excitation level is very small in this regime and the great majority of excited molecules are induced by the pump beam, so that

$$f(\mathbf{x}) \approx \frac{\Gamma_\mathrm{p}(\mathbf{x})}{\Gamma_\mathrm{sp}} \,. \tag{2.57}$$

A homogeneous excitation profile correspondingly requires a homogeneous pump profile, i.e. a pump beam which is much bigger than the system size, so that $\Gamma_\mathrm{p}(\mathbf{x}) \equiv \Gamma_\mathrm{p}$. From eq. (2.57), one finds that $f_m = \int f(\mathbf{x})|\psi_m(\mathbf{x})|^2 \,\mathrm{d}\mathbf{x} \approx \Gamma_\mathrm{sp}^{-1} \int \Gamma_\mathrm{p}(\mathbf{x})|\psi_m(\mathbf{x})|^2 \,\mathrm{d}\mathbf{x} \ll 1$, so that a simplified expression for the small photon number distribution can be derived, which is [90]

$$n_m \approx \frac{\Gamma_{21,m}}{\Gamma_{12,m} + \kappa_m} \cdot f_m = \frac{1}{\Gamma_\mathrm{sp}} \frac{\Gamma_{21,m}}{\Gamma_{12,m} + \kappa_m} \cdot \int \Gamma_\mathrm{p}(\mathbf{x})|\psi_m(\mathbf{x})|^2 \,\mathrm{d}\mathbf{x} \,. \tag{2.58}$$

The spectral distribution of photons in the cavity is therefore determined by the pump beam overlap with the individual modes and a mode-dependent prefactor, which are both, to some extent, tunable parameters in the microcavity. Eq. (2.58) is useful to semi-analytically calculate the photon distribution far below the condensation threshold. Under equilibrium conditions, i.e. $\kappa_m \ll \Gamma_{12,m}$ and $\Gamma_\mathrm{p}(\mathbf{x}) \equiv \Gamma_\mathrm{p}$, the small photon number solution can be further simplified, which yields

$$n_m = \frac{\Gamma_\mathrm{p}}{\Gamma_\mathrm{sp}} \frac{\Gamma_{21,m}}{\Gamma_{12,m}} \simeq n_\mathrm{p} \cdot e^{-\hbar\omega_m/k_\mathrm{B}T} \,. \tag{2.59}$$

In this limit, the photon distribution can thus be well described by a Boltzmann distribution, where the scale factor n_p is experimentally set by the pump power.

2.4.8 | Realizing a Uniform Chemical Potential in an Open Cavity

While the previous section 2.4.6 explicitly treated the limiting case of small cavity losses compared to photon reabsorption, an interesting question to ask is, if a uniform chemical potential can also be realized when this condition does not apply. The answer of this question comes down to finding the required molecular excitation profile, such that the resulting chemical potential is uniform and the photon distribution is a Bose-Einstein distribution, even in the presence of finite cavity losses. Starting from the general expression for the mode dependent chemical potential in eq. (2.54), a condition for the modal overlap integral f_m with $\mu_m \equiv \mu$ can be derived

$$f_m = \frac{1 + \frac{\kappa_m}{\Gamma_{12,m}}}{1 + e^{[\hbar(\omega_\mathrm{zpl} - \omega_\mathrm{c}) - \mu]/k_\mathrm{B}T}} \,. \tag{2.60}$$

If the molecular excitation profile matches condition (2.60), the resulting photon distribution will be the same as an equilibrium Bose-Einstein distribution, despite non-zero cavity losses. It is easily verified that the equilibrium excitation fraction at threshold, as given in eq. (2.56), is correctly recovered for $\kappa_m/\Gamma_{12,m} \rightarrow 0$ and $\mu \rightarrow 0$.

The molecular excitation profile, and therefore f_m, is predominantly determined by the profile of the used pump beam. Recalling that the experimental cavity mirror stop band is centred around 530-550 nm (cf. fig. 2.2(a)) and the cutoff wavelength is typically fixed around $\lambda_\mathrm{c} = 580\,\mathrm{nm}$, κ_m is a decreasing function with increasing mode number m, while the absorption rate increases (exponentially) with increasing mode number. This means that $\kappa_m/\Gamma_{12,m}$ is a decreasing function of the mode number. This result is very important, because it is then possible that the condition in (2.60), for parameters where $\kappa_m/\Gamma_{12,m} \neq 0$, can be approximately fulfilled by using a focused pump beam. The pump shape

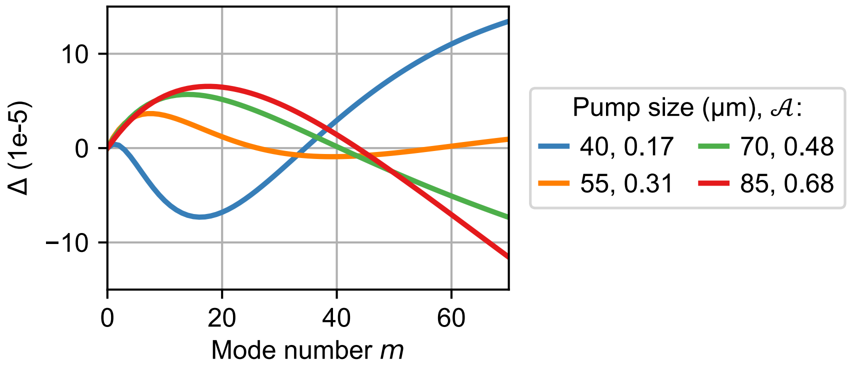

Figure 2.5: Δ, defined as the LHS - RHS of eq. 2.62, as a function of the mode number m in a one-dimensional harmonic oscillator potential with 70 oscillator levels. The numerical parameters are $\lambda_c = 584\,\text{nm}$, longitudinal mode number $q = 9$, trapping frequency $\Omega = 2\pi \cdot 63\,\text{GHz}$, dye concentration $\rho = 1\,\text{mmol/l}$ and the rates for cavity loss and photon absorption/emission at the ground state wavelength are $\kappa = 4.1\,\text{GHz}$, $\Gamma_{12} = 4.2\,\text{GHz}$, and $\Gamma_{21} = 1\,434.5\,\text{GHz}$, i.e. cavity losses occur on a comparable timescale as photon absorption. For an intermediate pump size of 55 µm FWHM, Δ exhibits the least variations around 0, corresponding to a relatively uniform chemical potential. The photon number at threshold would be smaller by a factor $\mathcal{A} = 0.31$, compared to the ideal case, when condition (2.60) could be exactly matched. Larger critical photon numbers in the cavity would be obtained for larger pump sizes, however at the cost of greater deviations from a uniform chemical potential.

typically follows a Gaussian intensity profile with an adjustable beam size. Even though this provides great tunability in principle, it is not certain that the condition in (2.60) can be exactly met for every given trapping potential or cutoff wavelength. In an experiment, the pump profile could be adjusted so that the photon distribution at the onset of condensation is well described by a threshold Bose-Einstein distribution. However, the experimental critical photon number can potentially be smaller than the theoretical critical number. This aspect can be taken into account by introducing a scale factor $\mathcal{A}$ for the Bose-Einstein distribution, i.e.

$$n_m = \frac{1}{\frac{\Gamma_{12,m}}{\Gamma_{21,m}}\frac{1-f_m}{f_m} - 1 + \frac{\kappa_m}{\Gamma_{21,m} f_m}} = \frac{\mathcal{A}}{e^{[\hbar(\omega_m-\omega_c)-\mu]/k_B T} - 1}\,. \tag{2.61}$$

The corresponding condition for the overlap integral f_m at the threshold to BEC with $\mu \to 0$ is then given by

$$f_m = \frac{1 + \frac{\kappa_m}{\Gamma_{12,m}}}{1 + \frac{1}{\mathcal{A}} e^{\hbar(\omega_{\text{zpl}}-\omega_c)/k_B T} + (1 - \frac{1}{\mathcal{A}}) e^{\hbar(\omega_{\text{zpl}}-\omega_m)/k_B T}}\,. \tag{2.62}$$

The difference between the LHS and the RHS of eq. (2.62) (defined as Δ) is numerically evaluated for the example of a one-dimensional harmonic oscillator potential. The numerical parameters, which are the same as experimental parameters used in chapter 6 of this thesis, are given in the caption of fig. 2.5, which shows Δ as a function of the mode number m for different sizes of a Gaussian pump profile. The scale factor $\mathcal{A}$ is determined by the smallest overall deviation of Δ from 0, when Δ is calculated for $0 < \mathcal{A} <= 1$, i.e. it is the scale factor $\mathcal{A}$ for which eq. 2.62 is best fulfilled. The excitation profile at threshold is approximated by $f_{\text{th}}(\mathbf{x}) \approx \Gamma_{\text{p,th}}(\mathbf{x})/\Gamma_{\text{sp}}$ according to the discussion in chapter 4, where a detailed analysis of the pump threshold will be presented. By default, Δ is always zero for the ground mode, when this approximation for the threshold excitation level is used. With increasing mode number however, Δ deviates from zero, meaning that the chemical potential would not be perfectly uniform.

The smallest overall deviation is found for a pump size around 55 µm full width at half maximum (FWHM) with $\mathcal{A} = 0.31$, which should correspondingly give the closest agreement between the photon distribution and a threshold Bose-Einstein distribution. However, the critical photon number in the cavity would be only 31% of the theoretical number, which would be obtained if condition (2.60) could be exactly matched.

To conclude the section, it was found that for very small cavity losses and strong absorption by the dye molecules, combined with a homogeneous pump profile, a thermalized photon distribution inside the cavity can be achieved. A macroscopic occupation of the ground mode for high photon numbers on top of a broad cloud of photons in higher energy modes can then be classified as photon BEC [88]. However, the dye-filled cavity is still far from being a closed system, as continuous pumping is required in order to replenish the excitations which are lost by spontaneous emission into free space. Interestingly, thermalisation of photons is possible nevertheless, but it is predominantly achieved by one emission (following excitation from the pump) and one absorption event, rather than by repeated cycles of absorption and reemission of photons into the cavity modes. Such cycles become unlikely, at least in the absence of stimulated emission [19]. The equation for the molecular excitation level does not need to be considered explicitly in order to derive the equilibrium photon distribution (with $\kappa_m = 0$ and $f_m = const$), which is perhaps why the loss channel of spontaneous emission into free space is rarely mentioned. An imperfect redistribution of photons in the cavity towards thermal equilibrium is also the reason, why the small photon number distribution is directly proportional to the modal overlap with the pump profile. While this aspect might seem problematic at first, an adjustable chemical potential by tuning the pump shape can also be regarded as a very useful feature, since it in principle also allows to realize approximately Bose-Einstein distributed photons, when κ_m can not be neglected compared to $\Gamma_{12,m}$.

2.5 | Creation of Potentials for Photon Gases

The ability of imprinting tailored potential energy landscapes for two-dimensional photon gases has recently opened up the way for the investigation of photon condensation in non-trivial potentials with possible application in simulations of a wide range of Hamiltonians. For the experimental implementation, several different approaches were tested. Early experiments successfully worked with admixing a thermoresponsive polymer (poly(N-isopropylacrylamide)) to the Rhodamine 6G solution [34], which allowed for the direct control of a reversible attractive potential. An entirely different approach uses focused Gallium ion beam milling, to carve out the desired surface profile on the mirror substrate before the distributed Bragg reflector (DBR) coating is applied [111, 112]. This technique is especially well suited to create notches with extremely small radii of curvature on the few µm scale, which can provide tiny mode volumes [83]. A drawback of this method is that it involves a laborious procedure where the potential geometry has to be precisely laid out in the beginning. The structuring method used in this thesis allows to routinely create permanent surface structures by direct laser writing [85]. It was developed and thoroughly investigated in previous works and it is now a well established technique [37, 85, 113], which is also used in conjunction with the thermoresponsive polymer in order to allow for further tailoring of the potential during experiments [38, 114]. The following section briefly summarizes the main aspects and the physical origin of the microstructuring technique. An in depth analysis can be found in [36].

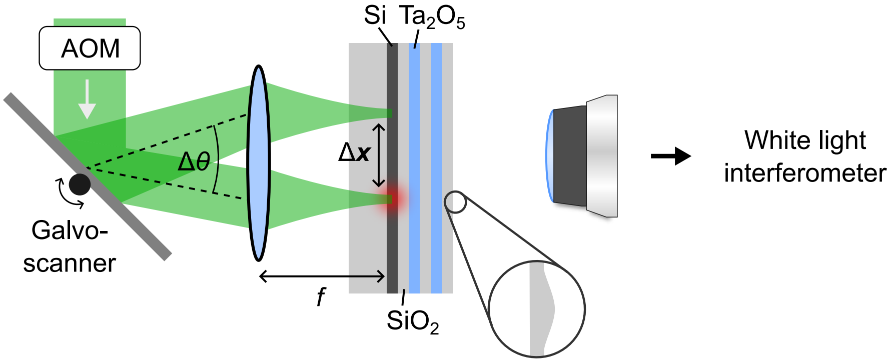

Figure 2.6: Schematic sketch of the microstructuring setup. A laser beam is focused onto the silicon layer from the mirror backside through the substrate. Absorption of the laser light in the silicon locally heats up the dielectric layers on top and leads to a permanent lifting of the surface on a nm scale. The laser beam power is controlled in time by an acousto-optical modulator (AOM) and a galvo-scanner laterally deflects the beam. The focusing lens then converts this angular deflection $\Delta\theta$ into a lateral shift of the focus point $\Delta x = f\Delta\theta$ (focal length f), such that a predefined pattern on the mirror can be addressed and elevated in a controlled way. The white light interferometer on the mirror front side is used to accurately measure the surface profile and it can also be used as feedback for subsequent sequences, if the structures are created iteratively.

2.5.1 | Mirror Composition and Physical Origin of Surface Microstructures

The mirrors used for the creation of micropotentials are composed of a fused silica substrate which is covered by a 30 nm thick layer of amorphous silicon, followed by the DBR coating consisting of a quarter-wave stack of 20 pairs of amorphous Tantalum pentoxide (Ta_2O_5) and Silicon dioxide (SiO_2). The substrate is superpolished to achieve a remaining surface roughness (rms) of 0.1 nm or better, to minimize scattering losses and to allow for defect free resonator modes. The thin silicon layer on top of the substrate absorbs light from a focused laser beam at 532 nm wavelength, which is the key feature to enable the structuring of the mirrors. For the commercial production of the mirror coating, the dielectric materials are slowly grown on the substrate by focused ion beam sputtering [115], where e.g. argon ions are accelerated onto a target consisting of the coating material. Single atoms are released (sputtered) from the target and then deposited on the surface of the sample. During this process some of the argon atoms are embedded in the dielectrics which is one of the mechanisms that lead to mechanical stress in the coating [116]. Such defects in the amorphous crystal structure, which are especially prominent in Ta_2O_5 thin films, can be annealed by subsequent heating to release the mechanical energy and promote the formation of small pores, which is accompanied by a slight increase in the film thickness of a few percent [117, 118]. In the method used in this work, absorption of focused laser light in the silicon layer activates this annealing process locally and only for a few of the bottom layers, so that the highly reflective surface quality of the mirror remains seemingly unaltered [35, 119]. The precise control of the local film thickness then allows to create variably shaped surface profiles, which translate into a local variation of the cavity length and therefore provide a trapping potential for light, cf. sec. 2.3.2.

2.5.2 | Mirror Structuring and Test Setup

Figure 2.6 shows a simplified sketch of the setup used to create and optically test the mirror surface profiles. A blank mirror piece is mounted in a mirror holder on top of a three-axis stage and positioned in the focus of a microscope objective. A continuous wave (CW) laser beam at 532 nm wavelength is chopped into ~ 10 µs long pulses of adjustable power using an acousto-optical modulator and afterwards laterally deflected via a galvanometer-scanner. This device is used for beam-steering and it is built by two perpendicularly oriented mirrors, whose tilt angles can be controlled independently by applied voltages. The microscope objective focuses the laser beam through the mirror substrate onto the silicon layer to a spot size of ~ 1 µm FWHM and transforms the angle-steering into a spatial scanning of the laser beam. A motion sequence and a pulse pattern is programmed for the laser beam and then the surface is carefully elevated to the desired target profile. This can be done either in a single sequence or in an iterative approach, with the latter typically giving much better end results. Typical mean deviations between the target and the structured profile of ~ 0.1 nm can be achieved in this way [35]. The structures are limited to surface heights below 20 nm to preserve the good mirror quality. While higher structures are in principle possible, the mirrors then exhibit a larger transmission and trapping potentials seem to be ineffective for heights larger than ~ 25 nm [109].

The structured mirror surface is analyzed from the front side by white-light, phase shifting interferometry, using a Mirau-objective, which has an inbuilt reference path to interfere light reflected from the sample [120]. The measurement is performed by moving the mirror along the optical axis over a distance of ~ 1 µm over the timescale of a few seconds. A camera continuously records images of the mirror surface with the superimposed interference pattern. In the analysis, relative phase differences across the investigated surface can be extracted from the recorded intensity profile for every pixel on the camera sensor. These phase differences correspond to height differences by $\Delta\phi(\mathbf{x}) = k\Delta h(\mathbf{x})$, with $k = 2\pi/\lambda$ and λ is the centre wavelength of the broadband light source, which then allows to reconstruct the surface profile. The lateral resolution of the setup is 0.74 µm and the minimum resolvable height differences are 0.1 Å [35]. Due to heat diffusion in the thin films, the minimum width of point-like structures is limited to 3.6 µm FWHM, which implies a significant smoothing of the created structures, such that sharp edges are generally hard to realize.

2.5.3 | Finite Difference Method

In many interesting resonator geometries, the complexity of the trapping potential may not allow to calculate the exact analytical solutions of the Schrödinger equation. In these cases only approximate wave functions can be given. If a more precise solution is needed, the Schrödinger equation can however be solved numerically, which can provide very good estimates of the mode functions and energies for a given trapping potential.

For simplicity the following discussion will be restricted to one-dimensional problems, but the method can be generalized also to higher dimensions [121]. In order to obtain a numerical solution, the eigenvalue problem in eq. (2.27) is discretised on a uniform spatial grid, consisting of N grid points $x = (x_1, x_2, \ldots, x_N)$. The wave functions are correspondingly represented as vectors on this grid, i.e.

$$\psi(x) = \begin{pmatrix} \psi(x_1) \\ \psi(x_2) \\ \vdots \\ \psi(x_N) \end{pmatrix} . \tag{2.63}$$

In order to solve the eigenproblem, the Hamiltonian $\hat{H} = \hat{T} + \hat{V}$ then has to be expressed as a matrix operator of dimensions $N \times N$. The potential energy operator is given by a diagonal matrix with the elements of V at each grid point x_i, so

$$\hat{V}(x) = \begin{bmatrix} V(x_1) & \cdots & \cdots & 0 \\ \vdots & V(x_2) & & \vdots \\ \vdots & & \ddots & \vdots \\ 0 & \cdots & \cdots & V(x_N) \end{bmatrix} . \tag{2.64}$$

Intuitively, without kinetic energy in the system, the energy at point x_i would just be $V(x_i)$. For the kinetic energy, the second derivative ∇_x^2 has to be expressed as a matrix operator. Recalling that the derivative of a discretised function at a point x_i can be approximated by the difference between neighbouring function values around this point, the second derivative can be expressed in this finite-difference approximation as [122]

$$\nabla_x^2 \psi(x_i) = \frac{\psi(x_{i-1}) - 2\psi(x_i) + \psi(x_{i+1})}{(\Delta x)^2} \tag{2.65}$$

with the spacing between grid points Δx. With this result at hand, the kinetic energy can now be cast into a matrix operator $\hat{T}$ which yields the second derivative of the wave function at every grid point if applied to $\psi(x)$. This kinetic energy operator takes the form

$$\hat{T} = -\frac{\hbar^2}{2m_{\mathrm{ph}}(\Delta x)^2} \begin{bmatrix} -2 & 1 & \cdots & 0 \\ 1 & -2 & 1 & \vdots \\ \vdots & 1 & \ddots & 1 \\ 0 & \cdots & 1 & -2 \end{bmatrix} . \tag{2.66}$$

Finally the eigenvalue problem in eq. (2.27) can now be implemented on a computer and numerical eigensolvers can be employed to find the solutions in terms of the wave functions and eigenenergies. So far the discussion excluded the photon rest mass energy, i.e. the eigenenergies obtained by this numerical calculation are given relative to the point of zero potential energy. If the real photon energies are required, the rest mass term has to be added to the calculated eigenenergies.

Even though the computation is straightforwardly set up, it can be numerically time consuming to find all solutions of large scale problems, especially for two-dimensional potentials which can comprise several thousands of bound states. Therefore it should be generally advised for potentials, that can over the most part be decently approximated by symmetric profiles with known analytic solutions, that the finite-difference method should merely serve as an extension to compute numeric solutions. This numerical method can then be an instrumental tool, for example around the minimum of a potential geometry, where the details of the potential profile have a profound influence on the resulting eigenenergies and wave functions.

Chapter 3 | Experimental Setup

The following chapter explains the main parts used to perform the experiments described in this work. The heart of the experiment is formed by a dye filled microcavity, which is depicted in the centre of the simplified sketch in fig. 3.1(a). Both cavity mirrors are mounted on stages equipped with piezoelectric actuators such that the needed accuracy for the control of the cavity length and the relative mirror orientation can be achieved. The interference pattern produced by a Helium Neon (HeNe) laser transmitted through the cavity, helps for the coarse parallel alignment of the mirrors. If a microstructured mirror is used for the experiment, it is placed on the site opposite to the pump beam, so that the incoupling of the pump light is not impaired by the silicon layer between the dielectric Bragg coating and the mirror substrate. The unstructured mirror on the other side of the cavity is glued onto a glass substrate and one right-angled glass prism on either side of the substrate helps to avoid refraction of the pump beam at the air glass interfaces. In this way, a good incoupling efficiency of the pump at an angle near the mirror coating's reflection minimum of 45° can be obtained.

3.1 | Pumping of Dye Molecules

A linearly polarized CW laser operating near 532 nm wavelength is used as the optical pump source to excite the dye molecules in the microcavity. Upon passing a first AOM, the laser beam is chopped into rectangular, constant power pulses of variable temporal width. Typically used parameters are pulse lengths of 500 ns at a repetition rate of 50 Hz. Compared to the timescale of thermalisation and photon dynamics inside the cavity, this realizes conditions of quasi-CW operation while the detrimental effect of photobleaching in the dye molecules can be reduced to a minimum, however a slight decrease of the fluorescence yield over time is usually observed due to the long-lived triplet states (see sec. 2.2.2). A second AOM serves to relieve this problem by transforming the pump pulse such that it slowly increases in power over the pulse length, see fig. 3.1(b). This compensates for the photobleaching in the dye and the pulse of photons emitted from the cavity is nearly constant over time once a steady state is reached. The pump pulse is adjusted in a way that this steady state is realized for the duration of $\tau_{\text{pulse}} \approx 500\,\text{ns}$, see fig. 3.1(c). Also the pump power and therefore the photon number in the cavity can be adjusted by the second AOM by controlling the power of the applied RF-signal. After the two AOMs, the pump beam passes a half-wave plate to guarantee that the pump light is s-polarized for maximum transmission through the cavity mirror coating. Behind the half-wave plate, a telescope with a pinhole at the focal point of the first lens is used to clean up the spatial pump profile and to control the pump size in the cavity. The latter is achieved by mounting the collimating lens on a translation stage, such that the beam can be adjusted to be slightly divergent or convergent after the telescope, which leads to a different diameter of the pump beam in the cavity plane. A piezo-adjustable mirror mount is used for precise positioning of the pumpspot before it is focused into the cavity by a final lens of exchangeable focal length. A flip mirror in front of the cavity can be used to image the pump beam onto a CCD camera, which is positioned in an optically equivalent plane as the cavity, such that the

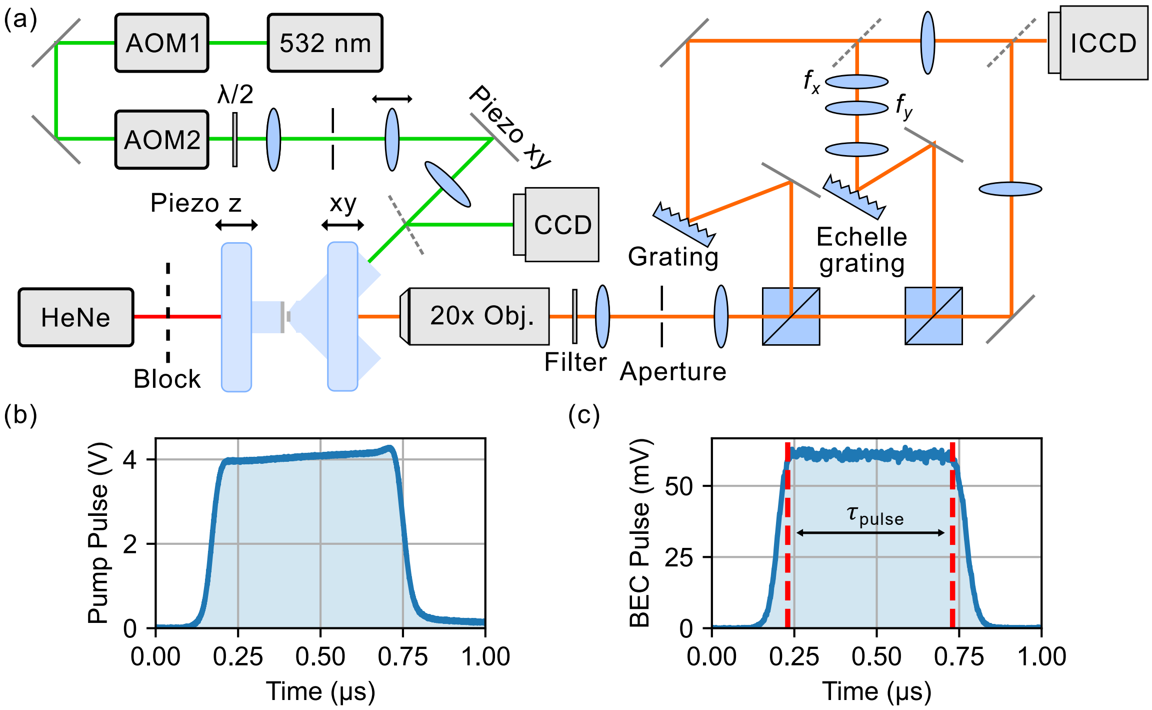

Figure 3.1: **(a)** Simplified sketch of the experimental setup. The pump laser beam at 532 nm wavelength is drawn in green. Before being coupled into the microcavity, it passes through a pair of AOMs, a wave plate and a telescope in order to optimize the temporal and spatial pulse shape as well as the incoupling efficiency into the cavity. The cavity mirrors are mounted on piezo stages, which are needed for the precise alignment of the cavity length and the relative mirror orientation. The HeNe laser and the piezo-adjustable mirror mounts allow for the relative alignment of the cavity mirrors. The emitted light from the cavity (orange) is collected by a microscope objective and passes an optical filter. The cavity emission can then be guided through a low resolution, broadband or a high resolution, narrowband Echelle spectrometer or it is directly imaged onto an ICCD camera to measure the spectral and spatial density distribution of photons in the microcavity. **(b)** Photodiode signal of the pump pulse recorded after the second AOM. The pulse is not a flat-top but it slightly ramps up in power over time to compensate for photobleaching of the dye molecules. **(c)** The signal emitted from the cavity for the pump pulse shown in **(b)**, recorded with a photomultiplier. The measured pulse is flat in time over the period marked by the two red vertical lines, which defines the pulse length where steady state conditions in the cavity are realized, here over $\tau_{\text{pulse}} \sim 500\,\text{ns}$.

shape and size of the pump beam can be monitored.

3.2 | Analysis of the Microcavity Emission

In order to spectrally and spatially analyse the microcavity emission, a microscope objective with 20x magnification and numerical aperture of 0.42 collects the emission from the cavity before it passes through a pair of optical filters to block residual pump light and fluorescence for wavelengths greater than 600 nm, for which the cavity mirrors are nearly transparent. An aperture in the image plane behind the objective is used to constrain the field of view for the analysis setup, for example to suppress any light emitted from outside a well defined potential structure. The remaining setup consists of two different grating spectrometers and a direct path for imaging the cavity emission onto an intensified CCD (ICCD) camera. The two spectrometers differ mainly in the diffraction grating that is used to disperse the light. One of them uses a standard blazed grating with 1200 lines per mm and an angular dispersion of 1.25 mrad/nm. This spectrometer is used to record the full broadband spectra over a bandwidth of ~ 50 nm. The second spectrometer uses an Echelle grating with 316 lines per mm and an angular dispersion of 0.69 mrad/nm. This diffraction grating is optimized to be used at large diffraction orders near the Littrow configuration [123] and in the experiment it is aligned for the 11th diffraction order which gives an actual dispersion of 7.6 mrad/nm (see eq. (3.3)) [124]. This is almost an order of magnitude more than what can be achieved with the broadband spectrometer, so that a resolution of $\Delta\nu \sim 20$ GHz can be obtained, however at the trade-off of a limited bandwidth. This spectrometer is used to measure the individual populations of photons in low energy modes, close to the cavity cutoff. An intermediate telescope behind the Echelle grating, where the objective lens is replaced by two perpendicularly oriented cylindrical lenses with different focal lengths can be used to independently adjust the magnification in the transverse x- and y-directions. The direct imaging path is used to record the spatial density distribution of photons in the microcavity.

An ICCD camera is used for both the spectral and the spatial density measurements. Such an intensified camera consists of two main components, an image intensifier unit and a CMOS camera (in this thesis it will be anyway referred to as ICCD camera). In a first stage, incident photons are converted into photoelectrons at the photocathode of the intensifier unit. These electrons are accelerated and multiplied with the help of a microchannel plate which achieves a gain of the electric signal, typically in the range of ~ 1000. After undergoing multiplication, the electrons are guided onto a phosphor screen where they are converted back into photons by phosphorescence. This optical signal is then imaged onto the CMOS-camera chip. The intensifier can be gated over time windows typically as short as a few ns, which allows for excellent signal-to-noise ratios and great suppression of counts caused by spurious background photons despite the comparably much longer minimum exposure time of the CMOS camera, which is typically ~ 1 µs. An ICCD camera is therefore very practical for low light imaging applications.

3.3 | Measurement of Spatial and Spectral Density Distributions

As for all experiments with light trapped in cavities, the outcoupled photons from the cavity are characterized by the same properties as light currently populating the cavity. It is therefore possible to directly measure the photon properties inside the cavity by collecting the emitted light and analysing it in the suitable way to extract the physical quantities of interest. High numerical aperture objectives covering large solid angles are used to efficiently capture most of the light coming from the cavity, which is crucial to achieve the best possible resolution.

3.3.1 | Spatial Distribution

For photon condensates, all stationary system properties are in some way related to the mean distribution of photons over the many resonator modes. Under stationary conditions of operation, this distribution can be conveniently accessed by integrating the collected optical signal over time on a sensitive camera. A direct measure is given by the spatial distribution of photons, which implies imaging the magnified resonator plane onto the camera. The total density distribution can be written as the sum over all cavity mode functions weighted by the respective population of photons per mode

$$n(x,y) = \sum_m n_m |\psi_m(x,y)|^2 \,, \tag{3.1}$$

where n_m denotes the mean photon number in the m-th mode. In order to verify thermalisation of the photon gas, this distribution is compared with a Bose-Einstein distribution. Doing this for the two-dimensional distribution is possible, but a more comprehensive analysis is often achieved, from the vertically integrated distribution, i.e. from $n(x) = \int n(x, y)\,\mathrm{d}y$. A measurement of the spatial density distribution however does only allow to measure the full distribution, and individual populations per mode can not be determined due to the spatial overlap between different mode functions.

3.3.2 | Spectral Distribution

The information obtained from the spatial distribution of photons can be compared to the spectral density distribution. The measurement is performed with the help of an optical grating spectrometer. While this is a very established way of measuring optical spectra, a few important details need to be considered to understand how the measured spectrum relates to the actual photon distribution inside the cavity.

The working principle of a diffraction grating spectrometer in $4f$-configuration is sketched in fig. 3.2(a). The light source is placed into the real space input plane of the spectrometer. A lens of focal length f_1 serves to collimate the emitted light and a diffraction grating placed into the back focal plane of this lens disperses the photons according to the different spectral components. The image of the dispersed light source is then reconstructed on the detector in the output plane by a lens of focal length f_2. The starting point to determine the spectrometer resolution is the grating equation with the condition for constructive interference

$$g\left(\sin\theta_i + \sin\theta_r\right) = u \cdot \lambda\,. \tag{3.2}$$

Here g is the grating constant, θ_i is the angle of incidence, θ_r is the diffraction angle and u is the diffraction order for light of wavelength λ [125]. The angular dispersion is obtained by differentiation of both sides of this equation w.r.t. the diffraction angle, which gives

$$\left(\frac{\mathrm{d}\lambda}{\mathrm{d}\theta_r}\right)^{-1} = \frac{u}{g\cos\theta_r} := \delta\,. \tag{3.3}$$

According to the Rayleigh-criterion [126], the diffraction limited minimum difference between optical wavelengths, that can be resolved by the grating, is determined by the used diffraction order and the number of illuminated grooves N by

$$\Delta\lambda_{\mathrm{min}}^{\mathrm{grating}} = \frac{\lambda}{uN}\,. \tag{3.4}$$

Assuming now that the light source is of transversal width w in the input plane (with coordinates (x, y)) and it includes two spectral components split by $\Delta\lambda$, the image of the light source in the output plane behind the spectrometer (with coordinates (x', y')) is magnified by a factor $M = f_2/f_1$, so $w' = Mw$, and with the approximation of small diffraction angles, the separation of the two spectral components on the detector is

$$\Delta x' = f_2\tan\Delta\theta_r = f_2\tan\delta\Delta\lambda \approx f_2\delta\Delta\lambda\,. \tag{3.5}$$

The resolution of the spectrometer is ultimately limited to the case when $\Delta x' = w'$, so that one finds

$$\Delta\lambda_{\mathrm{min}}^{\mathrm{spec}} = \frac{w'}{f_2\delta} = \frac{w}{f_1\delta}\,. \tag{3.6}$$

Thus it is evident that in order to achieve a high spectral resolution, a grating with large angular

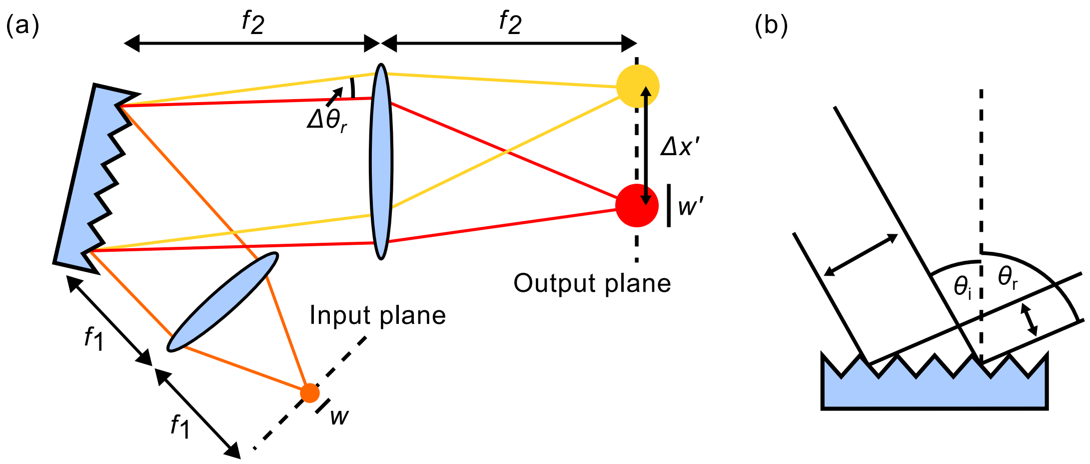

Figure 3.2: **(a)** Scheme of a diffraction grating spectrometer in $4f$-configuration. A light source of size w in the input plane (orange circle) is dispersed into its different spectral components by the grating before it is magnified to size $w' = \frac{f_2}{f_1} w$ and imaged into the output plane. Different components (red and yellow circles) are separated according to the angular dispersion δ and the difference in optical wavelength $\Delta\lambda$ by $\Delta x' = f_2 \delta \Delta\lambda$. They can be completely distinguished if $\Delta x' > w'$. **(b)** Illustration of the reason for the anamorphic magnification of the image along the axis of dispersion. In general $|\theta_r| \neq |\theta_i|$, so the diameter of a collimated beam changes in the course of diffraction by the grating surface.

dispersion and a long focal length lens for f_1 should be used, while the light source should be preferably of small size (cf. fig. 3.2(a)). Note that the spectrometer resolution can not beat the diffraction limited grating resolution, so if $\Delta\lambda_{\text{min}}^{\text{spec}} < \Delta\lambda_{\text{min}}^{\text{grating}}$, the spectrometer resolution is limited by the grating. In the opposite case the size of the light source is the limiting factor. This is the reason why commercial spectrometers often use adjustable entrance slits, which increases the achievable spectral resolution at the expense of losing optical throughput. This scheme is however not directly applicable for measurements on the here realized dye microcavity photon condensates, because an entrance slit of the spectrometer acts as a mode filter, which unequally attenuates the signal from different modes and therefore distorts the measured spectrum. There exist more elaborate methods, e.g. a technique sometimes referred to as *hyperspectral imaging*, where the image of the light source is transversally scanned over the entrance slit and in this way a spectrum can be recorded, which is almost completely decoupled from the spatial profile of the light source [127]. This method however can only be used to its full potential for light sources with little variations in their spectral and power characteristics, as it requires many consecutive measurements over the time span of at least a few seconds.

Analogously to the spatial density distribution, the measured spectral distribution in the output plane can now be written as

$$n(\lambda, x', y') = \frac{1}{M^2} \cdot \sum_m n_m \cdot |\psi_m(x'/M + \Delta x'(\lambda), y'/M)|^2 , \tag{3.7}$$

where the dependence on λ is implicitly included in $\Delta x'(\lambda) = f_2 \delta \Delta\lambda$. The wavelength difference $\Delta\lambda = \lambda - \lambda_0$ is measured relative to a reference wavelength λ_0, which could be the cutoff wavelength for example. In the argument of the mode functions $|\psi_m|^2$, it was explicitly written x'/M and y'/M, which is the operation performed by an optical telescope, i.e. it maps a function value at position x in the input plane to the point $x' = Mx$ in the output plane. The prefactor $1/M^2$ ensures that the mode functions remain properly normalized after magnification.

A detailed analysis of the spectrometer's imaging properties reveals, that the magnification in x- and y-direction is generally not the same, even if just usual symmetric converging lenses are used. While the simple expression for M used so far is correct for the y-direction, the projection of the incident and diffracted light beams onto the grating surface leads to a further magnification in the direction of dispersion, see fig. 3.2(b). This magnification is given by $M_x = \cos\theta_i / \cos\theta_r$. This effect is known as anamorphic magnification in the literature and it means that in practice two separate values for the magnification, M_x and M_y, have to be used [124, 128].

3.3.3 | The Measured Spectrum

Equation (3.7) implies, that the spatial mode functions $|\psi_m|^2$ are still contained in the resulting spectral distribution, so that the measurement at the output of the spectrometer yields an intricate convolution of the spectral and spatial photon distribution. What is then typically referred to as a spectrum in experiments on photon condensates, is the vertically integrated detector signal, i.e. $n(\lambda, x') = \int n(\lambda, x', y')\,\mathrm{d}y'$. For the purpose of a quantitative analysis of experimental data, it would be instructive to construct a model function that describes the measured spectrum for given parameters of the spectrometer, under the assumption that the photons inside the cavity follow a Bose-Einstein distribution. Such a function can be obtained numerically by calculating the mode functions (either analytically or as described in sec. 2.5.3) while the photon number for every mode is determined by the Bose-Einstein distribution, before the sum over all modes in eq. (3.7) is performed. For large scale two-dimensional problems this can be however numerically expensive, because it potentially involves the calculation of tens of thousands of modes. However, for the special case where the 2D wave functions are given by products of 1D wave functions, the complexity of this calculation can be reduced. The procedure of calculating the spectrum $n(\lambda, x')$ can then be facilitated significantly by exploiting the fact that the wave functions are normalized, i.e.

$$\psi_{n_x,n_y}(x,y) = \psi_{n_x}(x)\cdot\psi_{n_y}(y) \quad \longrightarrow \quad \int |\psi_{n_x,n_y}(x,y)|^2\,\mathrm{d}y = |\psi_{n_x}(x)|^2 . \tag{3.8}$$

In this case, the spectrum can be constructed exclusively from one-dimensional wave functions. As an example, consider the 2D harmonic oscillator level with quantum number $m = 2$. With the condition $m = n_x + n_y$ (see eq. (2.28)), there are three energetically degenerate states ($\psi_{0,2}$, $\psi_{1,1}$ and $\psi_{2,0}$) contributing to this level. Integration of the mode functions over y then implies that the total contribution of these states to the full spectrum is given by $|\Psi_2(x)|^2 = \left(|\psi_0(x)|^2 + |\psi_1(x)|^2 + |\psi_2(x)|^2\right)$. This principle can be generalized for the m-th oscillator level so that a simplified expression for the measured spectrum is obtained, i.e.

$$n(\lambda, x') = \sum_m n_m \cdot |\Psi_m(\lambda, x')|^2 \quad \text{with} \quad |\Psi_m(\lambda, x')|^2 = \frac{1}{M_x}\cdot\sum_{m'=0}^{m} |\psi_{m'}(x'/M_x + \Delta x'(\lambda))|^2 . \tag{3.9}$$

Fig. 3.3 illustrates how a measured spectrum looks like on the camera sensor. It shows calculated Bose-Einstein distributed spectra over the first 100 harmonic oscillator levels for two grating spectrometers with different angular dispersion. The exact agreement between the integrated two-dimensional spectrum and the one constructed starting from one-dimensional wave functions according to eq. (3.9) confirms the validity of the method. It is evident from the shown spectra, that for a small grating dispersion, the resolution is not sufficient to extract the photon number n_m per state, given their overlap.

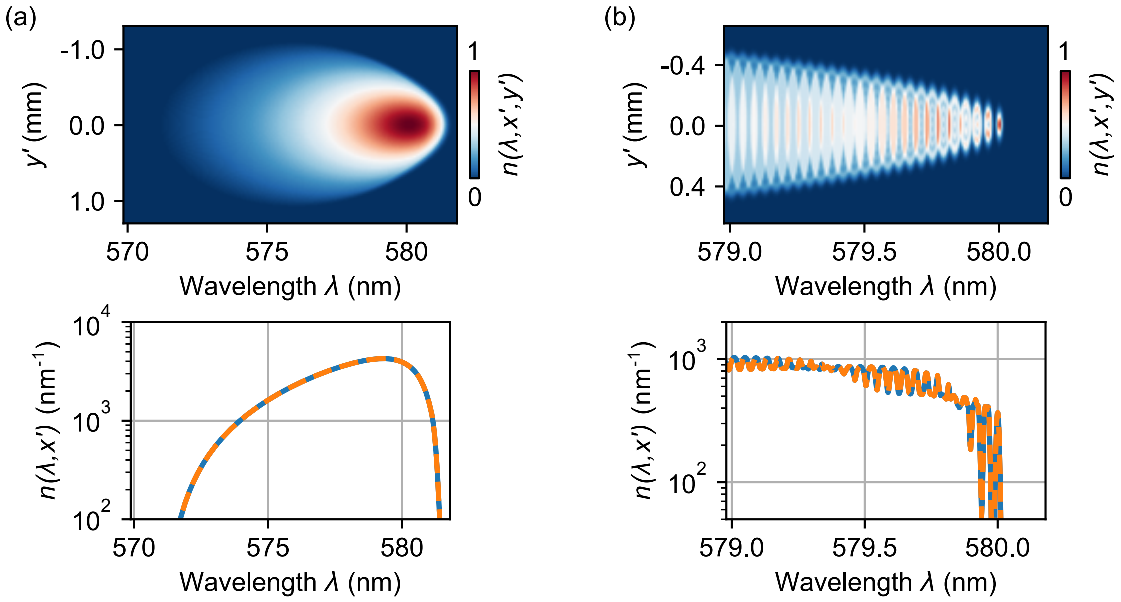

Figure 3.3: Theoretical spectral photon distributions over the lowest 100 levels in a 2D harmonic oscillator potential for a chemical potential of $\mu \cdot k_B T/\hbar = 10\Omega$, which would correspond to $\approx 85\%$ of the critical photon number for an infinitely deep potential (other parameters are $R = 1$ m, $q = 8$, $\Omega = 2\pi \cdot 36.9$ GHz). The ground state is set to the cutoff wavelength of $\lambda_c = 580$ nm. **(a) Top panel** Peak normalized spectral density distribution as it would be measured on a camera with an optical magnification of $M_y = 10$, $M_x = 11$ (the difference here is just due to the anamorphic magnification), and an angular dispersion of the grating of 1.25 mrad/nm. **Bottom panel** Vertically integrated spectral density (blue, solid) and the spectrum as calculated from eq. (3.9) (orange, dashed). For convenience the horizontal axis is only labelled by wavelength λ and the dependence on x' is omitted here. The spectrum drops for wavelengths smaller than ~ 573 nm due to the finite range over which it is computed. **(b) Top panel** Same parameters as in (a) but for a dispersion of 7.6 mrad/nm and magnification of $M_y = 9$, $M_x = 6$ (anamorphic magnification). This gives a large enough spectrometer resolution, such that the first few harmonic oscillator states can be distinguished. The mode functions appear squeezed along the horizontal axis due to an aspect ratio (height/width) of 3 for the figure grid points. **Bottom panel** Integrated and calculated spectrum analogous to (a).

On the other hand, employing the high resolution spectrometer (fig. 3.3(b)) allows for a good separation of the more confined low energy modes, although higher and more spatially extended modes still overlap. Most importantly, the ground mode population could be determined in this example case.

The described method of calculating the spectrum therefore conveniently allows the definition of a fitting function for given parameters of the spectrometer and a given trapping potential, which is instrumental for the evaluation of experimental data. All spectra presented in this work are analysed making use of this method.

3.4 | Average Photon Number in the Cavity

A very important parameter for the characterization of photon condensates is the (critical) photon number in the cavity, which is specific for a given trapping potential (cf. eq. (2.31)). For this reason, it should be accurately measured. The mean photon number inside the cavity can be accessed from time integrated measurements of the signal emitted from the cavity following some simple considerations.

Assume that there are photons at wavelength λ populating the cavity. The optical power circulating in the cavity at this wavelength is then given by

$$P_{\mathrm{c}}(\lambda) = \frac{n(\lambda)h\nu}{\tau_{\mathrm{RT}}} \tag{3.10}$$

with the number of photons $n(\lambda)$, the round-trip time $\tau_{\mathrm{RT}} = 2\tilde{n}L/c$, and $\nu = c/\lambda$. If the outcoupling cavity mirror has the transmission $T_s(\lambda)$, the measured optical power at the camera would be

$$P_{\mathrm{cam}}(\lambda) = T_s(\lambda)T'P_{\mathrm{c}}(\lambda)\,. \tag{3.11}$$

Here T' is the combined transmission of all other optical elements between the cavity and the camera. During a measurement, several camera images integrated over consecutive pulses with a temporal width of τ_{pulse} are recorded. The number of photons arriving at the camera is given by

$$n_{\mathrm{cam}}(\lambda) = \frac{\tau_{\mathrm{pulse}}}{h\nu}P_{\mathrm{cam}}(\lambda) \tag{3.12}$$

and taking into account some finite detection efficiency η of the camera, one can write

$$n_{\mathrm{sig}}(\lambda) = \eta \cdot n_{\mathrm{cam}}(\lambda) = \eta \cdot \frac{\tau_{\mathrm{pulse}}}{h\nu}P_{\mathrm{cam}}(\lambda)\,. \tag{3.13}$$

Substituting (3.11) into this expression gives

$$n_{\mathrm{sig}}(\lambda) = \eta \cdot T'T_s(\lambda)\frac{n(\lambda)\tau_{\mathrm{pulse}}}{\tau_{\mathrm{RT}}} = A \cdot T_s(\lambda)\frac{n(\lambda)\tau_{\mathrm{pulse}}}{\tau_{\mathrm{RT}}} \tag{3.14}$$

where the finite detection efficiency and optical elements' transmission were merged into a common proportionality constant A in the last step. This equation relates the photon number in the cavity $n(\lambda)$ to the measured signal $n_{\mathrm{sig}}(\lambda)$. The parameter A can be calibrated with the help of a weak cw laser and gating the camera over a time interval τ_{gate}, which is comparable to the photon pulse width. Assume there is the optical power $P(\lambda_{\mathrm{cal}})$ at wavelength λ_{cal} incident onto the outcoupling cavity mirror. Following the discussion from above, the expected signal measured on the camera is

$$n_{\mathrm{sig}}(\lambda_{\mathrm{cal}}) = A\frac{\tau_{\mathrm{gate}}T_s(\lambda_{\mathrm{cal}})}{h\nu_{\mathrm{cal}}}P(\lambda_{\mathrm{cal}})\,, \tag{3.15}$$

so that A can be determined by performing such a measurement for several different laser powers. This method of calibrating the camera signal versus the cavity photon number is very robust because for the eventual use in the analysis, only parameters which are quite accurately known remain in the equation. The least well known quantity is probably the exact mirror transmission $T_s(\lambda)$. However solving eq. (3.15) for A, it is clear that $A \propto 1/T_s(\lambda_{\mathrm{cal}})$. Inserting this into eq. (3.14) gives the ratio $T_s(\lambda)/T_s(\lambda_{\mathrm{cal}})$, indicating that the exact mirror transmission does not need to be known, as only the relative transmission between the laser wavelength used for calibration and the condensate wavelength is important. This is very convenient, because it can be difficult to determine the exact mirror transmission on the scale of a few ppm with sufficient accuracy, such that the calculated theoretical values provided by the manufacturer are sufficient for this purpose.

Chapter 4 | Condensation Threshold

As was mentioned at the end of sec. 2.4, the question whether or not photon Bose-Einstein condensation can be realized in the dye-filled microcavity, depends on the competing timescales of photon absorption Γ_{12} and cavity losses κ. If the mean absorption time of photons is much shorter than their loss from the cavity by transmission through the mirrors, a near equilibrium distribution can be obtained and BEC should be observed upon reaching a critical photon number. It has been thoroughly investigated, both experimentally and theoretically, under steady state and time-resolved dynamical conditions how photon thermalisation is or is not achieved, depending on the ratio between κ and Γ_{12} [12, 40, 89, 90]. Both parameters can be directly controlled by the cutoff wavelength in an experiment. Some authors introduce a dimensionless thermalisation parameter, $\gamma = \kappa/\Gamma_{12}$ [21, 90, 131, 132], which provides a measure for the degree of photon thermalisation. The regime of good thermalisation is identified by $\gamma \ll 1$ and a strongly occupied ground mode is then classified as a Bose-Einstein condensate. On the other hand, $\gamma \gg 1$ indicates the opposite regime of poor thermalisation, similar to the operating conditions of standard lasers. While a figure of merit of successful thermalisation can be obtained by the comparison of the energy distribution of non-condensed photons to a Bose-Einstein distribution, a very rigid test of thermalisation is the validation of fluctuation-dissipation theorems, which are expected to fit to ambient temperature for well thermalised systems [129] and which has been verified for the photon BEC for a cavity cutoff where $\gamma < 1$ [130].

In the following, the pump power required to reach the threshold of Bose-Einstein condensation ($\gamma \ll 1$) or lasing-like behaviour ($\gamma \gg 1$) is analysed. It is shown, that for the used experimental configuration, the crossover point between lasing and condensation (or poor and good thermalisation respectively) when varying the cavity cutoff wavelength is quite closely determined by the point at which the pump threshold reaches a minimum value. A corresponding model will be introduced in the following before an experimental measurement of the pump threshold will be presented.

4.1 | Pump Threshold for Photon Condensation

Considering just a single cavity mode (ground mode, $m = 0$), a gain coefficient can be defined in an analogous manner to the gain coefficient that was introduced for an ensemble of broadened two-level systems in eq. (2.20). For convenience the index $m = 0$ will be omitted in the following, so that all parameters refer to the ground state. Collecting all terms proportional to the photon number in eq. (2.38) and ignoring spontaneous emission [99], the change of the ground mode photon number n over time is

$$\frac{\partial n}{\partial t} = -\kappa n + \Gamma_{21} n f - \Gamma_{12} n (1 - f) =: \alpha_0 n \,. \tag{4.1}$$

The overlap integral of the molecular excitation profile with the ground mode profile is denoted by f here. The value of the gain coefficient α_0 determines whether the photon number in the cavity remains small ($\alpha_0 \ll 0$) or if laser oscillation can be self-sustained ($\alpha_0 \rightarrow 0$). The standard definition for the laser threshold condition is $\alpha_0 = 0$, which is obtained, when the excitation density in the gain medium is large enough, so that stimulated emission exactly compensates the loss of photons. This condition can be rearranged to obtain a threshold value for f, which is [94, 131]

$$f_{\mathrm{th}} = \frac{\Gamma_{12} + \kappa}{\Gamma_{21} + \Gamma_{12}} \approx \frac{1}{\Gamma_{\mathrm{sp}}} \int \Gamma_{\mathrm{p,th}}(\mathbf{x}) |\psi_0(\mathbf{x})|^2 \, \mathrm{d}\mathbf{x}\,, \tag{4.2}$$

with the threshold pump rate $\Gamma_{\mathrm{p,th}}(\mathbf{x})$. For the approximate equality of the RHS of eq. (4.2), a small excitation fraction was assumed (see eq. (2.57)). This approximation holds quite well, also up to the threshold point, because there is only a minor saturation in the dye molecules. The pump rate can be written as (see appx. A.1)

$$\Gamma_{\mathrm{p}}(\mathbf{x}) = \frac{P_{\mathrm{abs}}}{\hbar\omega_{\mathrm{p}}\rho_{\mathbf{x}} \int \Pi(\mathbf{x}) \, \mathrm{d}\mathbf{x}} \cdot \Pi(\mathbf{x}) =: \frac{P_{\mathrm{abs}}}{s} \cdot \Pi(\mathbf{x}) \tag{4.3}$$

where $\Pi(\mathbf{x})$ is the peak normalized (dimensionless) pump shape function and $P_{\mathrm{abs}} = \eta P$ is the absorbed pump power in the molecules. Using (4.3) in the RHS of (4.2) and introducing the pump beam overlap integral $F = \int \Pi(\mathbf{x}) \, |\psi_0(\mathbf{x})|^2 \, \mathrm{d}\mathbf{x}$, the terms can be rearranged to derive an expression for the needed pump power at threshold

$$P_{\mathrm{th}} = \frac{s}{\eta} \cdot \frac{\Gamma_{\mathrm{sp}}}{F} \frac{\Gamma_{12} + \kappa}{\Gamma_{21} + \Gamma_{12}} = \frac{s}{\eta} \cdot \frac{\Gamma_{\mathrm{sp}}}{F} \frac{1 + \gamma}{1 + \Gamma_{21}/\Gamma_{12}}\,, \tag{4.4}$$

with the thermalisation parameter $\gamma = \kappa/\Gamma_{12}$.

In order to obtain an idea of how the threshold pump power depends on the cavity cutoff in the experimentally relevant region of $\lambda_{\mathrm{c}} = 550 - 600\,\mathrm{nm}$, it is instructive to consider the nominator and denominator of eq. (4.4) separately, see fig. 4.1(a). The prefactor $s\Gamma_{\mathrm{sp}}/\eta F$ only depends very weakly on the cutoff, so it is assumed to be constant. The factor $1/(1 + \Gamma_{21}/\Gamma_{12})$ is an exponentially decreasing function for increasing cutoff wavelengths, which is a direct consequence of the Kennard-Stepanov relation. On the other hand, with the mirror stop band centred around 550 nm (cf. fig. 2.2(a), coating *LosGatos*), the nominator is a very flat function with $\gamma \ll 1$ for $\lambda_{\mathrm{c}} < 570\,\mathrm{nm}$ and $\gamma = 1$ is reached around $\lambda_{\mathrm{c}} \approx 583\,\mathrm{nm}$. Going to larger cutoff wavelengths, the nominator now steeply increases, owing to the decreasing absorption cross section and the approaching edge of the mirror stop band. As a result, the pump threshold exhibits a minimum around $\lambda_{\mathrm{c,min}} \approx 584\,\mathrm{nm}$. Note that the scaling with the cutoff obtained in the regime of good thermalisation is $P_{\mathrm{th}} \propto (1 + e^{\hbar(\omega_{\mathrm{zpl}} - \omega_c)/k_{\mathrm{B}}T})^{-1}$, which should be expected from the critical excitation fraction for an equilibrium system, that was derived in sec. 2.4.6.

A perhaps more intuitive understanding of the pump threshold as a function of the cutoff wavelength can be obtained by expressing eq. (4.4) in terms of the photon absorption time $\tau_{\mathrm{abs}} = 1/\Gamma_{12}$ and the cavity lifetime $\tau_{\mathrm{cav}} = 1/\kappa$ which together determine the total photon lifetime by $1/\tau_{\mathrm{phot}} = 1/\tau_{\mathrm{abs}} + 1/\tau_{\mathrm{cav}}$. The pump threshold then takes the form

$$P_{\mathrm{th}} = \frac{s}{\eta} \cdot \frac{\Gamma_{\mathrm{sp}}}{F_0} \cdot \frac{1}{\tau_{\mathrm{phot}} \cdot (\Gamma_{21} + \Gamma_{12})}\,. \tag{4.5}$$

κ, Γ_{12} and $1/\tau_{\mathrm{phot}}$ are plotted in fig. 4.1(b). The photon lifetime exhibits a maximum around $\lambda_{\mathrm{c}} = 585\,\mathrm{nm}$ which is due to the interplay of increasing cavity losses for larger cutoffs and increasing absorption for smaller cutoffs. The sum of the absorption and the emission rate, $\Gamma_{21} + \Gamma_{12}$, is dominated by the emission rate and it is a slowly increasing function towards smaller cutoffs (cf. fig. 2.1(a)), such

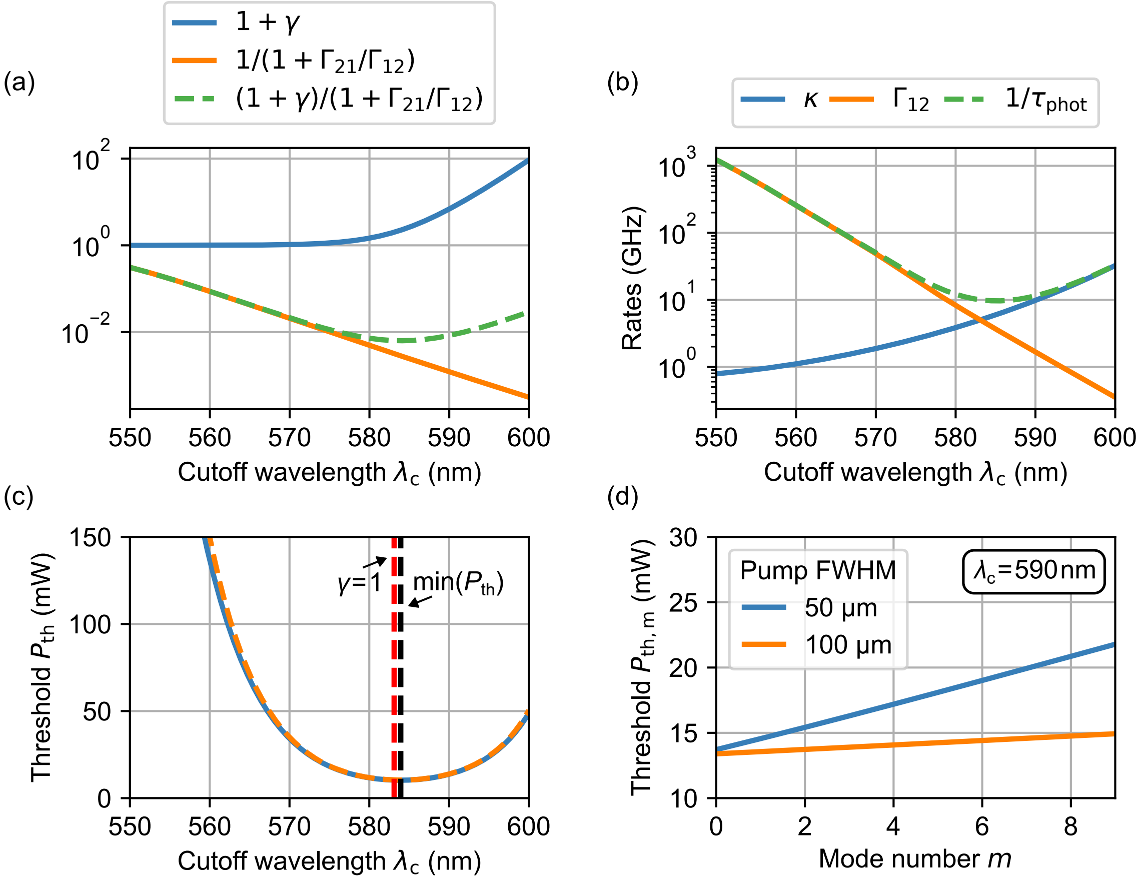

Figure 4.1: **(a)** Calculated parameters in eq. (4.4) and their ratio vs. cavity cutoff wavelength (dye concentration 1 mmol/l, $q = 8$). **(b)** Cavity loss rate, absorption rate and inverse photon lifetime vs. cavity cutoff. For small wavelengths (good thermalisation) the photon lifetime is determined by the absorption time while for large wavelengths (poor thermalisation) it is determined by the cavity lifetime. **(c)** Calculated ground mode pump threshold from eq. (4.4) (solid blue) and numerical pump threshold obtained by solving the rate equations (dashed orange) for a pump size of 50 µm FWHM . When tuning the cutoff closer to the dye zero phonon line ($\lambda_{zpl} = 545$ nm), the approximation of a small excitation fraction from eq. (2.57) loses accuracy, so that a slightly larger pump power is required to reach the threshold, compared to the analytical threshold power. The cutoff wavelengths at $\gamma = 1$ and for the minimum pump threshold are marked. **(d)** Calculated pump threshold for the first 10 modes at the cutoff $\lambda_c = 590$ nm for two different pump sizes. The curve is more flat for the larger pump beam, which implies a larger gain competition among the modes.

that the minimum pump threshold is slightly shifted towards a smaller cutoff relative to the cutoff of maximum photon lifetime.

While the pump threshold for large cutoffs is determined by cavity losses, one can intuitively understand the scaling for small cutoffs, by considering that the number of excitations in the cavity, i.e. excited molecules plus photons, is determined by the pump power. If the cavity is tuned closer to the dye zero-phonon line where the molecules become more absorptive, the excitations are predominantly stored in the molecules [130], such that the required pump power to maintain a constant photon density in the cavity increases [101].

To summarize the discussion so far, fig. 4.1(c) shows the calculated pump threshold for a 1D harmonic oscillator potential (two mirrors with radius of curvature $R = 1$ m) with a Gaussian pump beam of 50 µm FWHM. Also shown is the numerically calculated threshold power, which is obtained by solving the rate equations for different pump powers and then identifying the power, where the derivative $\frac{\mathrm{d}\log n}{\mathrm{d}\log P}$ (ground mode photon number n) exhibits a maximum [133]. This single-mode threshold criterion works independently of the exact energy distribution of photons in the cavity. The good agreement between the analytical and the numerical result justifies the approximations made in the derivation of eq. (4.4). The cutoffs at the minimum pump threshold and for $\gamma = 1$ are marked by red and black dashed vertical lines, respectively. As the two cutoffs are evidently almost identical, a measurement of the pump threshold here can be used to approximately identify the transition point between the regimes of good and poor thermalisation. It should be noted however, that this statement is only valid for the experimentally used mirror transmission profile, which exhibits a steep increase when approaching the edge of the stop band at large cutoffs. For mirrors with a uniform transmission profile for instance, as studied in [90], the pump threshold becomes a much flatter function of the cavity cutoff wavelength, so that the wavelengths of minimum pump threshold and $\gamma = 1$ can be quite separated.

4.1.1 | Background Decay and Pump Size

So far the dependence of the pump threshold w.r.t. the cavity cutoff has been discussed. However, also the prefactor in eq. (4.4) deserves to be briefly analysed. Addressing the background decay rate Γ_{sp} first, the pump threshold exhibits a linear scaling. This implies that the pump threshold can be reduced by suppressing spontaneous losses, since pump induced excitations are then converted into photons in the cavity more efficiently. This is a well established concept for wavelength sized cavities in order to reach very small thresholds and achieving nearly thresholdless lasing [134, 135].

The inverse scaling of the ground mode threshold with the pump beam overlap integral, F, generally implies that the threshold power increases for larger pump sizes, simply because this corresponds to a lower pump intensity [17, 90]. For a multimode cavity, as is the case for the photon BEC experiments, one could also consider a pump threshold (or gain coefficient) for each mode separately. The competition between modes is especially noticeable in the regime of poor thermalisation for large pump sizes, where the gain for higher modes can be comparable or even be larger than that experienced by the ground mode. This can result in multimode condensation or condensation (lasing) in one of the excited states, which is then similar to the self-tuning behaviour observed for lasers [88, 101]. Fig. 4.1(d) shows the calculated pump threshold for the first 10 harmonic oscillator modes with the cutoff fixed at $\lambda_{\mathrm{c}} = 590\,\mathrm{nm}$ for two different pump sizes. It is clear how the curve is much flatter for the larger pump size, which implies a stronger gain competition between the modes. The pump beam position and size correspondingly need to be adjusted carefully, as they can sensitively influence the produced photon distribution and determine which mode will show condensation [17, 85].

4.2 | Measurement of the Pump Threshold

In order to measure the pump threshold experimentally, the high resolution Echelle spectrometer is used. The cylindrical lens telescope shown in fig. 3.1(a) is replaced by a conventional telescope, as only a small part of the full spectrum needs to be imaged onto the ICCD camera. The Echelle spectrometer allows to separate the ground mode signal from the rest of the modes, see fig. 4.2(a). The averaged spectrum of 50 consecutive pulses is recorded for a constant pump power. The distinct ground mode peak can be fitted by a Gaussian afterwards, which makes the integration of the total signal straightforward. This procedure is repeated for many different pump powers around the condensation threshold, yielding a typical plot of the ground mode intensity versus pump power as shown in fig. 4.2(b). Below the pump threshold, the signal builds up slowly with increasing pump power and, above the threshold, it shows the conventional near linear scaling with increasing pump power. However, the

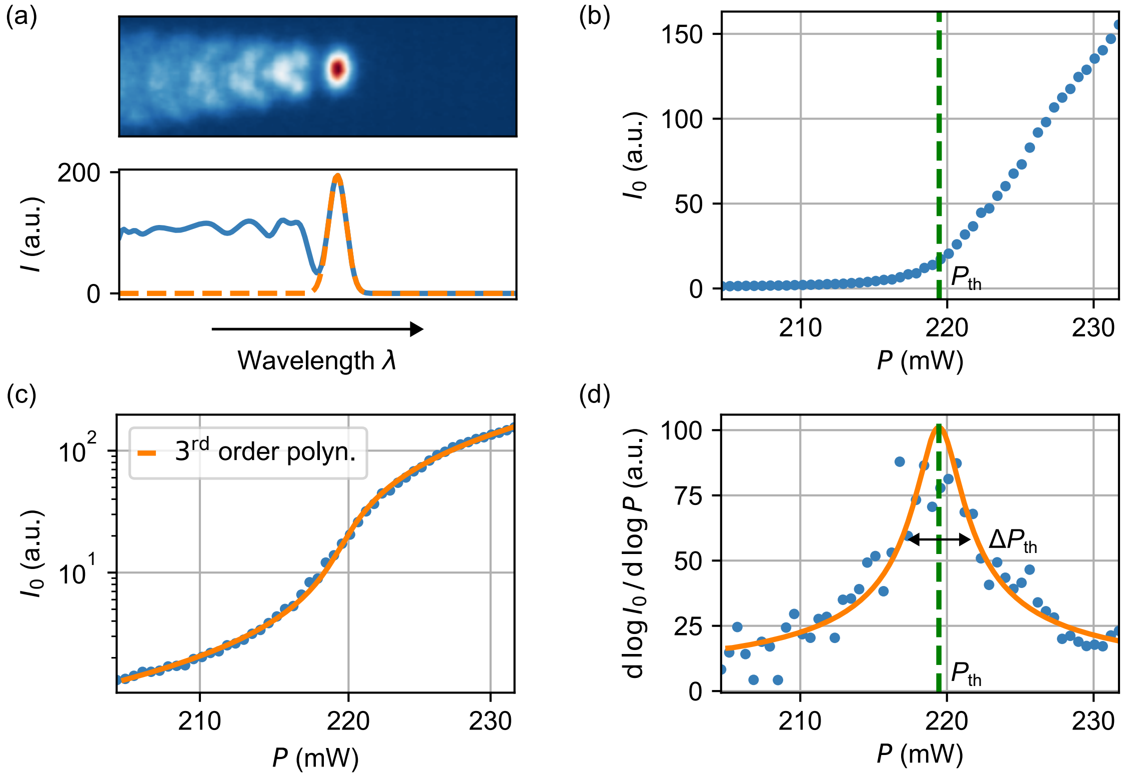

Figure 4.2: **(a)** Exemplary spectrum recorded with the Echelle grating spectrometer. The ground mode can be well separated from the higher energy modes and the intensity in the ground mode is extracted by integration of the fitted peak. **(b)** Input-output curve of the ground mode signal ($\lambda_c = 570\,\mathrm{nm}$, $q = 8$, $R = 1\,\mathrm{m}$), which shows the linear growth in intensity above a certain threshold power. **(c)** Same data as (b) represented in a log-log plot. There is almost no discernible difference for the power-axis in a linear or logarithmic scale, due to the small range over which the pump power is varied. The typical s-shaped input-output curve is interpolated by a cubic polynomial so that the derivative $\frac{\mathrm{d}\log I_0}{\mathrm{d}\log P}$ can be smoothly calculated, which is shown in **(d)**. The maximum of this derivative can be defined as the threshold and the width of the curve is a measure for the spread of the threshold region.

threshold point is not recognized very clearly, as is evident from the transition between the small and high signal regimes, which is extended over several mW of pump power, and the rather shallow growth of the photon number above the threshold. Such a behaviour is typical of small-scale lasers, which exhibit relatively large emission rates into the lasing mode, compared to laser cavities with sizes in the range of a few cm [136–138]. In a double logarithmic representation (fig. 4.2(c)) this correspondingly implies a rather weak bent of the s-shaped input-output curve [97]. The data points are numerically interpolated by a cubic polynomial, which is found sufficiently accurate to get a continuous function, that describes the ground mode signal versus pump power. The threshold power P_{th} is defined by calculating the maximum of the derivative $\frac{\mathrm{d}\log I_0}{\mathrm{d}\log P}$ (fig. 4.2(d)). This criterion generally gives consistent results for all kinds of lasers with different sizes [133] and it also works if the increase of the ground mode signal for large pump powers becomes nonlinear, as can be the case if the gain competition between different modes is significant (see fig. 4.3(b)). The width of the derivative around the threshold ΔP_{th} can be used as a measure for the uncertainty of P_{th}. A calibration of the spectrometer signal to convert the measured intensity into intracavity photon number is not required to determine the pump threshold.

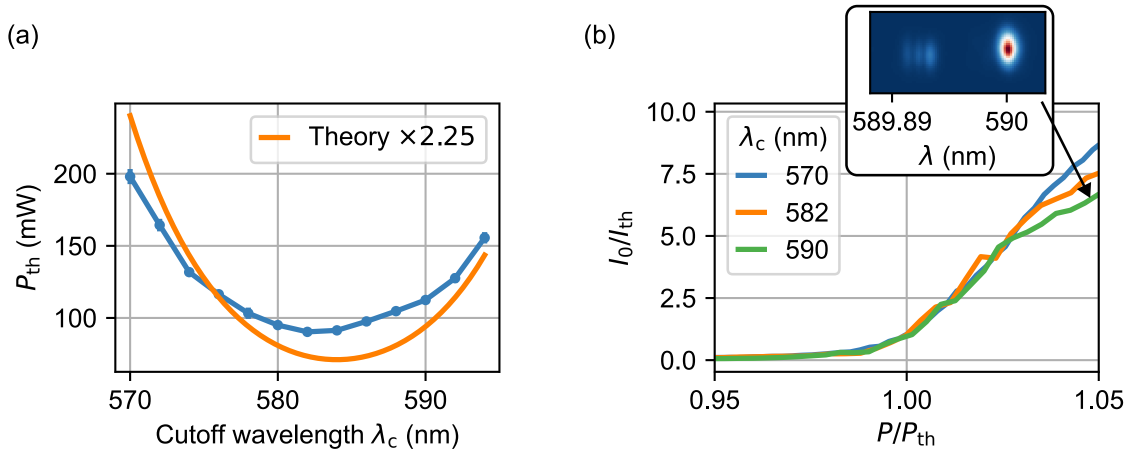

Figure 4.3: **(a):** Measured and calculated ground mode pump threshold versus cavity cutoff for $q = 8$. The theory curve obtained from eq. (4.4) is scaled by a factor of 2.25. **(b):** Normalized ground mode signal versus normalized pump power for different cavity cutoffs. The deviation of the near linear growth for increasing pump powers observed for $\lambda_c = 582$ nm and $\lambda_c = 590$ nm is due to the gain competition between multiple modes, see the inset, which shows the recorded spectrum at $P/P_{th} \approx 1.05$. In the regime of good thermalisation, the single-mode character is preserved deep into the condensed regime.

Fig. 4.3(a) shows the measured pump threshold for several different cutoffs between 570 – 594 nm at a pump size of 40 µm FWHM. Equation (4.4) is also plotted, however it is scaled by a factor of 2.25, such that the measured and calculated threshold powers fall into the same range. The absorbed pump power in eq. (4.4) is estimated under the assumption, that all of the incident power is transmitted through the incoupling mirror. This is probably a poor idealization, as it does not account for reflected pump light from the incoupling prism or a small mismatch w.r.t. to the optimum incoupling angle, therefore a scaling factor of 2.25 seems fairly reasonable. The qualitative dependence of the measured pump threshold as a function of the cavity cutoff strongly resembles the calculated expectation. The measured minimum threshold is slightly shifted towards smaller cutoff wavelengths, compared to the calculation, which could be explained by an overestimated absorption rate or an underestimated cavity loss rate in the theory. The cavity loss rate is the more likely candidate of the two to account for the observed discrepancy, as other loss channels than mirror transmission are neglected for κ, which is certainly not perfectly accurate. Another difference is that the measured threshold power exhibits a smaller curvature as a function of the cavity cutoff compared to the calculated curve. A possible explanation could also be found in a small deviation of the pump beam from the optimum incoupling angle, which results in a resonance condition for the pump beam. This can lead to partial destructive interference of the pump beam near the condensate position as a function of the cavity cutoff, which of course impacts the measurement of the threshold power. While setting up the microcavity, it is always attempted to minimize this effect by optimizing the transmitted pump power through the incoupling cavity mirror, however it can not be ruled out that a weak resonance effect for the pump light is still present in the experiment. This could also be the reason why such a strongly dependent relation between the pump threshold and the longitudinal mode number was observed in [91]. The overall agreement between the measured and the calculated threshold powers however, apart from the absolute values, confirms that the pump threshold can be used as an easily accessible measure to determine the crossover point where the thermalisation parameter is $\gamma \approx 1$, which is here found at $\lambda_c \approx 582.5$ nm.

A further (qualitative) feature, that is related to the thermalisation parameter, is how distinctively the single-mode character of the condensate is preserved for pump powers reaching into the condensed regime. This is illustrated in fig. 4.3(b), which shows the input-output curves for the cutoffs $\lambda_c = 570\,\mathrm{nm}$, 582 nm and 590 nm, with the signal and the pump power normalized by the threshold values respectively. Evidently, in the regime of good thermalisation at $\lambda_c = 570\,\mathrm{nm}$, the ground mode signal follows the near linear growth with increasing pump power up to a relative pump power of $P/P_{\mathrm{th}} \approx 1.05$ with a ~ 8-fold increase of I_0/I_{th}, while for the other cutoffs, a deviation from this linear dependence is observed at smaller relative powers and ground mode signals already. This is related to gain competition between different modes [21, 83, 131] and the achievable condensate fraction is larger in the regime of good thermalisation. However, the photon number regime explored in this measurement is usually not accessed experimentally, where the total photon number is typically not larger than two times the critical photon number. The observed behaviour would become more significant in the case of larger pump beams however, i.e. when the gain coefficient is a shallower function for different modes (cf. fig. 4.1(d)).

Concluding the chapter, it was discussed, that the relevant experimental tuning parameters, which determine how well the thermalisation of photons works, are the cavity losses and the absorption rates. Both the cavity losses and the absorption rates are a function of energy, so that the cavity cutoff allows to scan both parameters from the regime of good to poor thermalisation. Apart from the cutoff, changing the dye concentration also allows to modify the absorption rate and therefore tuning between the different regimes is also possible for a fixed cavity cutoff. However, the commonly used dye concentration of 1 mmol/l is already at the higher end of the usable concentrations, due to a limitation caused by dimerisation of dye molecules at high densities, which is accompanied by a degradation in quantum efficiency [139, 140]. For the typical mirror coatings used in the experiments on photon condensates, it was motivated that measuring the pump threshold for a given cutoff wavelength and comparing it to the minimum pump threshold, can be an indicator, whether the chosen experimental parameters fall into the regime of good photon thermalisation.

Chapter 5 | A Four-Site Lattice Unit Cell for Photons

The technique for permanent mirror surface structuring is used in this work to create a photon BEC in the ground state of a square lattice unit cell with four sites. Since thermalisation for photon condensates is achieved via the coupling to the thermal bath of dye molecules, the experiments can be directly performed in a potential geometry that allows for complex ground states. This distinguishes itself from the procedure used in cold atom experiments, where atoms are adiabatically loaded into optical lattices from a previously generated BEC [23]. The following chapter first introduces the basic physics of bosonic particles confined to a periodical potential. Important aspects are discussed on the design of a lattice unit cell for photons with four sites, such that the features of a periodic ground state can be resolved by the used imaging setup. A suitable surface structure is created on a cavity mirror and the resulting trapping potential is numerically and experimentally characterized. For the evaluation of experimental data, theoretical Bose-Einstein distributed spatial and spectral densities are constructed, taking into account the energies and spatial profiles of the cavity eigenmodes.

5.1 | Bosons in Periodic Potentials

In order to understand the origin of the resonator eigenmodes in a periodic potential, as studied in this work, one can get a decent intuition by considering the simple model of a bosonic particle confined to a one-dimensional periodically closed lattice. The modulation period is a and the length of the (circular) system is given by L with the periodicity requirement that $L = N \cdot a$, where N is an integer, that gives the number of lattice sites along the ring. Denoting the spatial coordinate by x, the potential could be defined as

$$V(x) = V_0 \cos\left(\frac{2\pi x}{a}\right) , \quad \text{with} \quad V(x+a) = V(x) , \tag{5.1}$$

with amplitude V_0 (see fig. 5.1(a) for an illustration). However, the precise form of the potential is of negligible relevance. The crucial aspect for the following discussion is the periodic nature of the potential.

For such periodic lattice potentials, there is a famous theorem, formulated by Felix Bloch in 1929, which states that the single particle wave functions are plane waves e^{ikx} multiplied by an envelope function $u_k(x)$, which has the same spatial periodicity as one of the lattice vectors, i.e. $\psi_k(x) = e^{ikx} \cdot u_k(x)$ [141]. The question to answer now is: how are the eigenstates and energies affected if the potential is switched on? This problem can be analytically treated in two limiting regimes. One where the potential is of small amplitude, comparable to the kinetic energy of the particle and the opposite, in which case the potential is much deeper than the particle's kinetic energy.

5.1.1 | Nearly Free Particle - Perturbation Theory

The case of a weakly modulated potential can be treated as a small perturbation to the otherwise free particle [142]. Starting from the unperturbed case ($V_0 = 0$), the eigenstates of the Hamiltonian are the familiar plane waves $|k\rangle$ with wave functions $\psi_k(x) = e^{ikx}/\sqrt{L}$ and because the particle is moving along a ring, the wave number k is quantised in units of $2\pi/L$. The particle only has kinetic energy which is related to k by the well known dispersion relation $E(k) = \hbar^2 k^2/2m$ with the particle mass m.

Except for zero energy, there are always pairs of degenerate eigenstates, which are $|k\rangle$ and $|-k\rangle$. It is thus necessary to assess whether non-degenerate or degenerate perturbation theory is required to obtain the correct solution. This is done by evaluating the matrix elements $\langle k| V(x) |k'\rangle$ which yield

$$\langle k| V(x) |k'\rangle = \frac{1}{L}\int_0^L e^{-ikx} V(x) e^{ik'x}\,\mathrm{d}x = \frac{V_0}{2}\delta_{k-k',2\pi/a}\,. \tag{5.2}$$

This result implies that only the states with $k - k' = 2\pi/a$ are mixed by the periodic lattice structure, which are the degenerate states with $|k| = \pi/a$ at the edge of the so-called first Brillouin zone. The underlying reason is, that waves are scattered of the lattice structure if they fulfil the condition for Bragg diffraction, i.e. that the wave number is an integer multiple of $\pm\pi/a$ [143, 144].

With this finding at hand, it is straightforward to calculate the spectrum of energies for small momenta ($|k| \ll \pi/a$) by using non-degenerate perturbation theory, which gives $E(k) = \hbar^2 k^2/2m$. This is recognized as the same quadratic dispersion as in free space, indicating that the particle moves unimpeded by the potential. This result is plausible as the de Broglie wavelength $\lambda_{\mathrm{dB}} = 2\pi/k$ of the particle is much greater than the lattice period a. In other words, the lattice potential is almost invisible for the particle. At the edge of the first Brillouin zone, degenerate perturbation theory yields the energies $E_\pm = \frac{\hbar^2}{2m}\left(\frac{\pi}{a}\right)^2 \pm \frac{V_0}{2}$. This means that a gap of size V_0 opens up in the spectrum at $k = \pm\frac{\pi}{a}$ (fig. 5.1(b)). The corresponding wave functions are superpositions of the right- and left-propagating plane waves which are Bragg-reflected to form a standing wave, i.e. $\Psi_\pm(x) \propto e^{i\pi/ax} \pm e^{-i\pi/ax}$. Here $\Psi_+(x) \sim \cos(\pi x/a)$ describes a state with the highest probability of finding the particle around the peaks of the potential while for $\Psi_-(x) \sim \sin(\pi x/a)$ the particle is mainly located around the potential minima, giving it a lower energy. In the first Brillouin zone, all states combined make up the first energy band, and the gap where no allowed states in the spectrum exist is called the first band gap. The ground state at $k = 0$ is described by the real wave function

$$\psi_0(x) = \frac{1}{\mathcal{N}}\left[\alpha + \beta\cos\left(\frac{2\pi x}{a}\right)\right] \quad \text{where} \quad \beta \ll \alpha\,, \tag{5.3}$$

with a normalization constant $\mathcal{N}$, and parameters α and β which are both functions of V_0 (fig. 5.1(c)). This wave function fulfils Bloch's theorem and is non-zero for all x, meaning the particle can be found anywhere around the ring.

5.1.2 | Tight Binding Approximation

The other limit describing a particle in a deep lattice potential is the tight binding approximation, in which the particle is primarily located at the position of the lattice sites [144]. However, with a very small probability, it can also tunnel through the potential barrier that separates neighbouring sites. The wave function $\phi(x)$, which describes a particle in an isolated lattice site, rapidly decays away from the centre of the site so that a set of basis states to work out the problem is decently approximated by the mutually orthogonal wave functions $\phi_j(x)$ for a particle localized around lattice site j. In accordance with Bloch's theorem, the wave functions can be constructed by a linear combination of the N single

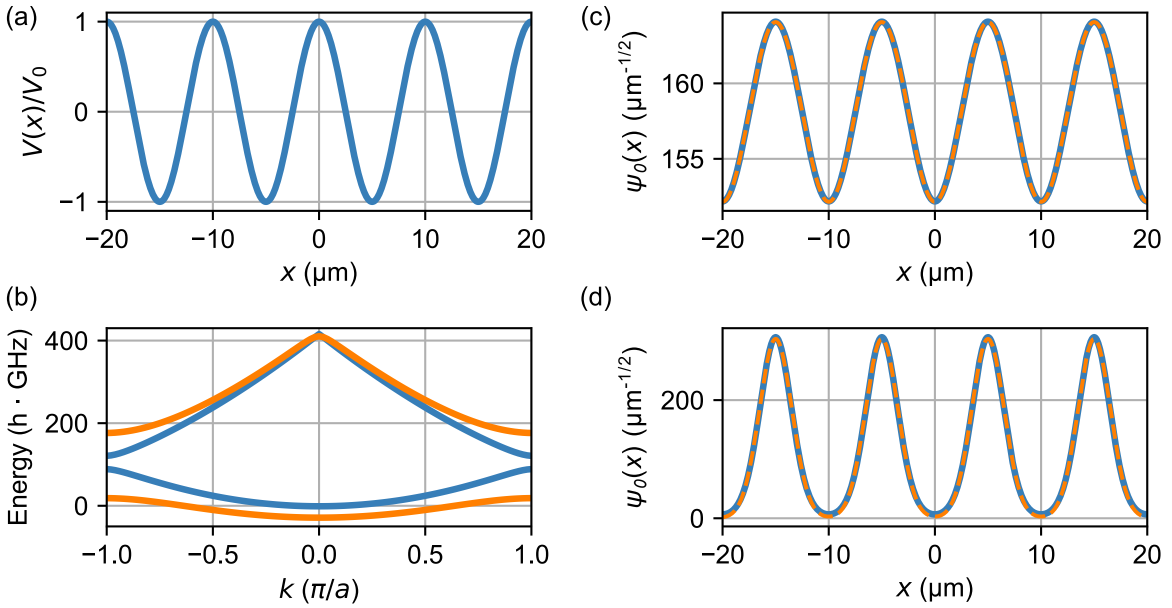

Figure 5.1: **(a)** A zoom into a peak normalized sinusoidal lattice potential with period $a = 10\,\mu\text{m}$. **(b)** Numerical calculation of the first two energy bands drawn in the reduced zone scheme for a shallow (blue) and a deep (orange) periodically closed lattice potential. The dispersion for the shallow potential is nearly unchanged for small momenta and the moderate band gap at the edge of the Brillouin zone can be calculated perturbatively. Instead, the typical cosine-like dispersion and large bandgap for the deep lattice potential is described by the tight binding model. **(c)** Ground state wave function (blue) for a photon in a cavity with parameters $q = 8$ and $\lambda_\text{c} = 580\,\text{nm}$ in a shallow potential of the form depicted in **(a)** with amplitude $V_0 = h \cdot 16\,\text{GHz}$ and a fit of eq. (5.3) (orange dashed). Note the narrow span of the vertical axis, which indicates that the wave function is only slightly modulated compared to the free particle plane wave solution. **(d)** Ground state wave function (blue) for a deep potential with amplitude $V_0 = h \cdot 1.27\,\text{THz}$ and a fit of eq. (5.4) (orange dashed) where the single site states are approximated by Gaussian wave functions. Compared to **(c)**, the wave function is mainly concentrated around the lattice sites with a small but finite amplitude between the sites.

site states, i.e.

$$\psi_k(x) = \frac{1}{\sqrt{N}} \sum_j e^{ikX_j} \phi_j(x)\,, \tag{5.4}$$

where $X_j = j \cdot a$, with $j = 0, 1, 2, \ldots N-1$, is a translation vector determined by the lattice period and the discretised wave vector can take the values $k = \frac{2\pi n}{Na}$ with $n = 0, \pm 1, \pm 2, \ldots, N/2$, i.e. it is restricted to be in the first Brillouin zone, if only one state per lattice site is considered. For systems where N is large, the states $\psi_k(x)$ form a quasi-continuous energy band which comprises N closely spaced single particle states. The dispersion relation of this energy band is then found by evaluating the energy expectation value, i.e.

$$E(k) = \langle\psi_k|\, H\, |\psi_k\rangle = \frac{1}{N} \sum_{j,m} e^{ik(X_j - X_m)} \langle\phi_m|\, H\, |\phi_j\rangle \tag{5.5}$$

$$= \sum_m e^{-ik\Theta_m} \int \mathrm{d}x\, \phi^*(x - \Theta_m) H \phi(x)\,, \tag{5.6}$$

with $\Theta_m = X_m - X_j$. Because the basis states are strongly localized, the overlap integrals between states that are separated by more than one lattice site (i.e. $|\Theta_m| > a$) can be neglected, so that the result is

$$E(k) = \epsilon - J \sum_m e^{-ik\Theta_m} = \epsilon - 2J\cos(ka) \tag{5.7}$$

$$\text{with} \quad \epsilon = \int \mathrm{d}x\, \phi^*(x) H \phi(x) \tag{5.8}$$

$$J = -\int \mathrm{d}x\, \phi^*(x-a) H \phi(x)\,. \tag{5.9}$$

Here ϵ is the energy of a particle in an isolated site, and the overlap integral between neighbouring basis states is generally difficult to evaluate explicitly, so it is often replaced by a parameter J, which represents the tunnelling energy and can be measured in an experiment. It is a negative energy because it allows for a reduction in the particle's energy by spreading over the lattice. The degeneracy of the initial eigenstates $\phi_j(x)$ is lifted by the tunnelling, and a narrow energy band with bandwidth $4J$ is formed. Depending on how many bound states there are per lattice site, there can also be more than just one energy band, each of which then spans over N different k-states (see fig. 5.1(b) which shows the first two energy bands). Considering only the lowest energy band for now, one can see by Taylor-expanding the dispersion relation for small k, that

$$E(k) \approx \epsilon - 2J + Jk^2a^2 =: \epsilon - 2J + \frac{\hbar^2 k^2}{2m^*}\,, \tag{5.10}$$

where an effective mass $m^* = \hbar^2/2Ja^2$ was defined. In physical terms this means, that a particle at low energy moves like in free space with mass m^*, unaware of the underlying lattice potential. The effective mass is not related to the physical particle however (or the effective mass of a photon), but it is determined by the lattice properties.

Equations (5.8) and (5.9) are the diagonal and off-diagonal matrix elements of the Hamiltonian evaluated in the basis of the single site wave functions. It is thus straightforward for a system with a finite number of lattice sites to cast the equations into an eigenvalue problem. Diagonalization of the Hamiltonian then yields the eigenenergies (5.7) and the tunnelling between sites leads to hybridization of the basis states, which results in lattice eigenfunctions that are linear superpositions of the localized basis states. In particular, the ground state for $k = 0$ is the symmetric superposition of all localized basis states, i.e.

$$\psi_0(x) = \frac{1}{\sqrt{N}} \sum_j \phi_j(x)\,, \tag{5.11}$$

which, similarly to the nearly free particle, describes a state with finite probability density everywhere around the ring, albeit having a very small density between sites (fig. 5.1(d)). The situation discussed here can also be considered as the Bose-Hubbard model for non-interacting bosons [145]. The roots of this model are found in the principle of adding isolated single particle states for the calculation of molecular wave functions, which is frequently encountered in molecular and chemical physics, where the method is called *linear combination of atomic orbitals* (LCAO) [146].

5.2 | A Four-Site Unit Cell for Experiments with Photons

Despite the very different assumptions made in the models of nearly free and tightly bound particles in the previous sections, the two approaches describe quite similar physics. They both give rise to a free space-like dispersion at small energies and explain how the different single particle states are arranged into energy bands, although these bands are of very different bandwidth. The existence of band gaps are common to both models, however only the perturbative approach correctly models how they arise from a continuum of momentum states. The wave functions share the same periodicity according to Bloch's theorem, and they are spread out over the entire lattice in both models. The main difference lies in the fact that the tight binding solutions are mainly concentrated at the lattice sites, whereas the nearly free particle approximation yields solutions with a much weaker density modulation. For a real case problem (that is somewhere in between the two limiting cases), it is therefore valid to choose either of the two pictures as a first step, in order to gain some intuition on the problem.

The potential geometry studied in this thesis consists of four lattice sites, that are arranged on the edges of a square with side length a, i.e. they form a periodically closed ring structure. Modelling the ring in tight binding approximation and assuming that there is just one bound state per site and each site is coupled only to its direct neighbours by the tunnelling amplitude J, the Hamiltonian expressed in the localized basis states $\phi_j(x, y) = \phi(x - x_j, y - y_j)$, with $j = 1, 2, 3, 4$, reads

$$\hat{H}_{\mathrm{lat}} \simeq \begin{pmatrix} \epsilon & -J & 0 & -J \\ -J & \epsilon & -J & 0 \\ 0 & -J & \epsilon & -J \\ -J & 0 & -J & \epsilon \end{pmatrix}, \tag{5.12}$$

where ϵ and J are given by equations (5.8) and (5.9). Diagonalization of the Hamiltonian yields for the eigenstates

$$\psi_n(x, y) = \frac{1}{\sqrt{4}} \left[\phi_1 + e^{in\frac{\pi}{2}} \phi_2 + e^{i2n\frac{\pi}{2}} \phi_3 + e^{i3n\frac{\pi}{2}} \phi_4 \right], \tag{5.13}$$

which can be labelled by the integer $n = 0, \pm 1, 2$ corresponding to the solution with $k = \pi n/2a$. The corresponding energies of the states are given by $E_0 = \epsilon - 2J$, $E_{\pm 1} = 0$ and $E_2 = \epsilon + 2J$, i.e. the ground state and the second excited state of the system should be equally separated in energy from a pair of two degenerate intermediate states.

5.2.1 | Design Parameters of the Four-Site Mirror Surface Profile

In the discussion of the optical grating spectrometer in sec. 3.3.2, it was pointed out that achieving a high spectral resolution for spatially extended light sources can be a difficult task. On the other hand, the spatial resolution of the imaging setup also imposes a limit on how well the density distribution of cavity modes in very closely spaced lattice sites can be resolved. Ideally the experiment would benefit from both a high spectral and spatial resolution, in practice, however, one has to find a compromise. This is because, to stay with the picture of the tight-binding approximation, the energetic splitting between states is proportional to the overlap of the neighbouring on-site wave functions. The important parameters for controlling this coupling energy experimentally are therefore the width and height of the potential barriers separating the sites. For high coupling energies at distant spacings between sites, relatively shallow barriers are required.

In the course of choosing suitable parameters for the potential, the distance between sites was decided to be near 10 µm. The eigenenergies and density distributions of the lowest energy states were then numerically calculated for a target profile using the finite difference method described in sec. 2.5.3. The potential barriers between the sites were adjusted in amplitude, until the calculated energetic spacings were close to $\Delta E \sim h \cdot 50\,\mathrm{GHz}$, which should allow to spectrally resolve them, given the experimental resolution of $\Delta\nu \approx 20\,\mathrm{GHz}$. In order to allow for a Bose-Einstein condensate of photons in the ground state, a manifold of excited states with a density of states $g(E) \propto E^{\alpha-1}$ with $\alpha > 1$ is required (see sec. 2.1.2), such that a saturation of the thermal cloud can be achieved at high photon densities. These states can be provided by superimposing a harmonic trapping potential ($\alpha = 2$) around the four-site structure.

5.3 | Creation and Numerical Characterization of the Surface Structure

The above outlined target trapping potential is realized with the mirror surface structuring setup presented in sec. 2.5.2. In order to achieve the requisite precision, an iterative process is implemented, comprising here 20 iterations. An image of the final surface profile, recorded with a white light interferometer is shown in fig. 5.2(a). The structured surface can be well approximated by four Gaussian-shaped indents arranged at the edges of a square, radially surrounded by a harmonically increasing elevation. For the quantitative analysis of the trapping potential, a two-dimensional function modelling this description is fitted to the surface profile, so that experimental parameters like the width of the sites or the harmonic trapping frequency can be estimated. The mean depth of the sites obtained from the fit is $0.80(6)$ nm, the FWHM is $6.7(3)$ µm and the lateral separation is $10.0(4)$ µm. The structure size radially extends up to 60 µm from the trap centre and levels off at a maximum surface height of $\approx$ 15 nm. While the lateral extent of the potential is limited by the field of view of the structuring setup, a maximum elevation below $\approx$ 20 nm guarantees that the microcavity can be maintained at high finesse [35]. The radius of curvature of the surface structure is $14.8(7)$ cm which corresponds to a harmonic trapping frequency of $64(2)$ GHz at the longitudinal mode number of $q = 9$. In theory, the trapping potential should confine modes up to an energy of $E_{\mathrm{max}} = h \cdot 3.9\,\mathrm{THz}$, which amounts to a total of 60 trapped harmonic oscillator levels or, counting all degenerate states in the two-dimensional system, $\sum_{m=0}^{60}(m+1) = 1\,770$ trapped individual states per polarization component.

In order to examine how the structured surface would translate into a trapping potential for photons, the fitted profile is used to calculate the expected eigenmodes and eigenenergies numerically. The main advantage of using the fitted profile instead of the directly measured profile is that the computation time can be reduced considerably. This is because the point density at which the potential is sampled, can then be adjusted to $\sim 1/\mu\mathrm{m}^2$, resulting in a $\sim$ 25-fold reduction in matrix size needed for the finite difference method, in comparison to the raw profile, which is recorded at a point density of $\sim 1/(0.2\,\mu\mathrm{m})^2$. The numerical analysis was conducted for various point densities to ensure the reliability of the numerical results.

Fig. 5.2(b) shows the calculated density distributions of the four lowest energy eigenmodes at the longitudinal mode number $q = 9$ and $\lambda_c = 584\,\mathrm{nm}$. The modes are labelled by an index $0, \pm 1, 2$, consistent with the notation used earlier (see sec. 5.2). They qualitatively resemble the expected mode distributions in the closed ring configuration with four lattice sites according to eq. (5.13), however slight imbalances between the densities per site can be observed, which are due to the remaining non-uniform depths and widths of the separate sites. Fig. 5.2(c) shows horizontal cuts through the centre of the trapping potential, at $y = 0\,\mu\mathrm{m}$ (dashed black line), and along an axis connecting two sites, at $y = 5\,\mu\mathrm{m}$ (solid black line). The potential energy curves are obtained from the averaged site fit parameters. Also shown are the calculated eigenenergies at $E_0 = h \cdot 140.1\,\mathrm{GHz}$, $E_{+1} = h \cdot 191.7\,\mathrm{GHz}$, $E_{-1} = h \cdot 200.5\,\mathrm{GHz}$ and $E_2 = h \cdot 251.4\,\mathrm{GHz}$. The degeneracy between the states ψ_{+1} and ψ_{-1} is lifted

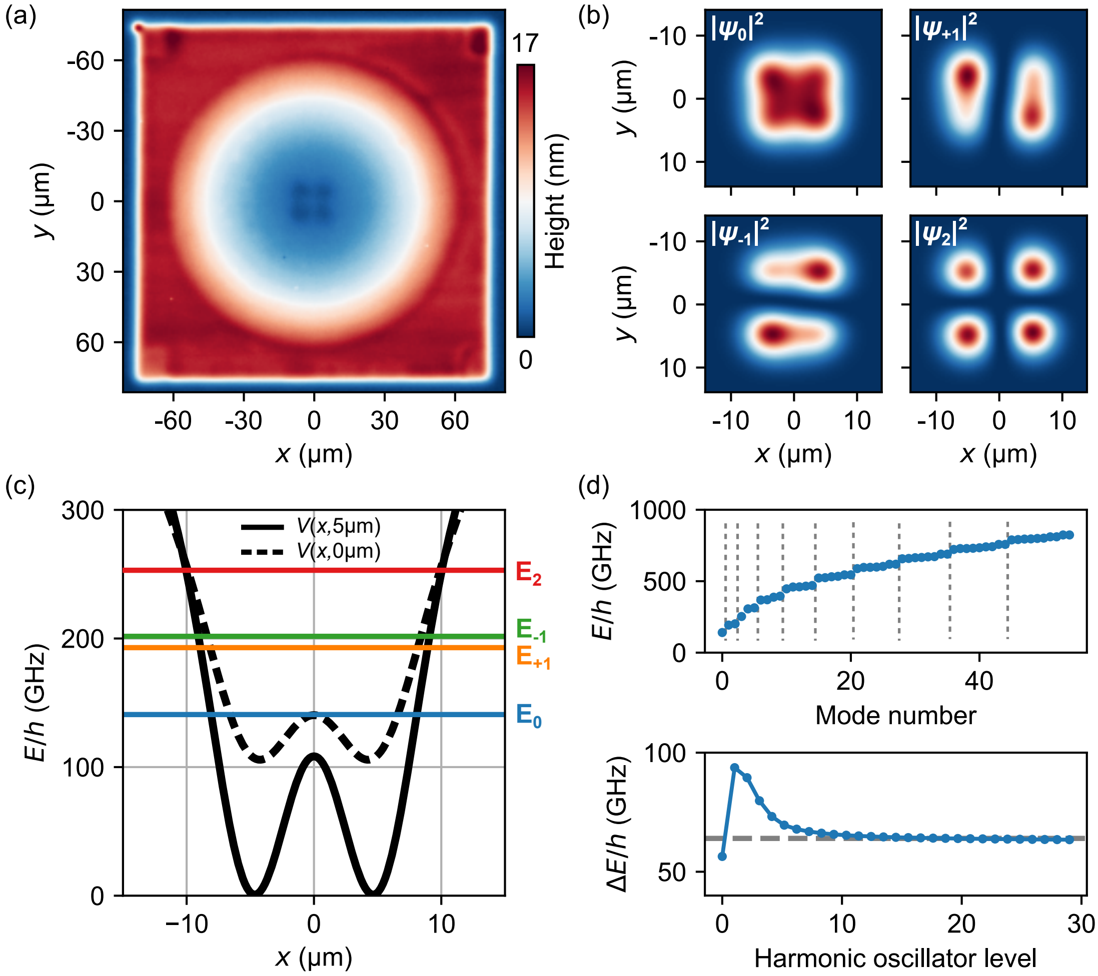

Figure 5.2: **(a)** Surface profile of the microstructured cavity mirror. Four Gaussian-shaped indents in the cavity centre are surrounded by harmonically increasing walls in the radial direction. **(b)** Numerically calculated (peak normalized) density distributions of the four lowest energy eigenmodes in the resulting trapping potential at $q = 9$ and $\lambda_c = 584\,\text{nm}$. The modes are labelled by the respective indices $0, \pm 1, 2$, consistent with the notation used in the tight-binding approximation, even though this description fails to be very accurate for the used parameters (cf. text). **(c)** Cuts through the potential landscape obtained from averaged fit parameters of the profile shown in **(a)** (black lines) and calculated energies of the states ψ_0, $\psi_{\pm 1}$, and ψ_2. The mode energies are comparable to the energies of the barriers, which necessitates a numerical calculation of the eigenstates, as analytical approximations are not applicable in this case. **(d)** The top panel gives the energies of the first 55 eigenstates in 2D. The vertical dashed lines indicate which modes should be grouped together if they were equivalent to harmonic oscillator states. The bottom panel gives the difference between the mean energies of these groups of modes and the dashed horizontal line indicates the expected trapping frequency of 64 GHz, which is calculated from the fitted radius of curvature of the surface profile.

because of the already mentioned small potential inhomogeneities between the separate sites. Denoting the mean energy of the two intermediate levels by $\overline{E_{\pm 1}} = h \cdot 196.1\,\text{GHz}$, an average energetic splitting between the states can be calculated, i.e. $\overline{E_{\pm 1}} - E_0 = h \cdot 56\,\text{GHz}$ and $E_2 - \overline{E_{\pm 1}} = h \cdot 55.3\,\text{GHz}$. These energy differences can be considered as equidistant and they are found to be close to the designated spacings of $\Delta E = h \cdot 50\,\text{GHz}$. In the tight-binding approximation, this would correspond to couplings of $J = \Delta E/2 \approx h \cdot 28\,\text{GHz}$. When the calculated eigenenergies are compared to the potential barriers, it is evident however, that all modes are situated above the barriers separating neighbouring sites and only the ground mode energy is slightly below the potential hill in the trap centre. This implies that the system should not be properly modelled in tight-binding approximation, which only applies if all states are of smaller energy than the potential barriers (cf. sec. 5.1.2). An alternative description for the eigenstates may be obtained by considering the potential as a box with inclined walls, where the barrier structure constitutes a perturbation in the bottom of the box. This point of view would suggest, that the observed states at low energies are similar to box-modes, albeit with distinctly modified density distributions, affected by the four-site structure in the bottom of the potential. Nevertheless that this description could be qualitatively matching for the low energy modes, it is far from being accurate, because a barrier of $\sim h \cdot 100\,\mathrm{GHz}$ can not be considered as a small correction for a box potential with a total depth of $h \cdot 300\,\mathrm{GHz}$. The states are therefore found to be in a crossover region where neither of the analytical approaches (tight-binding and perturbation theory) provide a valid model. This also emphasizes the importance of numerically solving the Schrödinger equation, without which this insight would be difficult to obtain.

Fig. 5.2(d) in the top panel gives the calculated eigenenergies for the 55 lowest energy modes. The visible step-like pattern for modes at energies larger than $\sim h \cdot 500\,\mathrm{GHz}$ alongside the linearly increasing number of modes per step, reveals that the potential can indeed be modelled as a harmonic oscillator at these energies. This is also clear from the bottom panel of fig. 5.2(d), which shows the difference between the mean energies per harmonic oscillator level, for which modes between two dashed vertical lines in the top panel are grouped into one level. Above the 10th oscillator level, the energetic spacing becomes nearly equidistant and it agrees well with the previously calculated trapping frequency of $\Omega = 64\,\mathrm{GHz}$, the result from the fitted radius of curvature. The potential should therefore be well suited to support photon BEC in the ground state of the four-site structure.

5.4 | Experimental Characterization of the Trapping Potential

Before conducting an experiment on photon BEC in the prepared micropotential, it is first investigated whether the physical parameters obtained from the numerical analysis are consistent with the experimental conditions. Particular attention is given to the low-energy modes, where the density of states is expected to differ from that of a harmonic oscillator.

Nearly all of the previously discussed parameters can be conveniently extracted by measurements of the photon spatial and spectral density distribution under steady state operating conditions. The cavity is assembled with a plane mirror and the microstructured mirror according to the setup shown in fig. 3.1(a). While the interference fringes in the transmitted pattern of the Helium-Neon laser serve well for a coarse parallel alignment of the two mirrors, the achievable precision is insufficient to entirely get rid of remaining small gradients of the trapping potential. The needed accuracy for the mirror alignment can instead be achieved by monitoring the spatial and spectral distribution during the process of iteratively optimizing the relative mirror orientation, until the emitted light from the cavity is very close to being evenly distributed over all four sites and the two intermediate states $\psi_{\pm 1}$ are nearly degenerate in energy. This implies that an underlying gradient in potential energy is minimized.

5.4.1 | Spatial Density Distributions of the Low Energy Modes

A detailed picture of the spatial mode distributions in the four-site potential can be obtained by using a tightly focused pump beam (FWHM of $\approx 5\,\mu\mathrm{m}$) at high pump powers under highly nonequilibrium conditions. By transversely moving the beam over the four-site structure, it is possible to almost exclusively populate a single resonator mode. This is because excitations are then only induced in

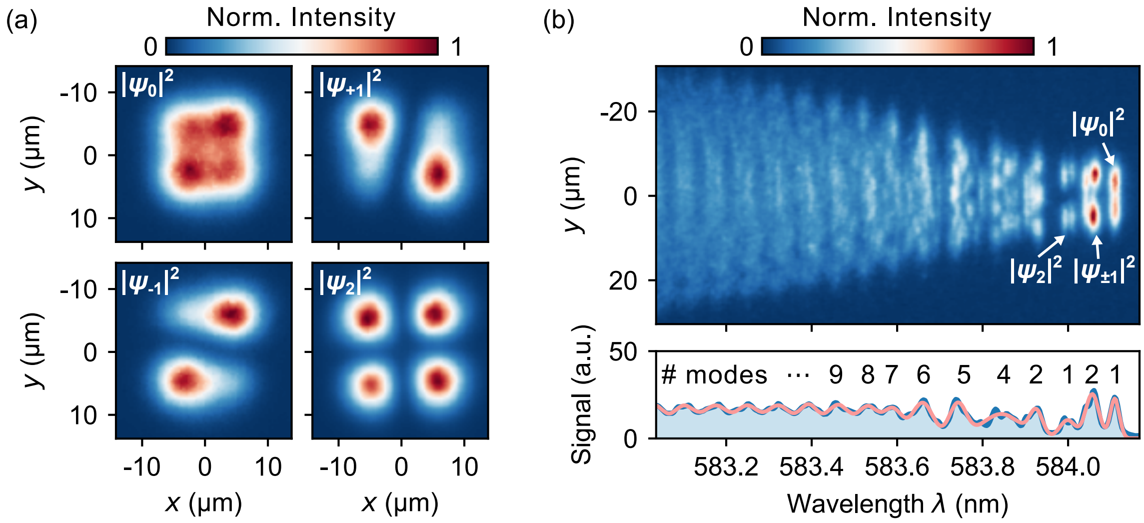

Figure 5.3: **(a)** Peak-normalized density distributions of the four lowest energy states, recorded at $\lambda_c = 584.1$ nm and $q = 9$. The images are obtained by using a strongly focused, high power pump beam so that only a single resonator mode is populated under conditions far away from thermal equilibrium. **(b)** The top panel gives the peak-normalized spectral density distribution recorded via the high dispersion spectrometer for a pump size of ≈ 55 µm FWHM and a total photon number below the condensation threshold. The three rightmost peaks correspond to the states ψ_0, $\psi_{\pm 1}$, ψ_2 and the crossover to a harmonic density of states at higher energies is visible from the square-root like increase in mode size along the vertical direction with increasing energy. The bottom panel gives the vertically integrated spectral density distribution. A multitude of peaks can be identified and merged into groups of energy states with the help of the data shown in fig. 5.2(d). The number of modes per group and per polarization component are given by the labels. The resonance frequencies of these groups of modes can be extracted by approximating the signal as a superposition of many neighbouring Gaussian peaks.

the cavity over a small spatial region and therefore the mode that exhibits the largest overlap with the molecular excitation profile (and consequently experiences the largest gain) will be amplified by stimulated emission of photons. The recorded profiles of the four lowest energy modes are shown in fig. 5.3(a). They qualitatively agree very well with the numerically calculated density distributions shown in fig. 5.2(b), but there are also visible differences. Focusing on the ground mode ψ_0 first, it is evident, that the photon density is larger in the sites and smaller over the barriers, compared to the numerical solution. The same feature is also observed for the two near degenerate states $\psi_{\pm 1}$, which both show a bigger absolute difference between the maximum and minimum density per site than is predicted by the numerical calculation, meaning that photons in these modes are predominantly localized in just two sites on the diagonals of the four-site structure. Among the four measured mode distributions, the state ψ_2 shows the closest agreement with the numerical calculation, which is perhaps due to it having the highest energy of the four states, so it is least affected by the detailed structure of the trapping potential. Overall it is clear that all modes are non-uniformly distributed over the four sites. The reason for this are the already mentioned remaining variations in the site to site structured surface profile, which can not be compensated in the present setup. In future, the additional use of a thermo-optic potential tuning technique [38, 114] could resolve this issue for future experiments if the sites need to be tuned more exactly into resonance w.r.t. each other.

5.4.2 | Spectral Density Distributions of the Low Energy Modes

The observed mode shapes suggest that photons in the cavity are overall more deeply bound to the structured sites than it was concluded from the numerical analysis. This also implies that the coupling energy between sites would be smaller and thus the modes should be more closely spaced in energy than what was calculated. This can be investigated by recording the spectral distribution of photons using the high resolution spectrometer path via the Echelle grating. The pump beam then has to be increased to a diameter which is large compared to the investigated structure size, so that all cavity modes exhibit similar overlaps with the excitation profile. The top panel of Fig. 5.3(b) shows the recorded spectrum for a pump size of $\approx 55\,\mu\text{m}$ FWHM and a pump power below the condensation threshold. The modes ψ_0, $\psi_{\pm 1}$ and ψ_2 are identified at the low energy end of the spectrum. The x-axis here is only labelled by the calibrated wavelength of the spectrometer, however the full spatial information is also preserved along this axis, as was pointed out in sec. 3.3.2. The aspect ratio of the imaged mode profiles is $\approx 6{:}1$ (vertical/horizontal) for this measurement, which is on one hand due to the anamorphic grating magnification and on the other hand, which is the more dominant contribution, due to the use of two perpendicularly oriented cylindrical objective lenses with focal lengths $f_x = 30\,\text{cm}$ and $f_y = 5\,\text{cm}$ placed after the grating. This allows to record a much broader part of the optical spectrum on the camera sensor, while a decent spatial resolution in the vertical direction can be maintained simultaneously. As is evident, the spectral resolution is sufficient to clearly resolve the small sized low energy modes. The square root scaling of the mode size with increasing energy for the harmonic oscillator modes is visible in the vertical direction. This implies that the modes increasingly overlap for higher energies along the horizontal axis, to a point where they can not be spectrally distinguished any more, which is also visible in the bottom panel of fig. 5.3(b), showing the vertically integrated spectrum. Despite not being resolvable from the bunch, the integrated spectrum clearly allows to identify separate peaks which can be matched to the different energy levels, as was discussed in sec. 3.3.2. The integers on top of the separate peaks give the number of modes per trap level and per polarization state, which were experimentally verified for the first few energy levels by selectively exciting and counting the different modes using the focused pump beam.

A quantitative analysis of the energy level structure can now be performed by fitting a sequence of neighbouring Gaussian peaks to match the measured distribution. Such a fit is shown by the orange line in the bottom panel of fig. 5.3(b). Clearly, the fit function can not accurately model the actual spectrum, however it allows to extract the resonance frequencies of the individual trap levels. According to the fit parameters, the four lowest energy modes are separated by $\overline{E_{\pm 1}} - E_0 = h \cdot 47.3(8)\,\text{GHz}$ and $E_2 - \overline{E_{\pm 1}} = h \cdot 50.5(3)\,\text{GHz}$, where the two near degenerate levels were combined to a mean energy $\overline{E_{\pm 1}}$. These energy differences are almost equal and close to the designated splittings of $\Delta E = h \cdot 50\,\text{GHz}$. However, the coupling energies are indeed smaller than expected from the numerical analysis, which supports the conclusion drawn from the spatial mode profiles. Also the measured trapping frequency of $\Omega = 2\pi \cdot 62(3)\,\text{GHz}$, which is obtained by averaging the energetic differences between neighbouring states higher than the 10th oscillator level, is slightly smaller than the numerically calculated frequency. Although the error bars of this result include the numerical value, it is noticeable, that all experimentally determined (relative) energies seem to be smaller than their respective numerically calculated value. This is an observation, which was also pointed out for a similar, recently performed experiment [37]. As will be discussed in the next section, these observations can be explained, at least qualitatively, by considering that the photon field has a non-zero amplitude in the mirror coatings.

5.4.3 | Penetration Depth of Light into the Mirror Coatings

The discrepancies in the mode profiles and energies between the numerical calculation and the experimental results could be rooted in a photon field which is not completely confined between the two highly reflecting mirrors, but instead leaks into the dielectric coatings. The length scale, over which the field penetrates into the mirrors, was experimentally determined to be $L_{\mathrm{DBR}} = q_0 \frac{\lambda_{\mathrm{c}}}{2\tilde{n}} \approx 949(34)\,\mathrm{nm}$ at the resonance wavelength of $\lambda_{\mathrm{c}} = 584\,\mathrm{nm}$, where $q_0 = 4.68(17)$ gives the number of half-waves located in the mirrors [12]. This result can also be confirmed by the relation $L_{\mathrm{DBR}} = \frac{\lambda_{\mathrm{c}}}{2\tilde{n}} \frac{n_1 n_2}{|n_1 - n_2|} \approx 936\,\mathrm{nm}$ [79, 147], where $n_1 = 1.4587$ (SiO_2) and $n_2 = 2.1326$ (Ta_2O_5) are the refractive indices of the Bragg layers in the mirror coating [148, 149]. This implies an effectively higher refractive index for light inside the microcavity, compared to that of ethylene glycol ($\tilde{n} = 1.4392$). Modelling this effect exactly is a difficult task, however a decently accurate picture can be obtained by inspecting how the photon energy in eq. (2.25) changes with the generalized refractive index $\tilde{n}$.

Upon substitution of the cavity length $L_0 = q\lambda_{\mathrm{c}}/2\tilde{n}$ and the effective photon mass $m_{\mathrm{ph}} = \tilde{n}q\pi\hbar/cL_0 = 2\tilde{n}^2\pi\hbar/c\lambda_{\mathrm{c}}$, the potential energy is

$$V(x) = \frac{4\pi c\pi\hbar}{q\lambda_{\mathrm{c}}} \cdot \Delta L(x) \cdot \tilde{n}\,. \tag{5.14}$$

This is a linear scaling with $\tilde{n}$, making the potential effectively deeper when $\tilde{n}$ is increased. The kinetic energy on the other hand decreases as

$$E_{\mathrm{kin}} \propto \frac{1}{m_{\mathrm{ph}}} \propto \frac{1}{\tilde{n}^2}\,. \tag{5.15}$$

This means that for larger $\tilde{n}$ the mobility of photons in the potential is lowered due to their reduced kinetic energy and the increased potential energy. Photons should therefore be more localized around the potential pits, which is indeed verified from the typical extend of the wave functions. Recalling for example that the harmonic oscillator wave functions scale as $\psi(x) \propto \exp -\frac{1}{2}\frac{x^2}{x_0^2}$, with the harmonic oscillator length $x_0 \propto 1/\sqrt{m_{\mathrm{ph}}\Omega} \propto \tilde{n}^{-\frac{3}{4}}$, where $\Omega \propto 1/\sqrt{\tilde{n}}$ was used, demonstrates that photons become more confined for an increasing refractive index. As a consequence, the coupling energy between sites for photons in a lattice potential would also decrease, so that the energetic splitting between the eigenstates becomes smaller. This explanation agrees well with the experimental observations, so that it seems possible that the ground state is energetically situated below the actual potential barriers in the experiment.

5.5 | Numerical Fit Functions for the Photon Density Distributions

For a quantitative comparison between the measured density profiles and Bose-Einstein distributions in the prepared micropotential, theoretical fit functions are constructed following the procedure described in secs. 3.3.1 and 3.3.3. For this purpose, the measured spatial density profiles of the first four modes, shown in fig. 5.3(a), are used to calculate the one-dimensional mode profiles $|\psi_m(x)|^2$, with $m = 0, \pm 1, 2$. All other modes are approximated by harmonic oscillator states, according to the degeneracy given in fig. 5.3(b), for a trapping frequency of 63 GHz. The energies of the modes over the first ~ 500 GHz of spectral bandwidth in the potential are derived from the spectrum displayed in fig. 5.3(b). In contrast to the numerically calculated trap depth of $E_{\mathrm{max}} = h \cdot 3.9\,\mathrm{THz}$, it turned out during the analysis that the measured distributions are energetically broader than what would be covered by this bandwidth, and that they are better matched by distributions that reach up to the energy

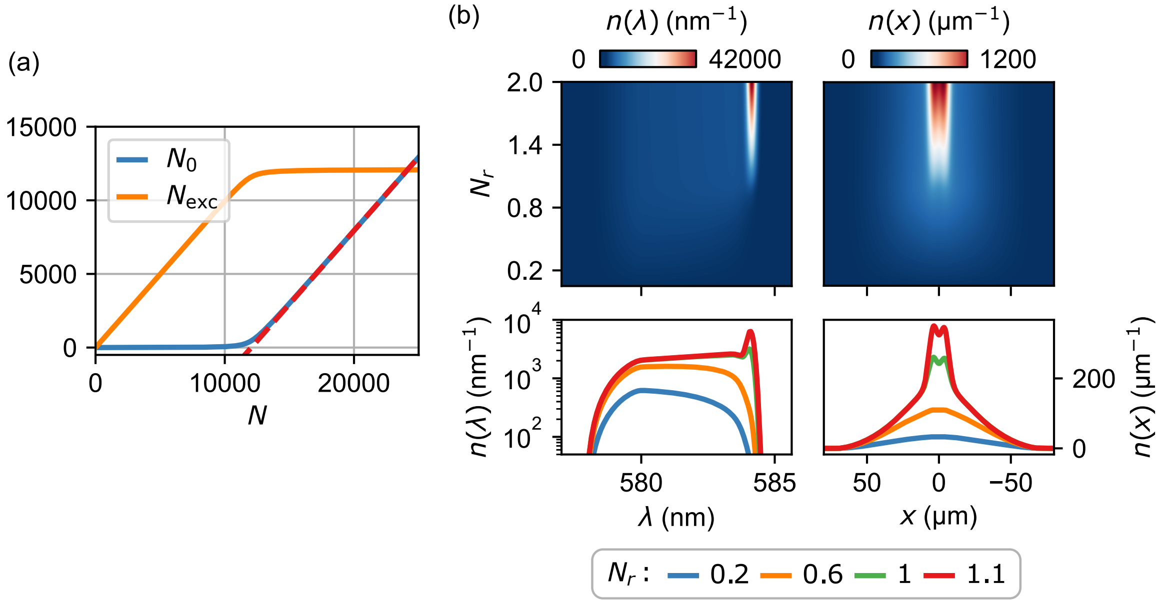

Figure 5.4: **(a)** Calculation of the Bose-Einstein distributed populations of photons in the ground mode (blue) and in the excited modes (orange) for the trapping potential with the four-site structure. The red dashed line is a linear fit of the ground mode population above the condensation threshold and the intersection with the N-axis marks the critical photon number. The transition point to the condensed regime is softened due to the finite mode number in the system, but the saturation of the excited states for $N > N_c$ displays the distinct feature of Bose-Einstein condensation. **(b)** The top panels show a two-dimensional map of theoretical Bose-Einstein distributed spectral and spatial densities vs. the relative photon number N_r. The bottom panels show the distributions for four selected relative photon numbers.

of $E_{\max} \sim h \cdot 4.5\,\mathrm{THz}$. The reason for this deviation is not entirely clear, but it could be, that cavity modes situated on top of the potential are also affected by the mirror structure and thus form additional confined modes, which then also contribute to the full spectrum of modes. A small contribution to an effectively deeper potential could also be due to the non-zero probability of photons being inside the mirror coatings, as mentioned in the previous section. The theoretical distributions are therefore extended and modelled using an effectively deeper potential up to the energy of $E_{\max} \sim h \cdot 4.5\,\mathrm{THz}$, where all additional modes are also approximated by harmonic oscillator states.

For the Bose-Einstein distribution, the photon number per mode n_m is determined by the chemical potential μ or, equivalently, the total photon number N in the system. Since the latter is in principle directly accessible from an experiment, it is used as the free parameter of the fit function. Accounting for the two orthogonal polarization components, the population in the ground mode and the excited modes is calculated versus the total photon number, reaching from far below to well above the condensation threshold, see fig. 5.4(a). The critical photon number at the condensation threshold can be obtained from the intersection with the N-axis by linearly extrapolating the ground mode population from above threshold down to zero, which yields $N_{\mathrm{c,theo}} = 12\,050$. Using the critical photon number, one can define a relative photon number in the system, $N_r := N/N_c$, analogous to the definition of a reduced temperature, $T_r = T/T_c$, for cold atoms. The relative photon number will be used as the primary fit parameter along with a scale factor, $\mathcal{A}$, to account for possible deviations in the absolute photon numbers (cf. sec 2.4.8).

One aspect to keep in mind is, that the interesting photon distribution is the one inside the cavity, which is not directly proportional to the distribution measured outside of it, due to the wavelength dependent mirror transmission (cf. eq. (3.14)). For the spectral densities, this implies that the measured signal should be divided by $T_s(\lambda)$ before comparing it to a Bose-Einstein distribution. The same approach however is rather difficult to apply to the spatial distributions, since all modes are overlapped and the individual contributions can not be distinguished appropriately in the experiment. For this reason, in the calculation of the theoretical spatial fit function, the modes are multiplied by the corresponding mirror transmission $T_s(\lambda)$, so that the corrected fit function can be directly matched to the recorded distributions.

Fig. 5.4(b) shows a two-dimensional map of the constructed fit functions for the spectral, $n(\lambda)$, and spatial, $n(x)$, density distributions, evaluated for relative photon numbers in the range of $N_r = 0.05-2.0$. Also shown are the distributions for four selected relative photon numbers. Note that fig. 5.4(b) contains the same information as fig. 5.4(a) in terms of the photon numbers, as the individual state populations here are incorporated in the density profiles.

Chapter 6 | Photon Condensation in a Four-Site Lattice Unit Cell

This chapter presents experimental results on photon Bose-Einstein condensation in the microstructured potential with four lattice sites. Spatial and spectral distributions for different total photon numbers are measured and compared to the previously calculated theoretical Bose-Einstein distributions in sec. 5.5. The individual occupation numbers per state as a function of the total photon number are extracted and the phase coherence between lattice sites is examined.

6.1 | Experimental Parameters

A microcavity consisting of the microstructured mirror analysed in the previous chapter, and a plane mirror, both with the coating *LO2018* (see fig. 2.2(a)), is assembled and filled with a Rhodamine 6G dye solution at a concentration of $\rho = 1\,\text{mmol/l}$. As for the characterisation of the trapping potential in the previous chapter, the cavity is set up at the longitudinal mode number $q = 9$ and the cutoff is fixed to the wavelength of $\lambda_c = 584.1\,\text{nm}$. The photon absorption and emission rates at the cutoff wavelength are $\Gamma_{12} = 4.2\,\text{GHz}$, and $\Gamma_{21} = 1\,434.5\,\text{GHz}$. In a previous experiment [85], conducted with the same mirrors used in this work, the cavity loss rate was found to be 4 times larger than what would be obtained when using the raw mirror transmission profile, provided by the manufacturer, in eq. (2.52). The same correction factor is used here to estimate the cavity loss rate, which gives $\kappa = 4.1\,\text{GHz}$. The cutoff at 584.1 nm was chosen because of the relatively small pump threshold at this wavelength. This comes at the trade-off of conducting the experiments in a regime of moderate photon thermalisation however, as is evident from the corresponding thermalisation parameter of $\gamma = \kappa/\Gamma_{12} \approx 1$. The pump size therefore needs to be tuned accordingly, so that an approximately uniform chemical potential can be realized (see the discussion in sec. 2.4.8). By adjusting the pump shape while monitoring the photon distribution around the threshold to Bose-Einstein condensation, it was found that the best match with the previously calculated equilibrium Bose-Einstein distribution (cf. sec. 5.5) is realized for a pump size of 55 µm FWHM (throughout the chapter, the notation of FWHM will often be omitted).

The pump pulse length is set to 500 ns, over which steady state conditions in the cavity are realized, and the experiment is repeated at a rate of 50 Hz. In order to map out the photon distribution in the microcavity from far below to above the condensation threshold, the pump power is increased in steps, and the time-integrated spatial and spectral density distributions are recorded on the ICCD camera. The experimental photon number is obtained from the integrated spatial density distributions and a calibration of the camera signal, which is performed beforehand using a Helium-Neon laser at 593.9 nm wavelength, according to the description in sec. 3.4.

6.2 | Spatial Photon Distributions

The measurement of the spatial density distribution is achieved by imaging a part of the cavity emission onto the ICCD camera, and the experiment is repeated 200 times for every pump power. Fig. 6.1 shows obtained distributions recorded at six different pump powers, which correspond to the relative photon numbers of $0.11 \leq N_r \leq 1.24$. The top row shows the plain distribution, $n(x, y)$, and the bottom row gives the one-dimensional spatial density, $n(x)$, which is obtained by integration of the signal along the y-axis. The shaded areas are standard deviations. These are relatively larger over the size of the ground mode in the condensed regime compared to below the condensation threshold, because in this regime, the ground mode population is very sensitive to small variations in pump power or cavity cutoff due to stimulated photon emission.

Inspecting the plain density profiles it is evident, that upon increasing the photon number in the cavity, the distribution changes from a broad photon cloud into a more centrally peaked distribution, where the characteristics of the low energy modes, affected by the four-site potential structure, become apparent. At a certain photon density, the ground mode begins to show on top of the distribution until it clearly stands out when a critical photon density is exceeded. However, when compared to the measured profile of the ground mode in fig. 5.3(a), it is noticeable that the condensate density distribution observed here exhibits a slight tendency towards the lower two sites. A possible reason for this could be, that there was a slightly different gradient of the potential structure present when the two measurements were performed, which slightly displaced the photon density towards the bottom of the trapping potential. However, as will be clear from the discussion of the population per state in sec. 6.5, the major cause for this effect is that a small contribution of the first excited state adds to the ground state above the condensation threshold.

The measured photon numbers for the shown profiles are $N = 316(55)$ for $N_r \approx 0.11$ up to $N = 3\,636(641)$ for the measurement at $N_r \approx 1.24$. As these numbers are significantly smaller than the previously calculated critical photon number $N_{\mathrm{c,theo}} = 12\,050$, the scale factor, $\mathcal{A}$, relating the ratio of the measured to the theoretical photon number in the cavity as introduced in sec. 2.4.8, is included for numerical fitting of the Bose-Einstein distributions to the measured distributions. The numerical value of $\mathcal{A}$ is determined by running the fitting routine at first with a freely adjustable scale factor for all measured distributions. This gives a very good agreement between the measurements and correspondingly scaled Bose-Einstein distributions in general. The fit parameters obtained by this analysis are shown in fig. 6.2(a) and the measured photon number is plotted against the fitted relative photon number in fig. 6.2(b) (blue dots). Allowing for a different scale factor for every distribution, evidently results in a smaller $\mathcal{A}$ for decreasing photon numbers, while the fitted relative photon number remains at higher values ($N_{r,\mathrm{fit}} \sim 0.4$), when the measured photon number approaches zero. This is of course unphysical and hints at photon distributions, which are too pronounced for the low energy modes in the regime of small photon numbers, a consequence of the relatively small utilized pump size. In order to resolve the issue of the measured photon number being not in compliance with the fitted relative photon number, the scale factor is fixed to the value obtained for the measurement close to threshold, i.e. for $N_{r,\mathrm{fit}} \approx 1$, which gives $\mathcal{A} = 0.24$, and the fitting routine is performed again. With the fixed fitting parameter $\mathcal{A}$, the measured and the fitted relative photon numbers exhibit perfect linear scaling and a zero crossing at $N = 0$, see fig. 6.2(b) (orange dots). The experimental critical photon number can then be determined by looking for the measured photon number at $N_{r,\mathrm{fit}} = 1$, which gives $N_{\mathrm{c,exp}} = 2\,940(20)$.

The resulting fitted Bose-Einstein distributions are shown by the black dashed lines in the bottom panels of fig. 6.1. They agree very well with the measured distributions, especially close to the threshold point, so that the conclusion is, that the observed behaviour, despite the discrepancy in the

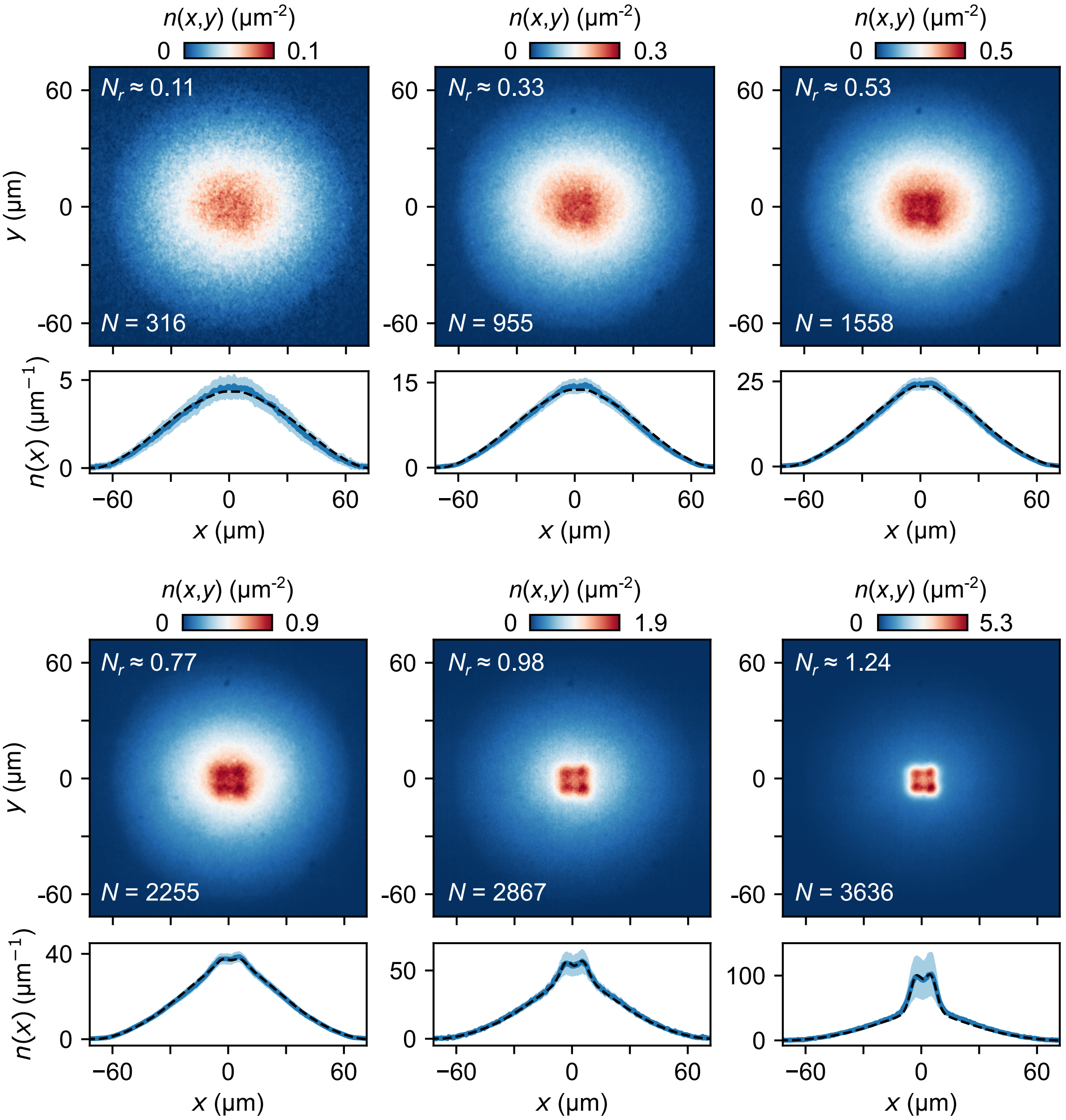

Figure 6.1: Spatial density profiles in 2D ($n(x, y)$) and integrated profiles in 1D ($n(x)$) for experimental photon numbers far below the condensation threshold at $N = 316$ ($N_r \approx 0.11$) up to within the condensed regime at $N = 3\,636$ ($N_r \approx 1.24$). Blue solid lines in the bottom panels are the average density distributions, the shaded areas give standard deviations and the black dashed lines are fits of Bose-Einstein distributions, which are set up according to sec. 5.5. The free parameter for the fitting analysis is the relative photon number N_r with the scale factor fixed to $\mathcal{A} = 0.24$.

total photon number, is adequately described by thermalisation and Bose-Einstein condensation of photons in the ground state of the four-site potential. Inspecting the fitted distributions for small relative photon numbers however reveals that there are slight deviations from the measured distributions. This observation, alongside the smaller measured critical photon number, compared to the theoretical critical number, can be attributed to the open nature of the experiment and the moderate photon thermalisation at the cutoff wavelength $\lambda_c = 584.1\,\mathrm{nm}$, which required the use of a relatively small pump beam

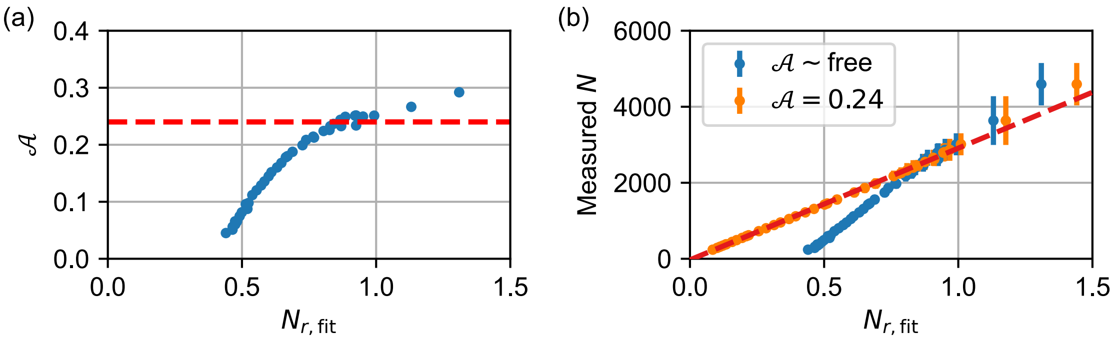

Figure 6.2: **(a)** Parameters $\mathcal{A}$ and $N_{r,\mathrm{fit}}$ obtained from fitting the theoretical (set up according to sec. 5.5) to the measured spatial photon distributions with both of the parameters as free fit parameters. $\mathcal{A}$ is smaller than 1, due to a smaller measured total photon number than the theoretical critical number. Furthermore $\mathcal{A}$ decreases with decreasing fitted relative photon number. This means that the distributions for small relative photon numbers are better matched by Bose-Einstein distributions that would correspond to higher relative photon numbers, i.e. distributions more peaked towards the low energy modes. This is then compensated by a smaller factor $\mathcal{A}$. The red, dashed horizontal line marks the scale factor at threshold, which is $\mathcal{A} = 0.24$. **(b)** Measured photon number vs. fitted relative photon number with $\mathcal{A}$ free (blue) and with $\mathcal{A}$ fixed to the threshold value (orange). By fixing the scale factor to the threshold value, a strictly linear scaling with a zero crossing at $N = 0$ is obtained.

compared to the system size (see also the discussion in sec. 2.4.8). The distributions for small relative photon numbers and the critical photon number will be further analysed in sections 6.4 and 6.5.

6.3 | Broadband Spectral Photon Distributions

For the measurement of the broadband photon spectral density distribution, the part of the cavity emission that is not used for the spatial density measurement is directed over the broadband spectrometer path, see fig. 3.1. Fig. 6.3 shows the average distributions for the same relative photon numbers as in fig. 6.1. For each measurement, the top row shows the plain distribution $n(\lambda, y)$ recorded on the ICCD camera and the bottom row gives the spectral density $n(\lambda)$, which is obtained by integration of the signal along the y-axis. As the spectral distributions are recorded together with the spatial distributions in the same pulse, the photon number obtained from the integrated and calibrated spatial distributions can be used to normalize the spectral densities accordingly. The spectra are divided by the wavelength dependent mirror transmission, $T_s(\lambda)$, such that the presented data gives the intracavity photon distributions that can be directly fitted by the previously set up Bose-Einstein distributions. Similarly to the analysis of the spatial distributions, the scale factor $\mathcal{A}$ accounts for the smaller measured critical photon number, compared to the theoretical critical number.

The spectral profiles reveal the same features as observed for the spatial profiles. A transition from a broad distribution of photons over all modes to a distribution centred around the low energy end of the spectrum is observed when the photon number is increased, until a clear peak emerges at the ground state energy when the critical photon number is surpassed. After performing the numerical fitting procedure on the experimental data, with the scale factor here set to $\mathcal{A} = 0.22$ at threshold, overall a very good agreement is found between the measured and the fitted Bose-Einstein distributions, analogously to the spatial distributions. Also, for small photon numbers, the measured distributions show a slightly larger population in the low energy modes and at the same time a slightly smaller population in the high energy modes, compared to the fits at the corresponding relative photon number. This is consistent with the observations made from the spatial distributions, i.e. the same information can be obtained from both measurements. The slight discrepancy between the scale factors at threshold

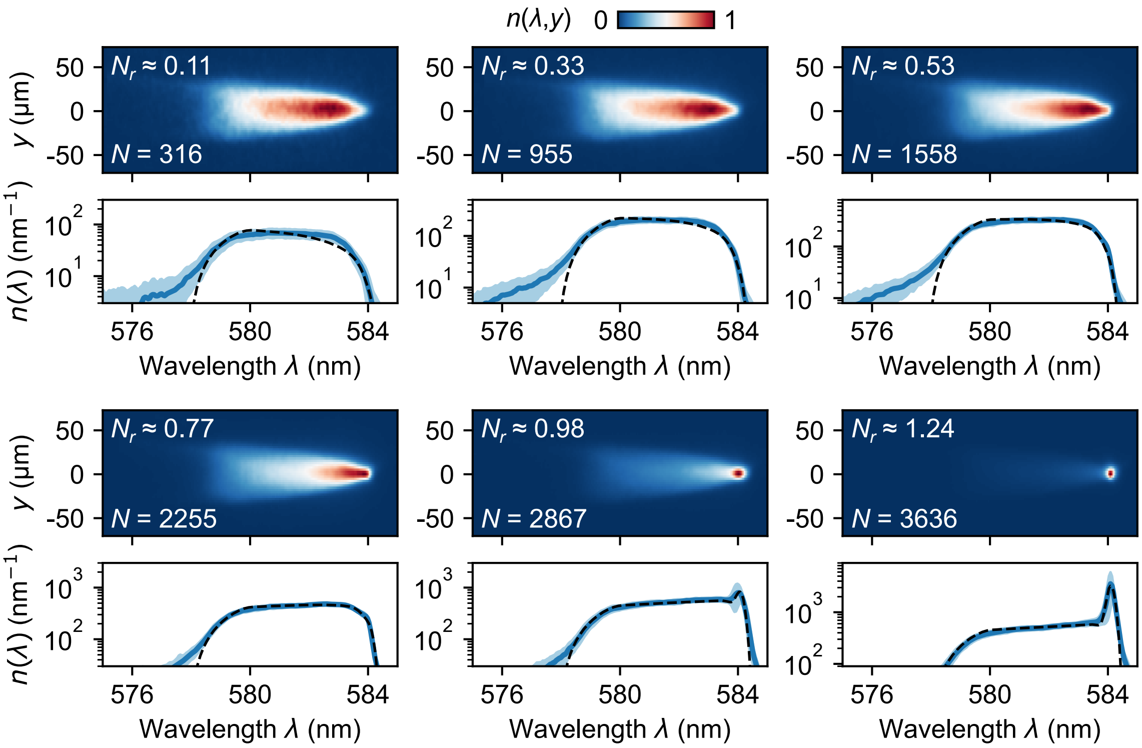

Figure 6.3: Spectral density profiles in 2D ($n(\lambda, y)$) and integrated profiles in 1D ($n(\lambda)$) for the same experimental photon numbers as in fig. 6.1. The two-dimensional profiles are peak normalized. Blue solid lines in the bottom panels are the average density distributions, the shaded areas give standard deviations and the black dashed lines are fits of Bose-Einstein distributions. The free fit parameter is the relative photon number N_r with the scale factor fixed to $\mathcal{A} = 0.22$.

for the spatial and spectral distributions could be attributed to a different background signal in the two detection paths.

6.4 | Small Photon Number Distributions

As mentioned in the previous sections, the measured threshold photon distributions show an excellent agreement with threshold Bose-Einstein distributions. However, measurements for small relative photon numbers do not agree as well (see e.g. fig. 6.3 for $N_r \approx 0.11$) but rather exhibit some deviations.

In the regime of small photon numbers ($N \ll N_c$) an approximate expression for the steady state population in mode m can be derived using eq. (2.58), which constitutes an estimate to non-equilibrium corrections to the Boltzmann distribution. In terms of the thermalisation parameter γ_m, the photon number in mode m is given by

$$n_m \approx \frac{\Gamma_{21,m}}{\Gamma_{12,m}} \frac{f_m}{1+\gamma_m} \,. \tag{6.1}$$

Analogously to the condition for a uniform chemical potential given in eq. (2.60), it is evident that if the modal overlap integral with the excitation profile f_m exhibits the same scaling with energy as $1 + \gamma_m$, the photons in the cavity will follow a Boltzmann-distribution. It was explained in the beginning of the chapter, that due to the open nature of the cavity, the pump size was adjusted to 55 µm, so that

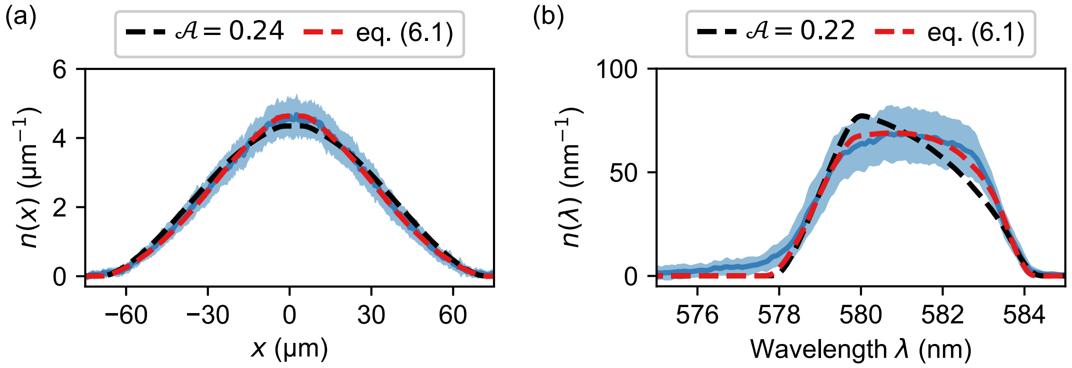

Figure 6.4: Spatial **(a)** and spectral **(b)** distributions for the measured photon number $N = 316$ ($N_r \approx 0.11$) together with fits of the Bose-Einstein distributions scaled by $\mathcal{A}$ set to the value obtained at threshold (black) and fits of the approximate small photon number distributions, constructed from eq. (6.1).

the photon distributions close to the threshold are well described by Bose-Einstein distributions. The corresponding scale factor at threshold was determined to be $\mathcal{A} \approx 0.24$ and $\mathcal{A} \approx 0.22$ for the spatial and spectral distributions respectively, which means, according to eq. (2.62), that f_m is a more steeply decreasing function of energy, compared to $1 + \gamma_m$ (the denominator of the RHS in eq. (2.62) is an increasing function of energy for $\mathcal{A} < 1$). The same conclusion for f_m should also hold for lower excitation fractions in the dye molecules and therefore it seems plausible, that the observed small photon number distributions exhibit slight deviations from ideal Boltzmann-distributions.

In order to verify if the measured distributions at the relative photon number of $N_r \approx 0.11$ are well described by eq. (6.1), a spectral and spatial density distribution is numerically calculated. The values for f_m are proportional to the overlap integrals between the Gaussian pump beam and the cavity modes, i.e. $f_m \propto F_m = \int |\psi_m(\mathbf{x})|^2\, \Pi(\mathbf{x})\, \mathrm{d}\mathbf{x}$, see also eq. (2.58). They can be calculated using the same two-dimensional mode functions as for the setup of the fit functions in sec. 5.5. The total absorption rates $\Gamma_{12,m}$, and the cavity loss rates κ_m can be directly calculated from the mode frequencies using the relations (2.46) and (2.52) and the emission rates are obtained by use of the Kennard-Stepanov relation. All other factors, that are equal for all modes, are combined into a common prefactor, which is then used as the only free fit parameter for a comparison with the experimental data. Note that this prefactor can not be directly related to the scale factor $\mathcal{A}$, because the used pump power was not measured when the data was recorded, and it can be difficult to precisely determine the experimental pump rate (cf. sec. 4.2, where the measured threshold pump power is larger than the calculated power). Therefore, only the profiles of the distributions are examined, and the actual photon densities are not analysed explicitly.

Figure 6.4 shows the measured spatial (a) and spectral (b) density profiles at the relative photon number of $N_r \approx 0.11$, together with the fitted Bose-Einstein distributions with $\mathcal{A}$ fixed to the value at threshold (black), compared to the fitted distributions obtained from the small photon number approximation in eq. (6.1) (red). As was pointed out before, the measured distributions exhibit higher densities for the low energy modes, that are mainly concentrated in the cavity centre, and simultaneously the density in high energy modes is smaller in comparison to the fitted Bose-Einstein distributions with $\mathcal{A}$ fixed at the threshold value. Looking at the fitted approximate small photon number distributions on the other hand, it is clear that they can describe the measured data quite accurately, so that eq. (6.1) seems to capture the main aspects which determine the population per mode very well. Even though the same conclusions can be drawn from both the spatial and spectral distributions, it is noticeable that the spatial fit agrees better with the measured data than the fit of the spectral signal. This is probably due

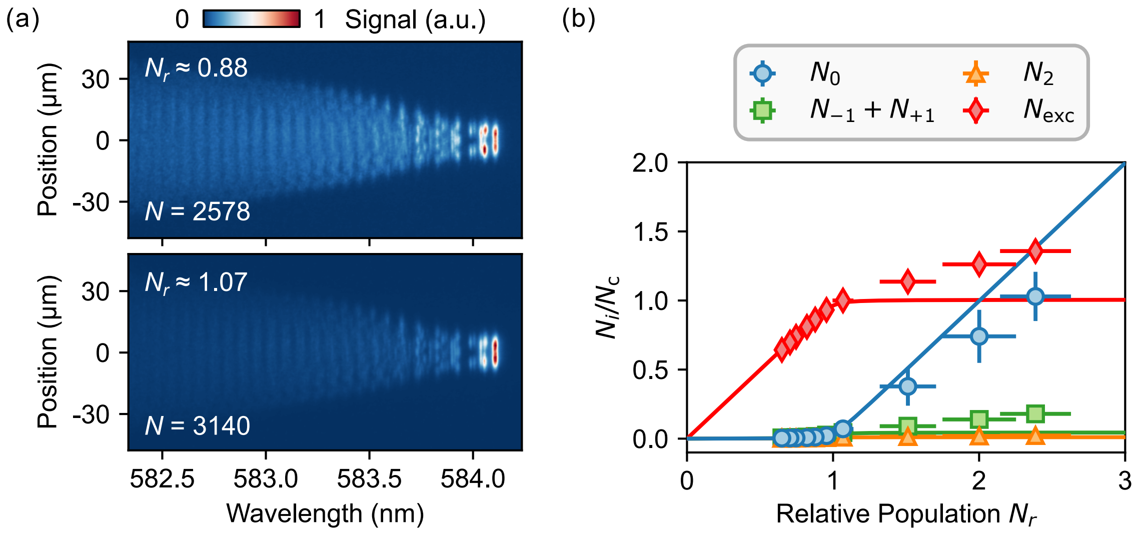

Figure 6.5: **(a)** Peak normalized spectral density distributions recorded via the Echelle spectrometer path for photon numbers below ($N = 2578$, $N_r \approx 0.88$) and above ($N = 3140$, $N_r \approx 1.07$) the condensation threshold. **(b)** Experimental relative photon populations in the low energy states and the excited states versus N_r (points) and theoretical Bose-Einstein distributed relative populations (lines). Data points for photon numbers smaller than $N_r \approx 0.6$ are not recorded due to instabilities of the cavity cutoff on a scale of ~ 30 GHz from pulse to pulse, which washes out the spectrum when averaging over many realizations and postselection of the spectra is difficult for small intensities.

to the complete overlap of all modes for the measurement of spatial density distributions, in contrast to only partially overlapping neighbouring modes for the spectral density measurements, as mentioned in sec. 3.3. Therefore, features concerning just a part of the total population are more prominently identified in the spectra while they might be absorbed in the bunched signal for the spatial density distributions.

The close agreement between the measured distributions and eq. (6.1) confirms that the approximations made in the derivation are well justified and the given simplified expression can thus be a useful tool to estimate the small photon number distributions for a given set of experimental parameters. It can be concluded that the used small pump beam indeed leads to corrections of the photon distributions far below the threshold due to the open nature of the experiment, compared to a Boltzmann distribution.

6.5 | Photon Population per State

Alongside the broadband spectral and spatial photon distributions, also high resolution spectra are recorded via the Echelle spectrometer setup (see fig. 3.1). Two of the measured distributions are shown in fig. 6.5(a) for a relative photon number slightly below ($N_r \approx 0.88$) and slightly above ($N_r \approx 1.07$) the condensation threshold. The spectrometer dispersion is sufficient to spectrally separate the low energy levels from each other, so that the relative photon population per state can be extracted.

Fig. 6.5(b) shows the individual relative populations for the four low energy states and all excited states combined (including $\psi_{\pm 1}$ and ψ_2), versus N_r. The populations of the near degenerate states $\psi_{\pm 1}$ can not be spectrally distinguished. Therefore the combined population is shown. Also plotted are the theoretical, Bose-Einstein distributed relative populations (solid lines). A good agreement between the experiment and the expected behaviour for an equilibrium system is observed, up to the critical point. While the excited states are predicted to saturate above the condensation threshold in an equilibrium system, and the ground state is supposed to absorb all additional photons added to the cavity, the observed populations show a slight deviation from this behaviour. Indeed, the ground mode takes up most of the photons added above the threshold, i.e. its population exhibits the largest slope w.r.t. the change in total photon number and therefore it can be confirmed that the photon condensate is indeed formed in the cavity ground mode. The ground mode grows with a slope smaller than unity however and the excited states' population continues to grow above threshold. When inspecting the population in the first energy level for the states $\psi_{\pm 1}$, it is clear that a significant contribution to the growth of the excited states is due to these two nearly degenerate states. This is also visible from the recorded spectral density in fig. 6.5(a) for $N_r \approx 1.07$, where the states $\psi_{\pm 1}$ are observed to be of significantly higher intensity compared to the signal of other nearby excited energy levels.

The observed contribution of photons in the first energy state in the condensed regime is also consistent with the measured spatial distributions (fig. 6.1), where a slightly increased density in the two bottom sites of the four-site lattice is observed. Judging from this, it seems probable that the state ψ_{+1}, with a maximum in density over the bottom right site (see fig. 5.3(a)), contributes more to the population in the first energy level than the state ψ_{-1}, which is the same conclusion one could come to from the shape of the measured spectrum in fig. 6.5(a) for $N_r \approx 1.07$, where the population in the first energy level is slightly peaked over the bottom right site. Following the numerical calculations, which estimated the state ψ_{+1} to be of lower energy than ψ_{-1} (cf. sec. 5.3), this also seems reasonable, as a lower energy state would be preferentially populated compared to a slightly higher energy state. The analysis of the integrated spatial and broadband spectral distributions remain essentially unaffected by this observation however, since the low energy modes completely overlap in these measurements and therefore are merged into the condensate peak, so that they cannot be distinguished.

Building on the numerical parameters for κ_m, $\Gamma_{12,m}$ and $\Gamma_{21,m}$ used in the previous section in eq. (6.1), it is also possible to obtain the full numerical steady state solution for varying pump power from the two-dimensional, spatially resolved rate equations, which were introduced in sec. 2.4.2. To set up the calculation, the resonator mode functions are calculated on a square grid with 150 µm side length with a total of 101 points along both transverse directions. With 2 628 cavity modes, which are taken into account to make up the cavity environment, this implies that a total of $2\,628 + 101^2 = 12\,829$ differential equations need to be simultaneously solved for the steady state, one for every mode and one for each grid point. A functional approach to tackling the problem proved to be a combination of first finding an approximate solution close to the steady state by integrating the initial value problem using the iterative Runge-Kutta method, and then employing an algorithm to find the roots of the resulting large set of non-linear differential equations[1]. Once the steady state is found for one set of parameters, the pump power can be incremented in small steps and a decent guess for the steady state with the updated pump power can be obtained by adding the difference between the solutions at the current and the previous steps. Providing a good estimate for the steady state is crucial to speed up convergence of the root-finding algorithm. The described method is especially efficient below the threshold, where the excitation fraction scales linearly with the pump power and there is barely any saturation in the molecules.

Fig. 6.6 shows the measured and numerically calculated relative population per state as a function of the total relative population. The numerical critical photon number is obtained by linearly extrapolating the ground state population above threshold down to zero, which gives $N_{\text{c,num}} = 3\,658$. Compared to the experimental critical photon number this is a slightly larger number, but it supports the mentioned arguments for the observed distributions with $\mathcal{A} < 1$ so far. Moreover it agrees almost exactly with the scale factor of $\mathcal{A} = 0.31$, which was determined numerically in section 2.4.8, since

---

[1] Explicitly the open source Python packages *scipy.integrate.solve_ivp* with the method 'RK23' and *scipy.optimize.root* with the method 'Krylov' were used. The approach is inspired by [150, 151].

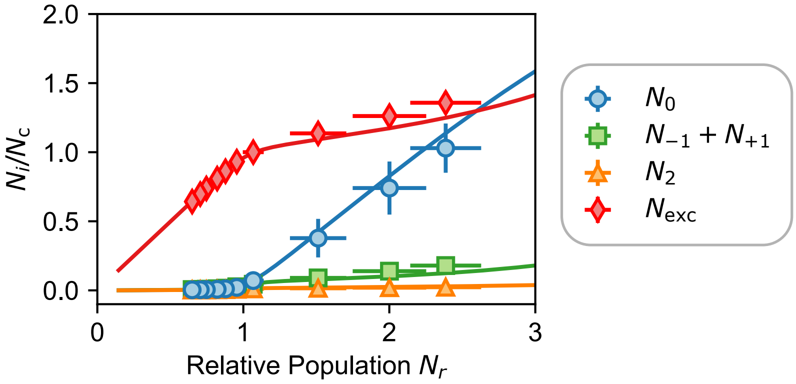

Figure 6.6: Experimental relative photon populations in the low energy states and the excited states (points) versus the total relative population N_r and numerically calculated relative populations (lines). The numerically obtained populations qualitatively match the experimental relative populations, since they also show an increase of the excited state population above the threshold to Bose-Einstein condensation, which is a consequence of the open cavity in the regime of moderate photon thermalisation.

$N_{\text{c,num}}/N_{\text{c,theo}} = 3\,658/12\,050 = 0.3$, for which a relatively close agreement between the photon distribution at threshold and a Bose-Einstein distribution would be expected. The measured data points agree very well with the numerical result up to the condensation threshold. Now, contrary to the expectation for an equilibrium system shown in fig. 6.5(b), the numerical solution also predicts a growing population of the excited states above the threshold, which comes close to the experimental observation. The reason for the incomplete saturation of the excited states is attributed to the fact, that the spatial gain profile is only locally clamped over the area covered by the ground mode and, considering that the gain coefficient in the regime of moderate thermalisation is a relatively flat function, the first excited modes experience a gain not too different from the ground mode [90]. The measured data points are not completely matched by the calculation, as the numerical result seems to underestimate the population of the antisymmetric lattice states $\psi_{\pm 1}$. The origin of these deviations could be based in the exact shape of the excitation profile on which the condensation features are heavily dependent in the regime of moderate thermalisation [152]. Nonetheless, the observed behaviour is well captured by the numerical solution, taking into account the open nature of the cavity.

Despite the decent agreement, two remarks should be made, on the reliability of the numerical solution. First of all, the numerical result can deviate from an experiment because the two perpendicular polarization components were not explicitly accounted for in the calculation. The populations were simply doubled after the computation, i.e. effectively only half of the modes, which compete for the gain in the cavity, were considered. This could imply small differences compared to the real experiment, because the polarization state of light in the cavity depends on the total photon number in a delicate way [153], and merely doubling the population calculated for one polarization component essentially assumes non-polarized photons, which does not agree with the typically observed linear polarization of photon condensates. In addition, the spontaneous emission rate out of the cavity was assumed to be the inverse free space fluorescence lifetime, $\Gamma_{\text{sp}} = 250\,\text{MHz}$, for the numerical calculation. Other experiments performed with cavity mirrors with a radius of curvature of 400 µm, corresponding to more tightly confined modes in micropotentials, proved to be modelled more accurately by a ~ 10 times smaller isotropic emission rate [83]. Hence the emission rate could be also slightly modified for the experiment presented here and it would be interesting if e.g. by investigating the ground mode population in more detail, also parameters like Γ_{sp} could be determined for this experiment.

6.6 | Phase Coherence of the Microcavity Emission

According to Landau's phenomenological theory of second-order phase transitions, a system undergoes spontaneous symmetry breaking when it reaches the critical point connecting the two phases [154]. For the BEC phase transition, this is manifested by a breaking of the gauge symmetry, such that all particles accumulated in the ground state can be collectively described by the same single-particle wave function

$$\psi(\mathbf{x},t) = \sqrt{n(\mathbf{x},t)}\, e^{i\phi(\mathbf{x},t)}\,, \tag{6.2}$$

with particle density $n(\mathbf{x},t)$ and the phase $\phi(\mathbf{x},t)$ of the wave function. Correspondingly, the ground state wave function is the order parameter of the BEC phase transition. While the amplitude of the wave function is already non-zero in the uncondensed regime, i.e. $\langle n(\mathbf{x},t)\rangle > 0$, the phase is fluctuating over space and time, which implies that $\langle \psi(\mathbf{x},t)\rangle = 0$. However, at the transition point, the system spontaneously chooses a specific phase over the entire condensate. Consequently, this leads to coherence over macroscopic distances, i.e. $\langle \psi(\mathbf{x},t)\psi(\mathbf{x}',t)\rangle \neq 0$ for $\mathbf{x}-\mathbf{x}' \rightarrow \infty$, as classified by the Penrose-Onsager criterion [155]. It is interesting to study the formation of coherence when the photon gas crosses the transition to the condensed phase [15, 91, 156, 157]. While the precise investigation of the emergence of coherence is a demanding project on its own, it is relatively simple to verify if there is macroscopic phase coherence in the light field. This information can be experimentally accessed by guiding the microcavity emission through an optical interferometer, which then leads to visible interference fringes at the interferometer output, if the light is (at least partially) coherent. By overlapping light emitted from different points in space or changing the path length and thus the time-delay between the interferometer arms, the coherence properties over space and time can be mapped out.

Fig. 6.7(a) shows a sketch of the interferometer used to to probe the mutual phase coherence between all separate sites. It is made up of multiple 50:50 non-polarizing beam splitters to realize a multi-path Mach-Zehnder interferometer, where the emission of all four lattice sites can be spatially overlapped. At first, the cavity emission is split onto four individual paths. Two of the images (B and D) are slightly shifted along the horizontal axis with respect to the other images (A and C) and guided at a small horizontal deflection angle. The interferometer is closed by bringing all four paths together, now with a small tilt and offset along the vertical direction. The relative differences between the path lengths in the interferometer are ≈ 1 cm, which corresponds to a time delay of ≈ 33 ps. This is much longer than the ~ 100 fs coherence time of thermal photons [156] and much shorter than the ~ 1 ns coherence time, which is assumed, when the condensate is formed [15]. The interferometer is therefore well suited to verify if the condensate is coherent. A focusing lens located behind the interferometer converts the lateral shifts and angular tilts into a wave vector mismatch and a lateral displacement between the paths in the detector plane. The tilt angle between two overlapping copies is $\Delta\theta \simeq 9\,\mathrm{mrad}$, which results in a wave vector mismatch of $\Delta k = 2k\sin(\Delta\theta/2)$, with $k = 2\pi/\lambda_c$. The interference fringe period in the camera plane is $d = \lambda_c/(2\sin(\Delta\theta/2)) \simeq 60\,\mu\mathrm{m}$, which corresponds to a period of $\approx 2\,\mu\mathrm{m}$ over the spatial image of the cavity emission, accounting for the 30-fold magnification of the imaging setup. Fig. 6.7(b) shows the averaged interference pattern over 123 realizations of the experiment below the condensation threshold ($N = 2578$, $N_r \approx 0.88$) and over 118 realizations above the condensation threshold ($N = 7015$, $N_r \approx 2.39$). The different number of averaged images is due to a post-selection necessary to compensate for a small frequency drift of the microcavity cutoff on a 30 GHz scale from pulse to pulse. This frequency drift causes shifts in the produced interferograms due to the uneven length of the interferometer arms. By simultaneously recording the high resolution spectrum, the interferograms can be grouped by cutoff within 10 GHz.

While the fringe visibility is close to zero for the data recorded below the condensation threshold,

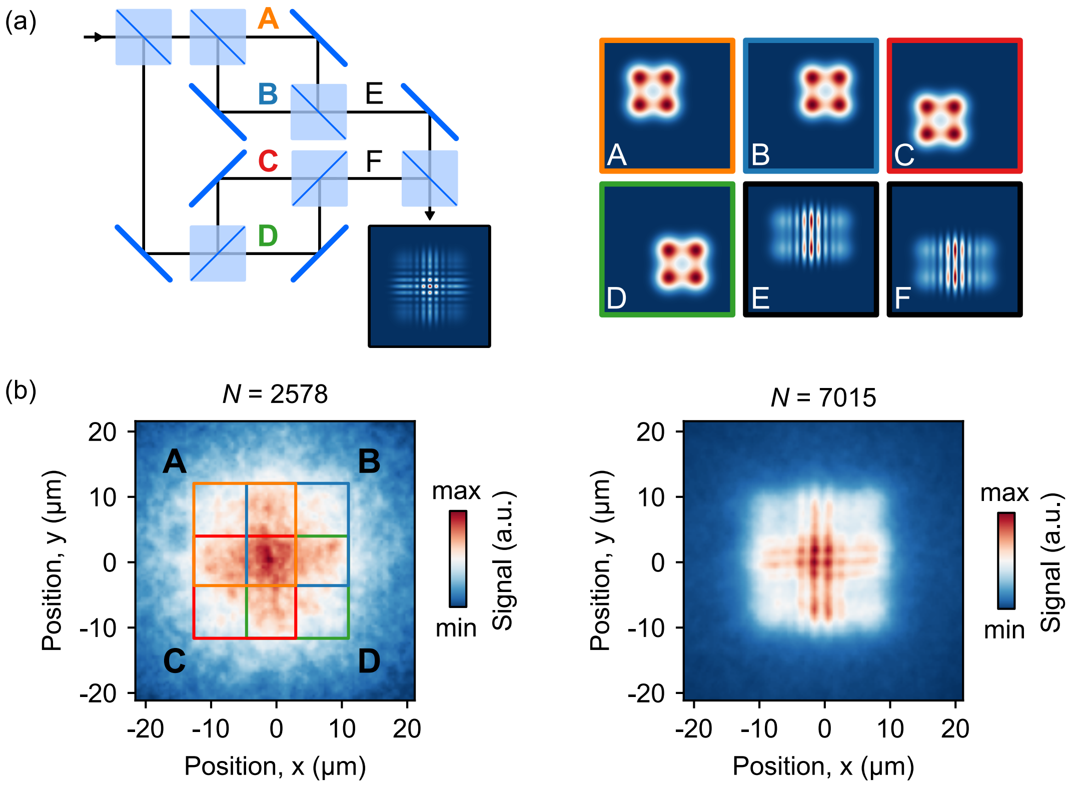

Figure 6.7: **(a)** The left panel shows a sketch of the multi-path Mach-Zehnder interferometer. The right panel illustrates what kind of pattern would be observed at the locations A-D, if a lens and a camera would be placed there. At the interferometer output, the emission from all sites is overlapped in the centre of the image and two neighbouring sites each are overlapped on the sides, which produces the chequerboard fringe pattern in the centre and a striped pattern over the outer parts. **(b)** Averaged interference patterns over many repetitive realizations of the experiment below ($N < N_c$, left) and above ($N > N_c$, right) the condensation threshold. The coloured squares in the left panel indicate how the different interferometer paths are overlapped.

clear fringes can be observed in the condensed phase. The visibility extracted from the right panel in fig. 6.7(b) is $\simeq 17\%$ along the horizontal and $\simeq 9\%$ along the vertical direction. Considering that the condensate fraction is approximately $N_0/N = 1/2.39 \approx 0.42$ (see the rightmost data point in fig. 6.5 (b)) and taking into account that the background of incoherent excited modes should only have a small overlap with the condensate, the observed visibility seems to be rather low. However, a reduced visibility could be explained by the finite spatial resolution of the imaging setup and the imperfect filtering of different cavity cutoffs. Moreover the observed population in the first excited state might be itself partially coherent, which could also produce an interference pattern and thereby reduce the overall fringe visibility [91]. The interference pattern shows no observable abrupt change in the fringe period, which gives evidence that the condensate is formed in a state described by a symmetric wave function, i.e. with the same phase in all four sites, as expected for the ground state in the potential. To conclude the discussion, it can be stated that a stable interference signal is observed after averaging over many realizations of the photon condensate, which clearly demonstrates the presence of a stable macroscopic phase over space and time in the ground state.

The experimental and numerical studies presented in this chapter give evidence for the successful realization of photon Bose-Einstein condensation in the ground state of a four-site lattice potential.

The experiments were conducted in a regime of moderate photon thermalisation, where, interestingly, both features of equilibrium and of the open nature of the cavity could be observed. The photon distributions around the critical point of condensation agreed very well with equilibrium distributions with a uniform chemical potential. For small photon numbers and in the condensed regime however, small deviations from equilibrium distributions were observed and the critical photon number in the cavity was also found to be smaller than the equilibrium critical number. Starting from the rate equations which describe all relevant processes of thermalisation, pumping and loss and therefore take into account the driven-dissipative nature of the experiment, the observations could be reasonably explained and the analytical as well as the numerical results capture most of the observed experimental features very well.

Chapter 7 | Conclusion and Perspective

In the presented work, investigations were conducted on the required pump power to reach the threshold for photon condensation and on Bose-Einstein condensation of photons in a square lattice unit cell with four sites. The main results of the studies can be summarized as follows:

- The pump threshold required to reach the critical point of photon condensation is determined by the interplay of photon cavity losses and photon absorption and emission via the dye molecules. Going to large cavity cutoff wavelengths, where cavity losses are large and the radiative contact of photons to the dye molecules is weak, the threshold pump power increases because photons are quickly lost from the cavity by mirror transmission and therefore exhibit short lifetimes. This is the regime of poor thermalisation, where the photon-cavity system operates under conditions similar to that of standard lasers. For smaller cutoff wavelengths, closer to the dye zero phonon line, where cavity losses are small and the radiative contact is strong, the threshold pump power also increases. This is because photons are quickly absorbed by the dye molecules and therefore also exhibit short lifetimes. The majority of the induced excitations by pumping the dye molecules are stored as molecular excitations and the required excitation level to reach a threshold number of photons in the cavity increases correspondingly. This is the regime of good thermalisation, where near equilibrium conditions can be realized for the photon gas. The transition point between the regimes of good and poor thermalisation, where the cavity loss rate is equal to the absorption rate, coincides with the cavity cutoff of minimum pump threshold. Good agreement between the measured and the theoretically estimated threshold power was found. The threshold pump power therefore, at least in the here realised system, provides one means to separate the regimes of good and poor thermalisation.

- Using the mirror surface structuring technique, a four-site lattice unit cell was designed and imprinted onto one of the cavity mirrors. The lattice structure was surrounded by a shallow harmonic trapping potential, so that a suitable density of states for Bose-Einstein condensation is provided. The trapping potential was numerically and experimentally characterized and decent agreement between the obtained features were found. Compared to the numerical solution of the Schrödinger equation, it was found that the measured eigenmodes of the custom shaped cavity exhibit smaller energetic spacings and the spatial mode profiles show larger peaks over the minima of the lattice sites. A qualitative explanation was motivated in terms of the penetration depth of the cavity fields into the mirror coatings, which leads to stronger localization of lower energy photons.

- A formalism based on the numerical summation of the spatial resonator mode profiles was set up, in order to calculate theoretical spatial and spectral density profiles for a given photon distribution function. For simple geometries like a harmonic oscillator potential, the mode profiles can be calculated analytically, while for more complex potentials, they can be obtained from the full numerical solution of the Schrödinger equation. With the calibrated imaging properties of the experimental setup, such as magnification or spectrometer dispersion, the method allows to prepare fit functions for a direct and system specific analysis of measured photon distributions. This is an advancement over the otherwise often used method of assuming a constant filter function of the Bose-Einstein distribution, which can not accurately account for the spatial overlap of different modes in the measurements.

- Bose-Einstein condensation of photons was investigated into the ground state of the four site trapping potential was experimentally demonstrated. The photon distributions were thoroughly characterized for different total photon numbers and good agreement with theoretical Bose-Einstein distributions was obtained, apart from the total photon number, which was found to be $\sim$1/4th of the expected equilibrium critical photon number. It was interferometrically verified that the emission of the condensate is indeed phase coherent over the entire lattice cell. The observable deviations between the measurements and theoretical expectations were attributed to the used finite size pump beam, which was required, in a regime of moderate thermalisation, to achieve a uniform chemical potential in the photon gas around the threshold point. Good agreement was found between the measurements and numerical results, taking into account the driven-dissipative character of the cavity environment. Future experiments could be carried out at smaller cavity cutoffs in the regime of good thermalisation, where the photon distributions are expected to fit better to equilibrium distributions, when larger pump sizes are used. It would be interesting to study, with a focus on the total photon number, the saturation of the excited states in the condensed regime or the small photon number distributions, how these observables change towards smaller cavity cutoffs, when the pump size is continuously increased towards a homogeneous pump profile.

An obvious extension of the present work is to study photon condensation in larger lattice systems. To reduce the amount of disorder that is probably expected to be present in larger potentials due to small inhomogeneities introduced by the surface structuring technique, an method of adjusting the potential geometry in the experiment could be used. Current projects are focused on implementing a correction setup and it was found that multiple lattice sites can be shifted into resonance by exploiting the weak temperature dependence of the dye solution's refractive index [158]. Interesting proposals would be to study Bloch-oscillations of a photon wave-packet in a one-dimensional chain of sites or to investigate the band structure and topological states in lattices with alternating tunnel couplings, as modelled by a Su-Schrieffer-Heeger type lattice configuration [159]. Such experiments could be conveniently carried out in one-dimensional lattice structures and it should therefore be possible to map out the band structure or follow the photon dynamics in momentum space. The experimental setup used in this work then would have to be modified by placing the diffraction grating in a real space plane while the camera would need to be in a momentum space plane. To investigate the band structure for larger sized, two-dimensional lattices, more elaborate setups would be required however, as realized for polariton experiments [160].

Another path to explore in the future is to add a mechanism of effective photon-photon interactions into the cavity. This could allow to investigate the formation of entangled photon states [35, 161], which are of great interest for quantum computation or communication. Such a photon-photon interaction could be achieved via optical nonlinearities in the microcavity. Investigations have shown that the dye medium itself exhibits a relatively large Kerr coefficient (third order in the electric susceptibility), however the effect is still too weak to cause any measurable signature in the photon gas [162]. A second order optical nonlinearity however can, on a single photon level, lead to a photon blockade type of interaction [163] or, on the level of many photons, to an intensity dependent phase shift for photons in the resonator [164]. Current research aims to implement an effective interaction based on a second order nonlinear optical material by exploiting cascades of frequency conversion in a slightly detuned doubly resonant cavity, similar to the configuration of an optical parametric oscillator [165]. The expected interaction strength scales with the efficiency of the frequency conversion processes, which in turn scale with the electric field amplitudes. This means that an effective interaction should be enhanced in lattice sites with tighter confinement, and therefore it would be beneficial to reduce the lateral size of the lattice sites. The technique for printing potentials based on the photoresist used in [87] could be very useful in this regard, as micropillars with diameters as small as 100 nm can be printed with this method. For the recently discovered photon condensates in semiconductor microcavities, a dimensionless interaction coefficient of $\tilde{g} = 0.0022$ was reported [21], which is three orders of magnitude larger than the interaction coefficient in the present dye microcavities. If supplemented by microstructured cavity mirrors, the semiconductor microcavity platform seems promising to allow for further studies toward entangled photon states.

Experiments in a flat bottom ring potential are pursued currently with the goal of studying the emergence of coherence in the condensate, following a rapid quench of the system through the phase transition, by ramping up the photon number in the cavity. If such a quench is fast enough, it is predicted that condensation can be locally triggered and several coherent domains with different phases are formed [166]. Upon merging of these spatially separate domains it is expected that vortices and photon currents arise.

A | Appendix

A.1 | Connection Between Pump Rate and Pump Power

In order to calculate the position dependent pump rate $\Gamma_\mathrm{p}(\mathbf{x})$, a starting point is the absorbed pump power in the dye solution, which is related to the total pump rate Γ_p by

$$P_\mathrm{abs} = \hbar\omega_\mathrm{p} \cdot \Gamma_\mathrm{p} = \hbar\omega_p \cdot \int \Gamma_\mathrm{p}(\mathbf{x})\, \rho_\mathbf{x}\, \mathrm{d}\mathbf{x}\,,$$

where ω_p is the pump frequency. For a Gaussian pump beam of width σ, one would then write

$$\Gamma_\mathrm{p}(\mathbf{x}) = \frac{\Gamma_\mathrm{p}}{\rho_\mathbf{x} \cdot 2\pi\sigma^2}\, e^{-\frac{\mathrm{x}^2}{2\sigma^2}} \quad \rightarrow \quad \int \Gamma_\mathrm{p}(\mathbf{x})\, \rho_\mathbf{x}\, \mathrm{d}\mathbf{x} = \Gamma_\mathrm{p}\,.$$

Defining the peak normalized (dimensionless) pump shape function $\Pi(\mathbf{x})$, this can be generalized for arbitrary pump profiles, i.e.

$$\Gamma_\mathrm{p}(\mathbf{x}) = \frac{\Gamma_\mathrm{p}}{\rho_\mathbf{x} \cdot \int \Pi(\mathbf{x})\, \mathrm{d}\mathbf{x}} \cdot \Pi(\mathbf{x})\,.$$

The absorbed pump power is related to the incident pump power P via Lambert-Beer's law by

$$P_\mathrm{abs} = (1 - e^{-L_0/\ell_\mathrm{abs}}) \cdot P = \eta \cdot P$$

with the cavity length L_0 and the absorption length $\ell_\mathrm{abs} = 1/\sigma_\mathrm{p}\rho \approx 40\,\mu\mathrm{m}$ (absorption cross section $\sigma_\mathrm{p} \approx 4.3 \times 10^{-20}\,\mathrm{m}^2$) of the pump light in a solution of Rhodamine 6G with a concentration of $\rho = 1\,\mathrm{mmol/l}$.

A.2 | Emission Rate into the Cavity - Fermi's Golden Rule

The starting point to calculate the spontaneous emission rate of a single emitter is Fermi's golden rule, which is given by [167]

$$R_\mathrm{spont} = \frac{2\pi}{\hbar^2} \int |\langle i|H|f\rangle|^2 \rho(\omega) L(\omega)\, \mathrm{d}\omega\,.$$

Here $|\langle i|H|f\rangle|$ is the matrix element of electric dipole transitions between initial state $|i\rangle$ and final state $|f\rangle$, $\rho(\omega)$ is the spectral density of the available final states and $L(\omega)$ is the line shape function.

The dipole transition matrix element is given by

$$|\langle i|H|f\rangle| = |E_0| \cdot |\vec{d} \cdot \vec{e}|$$

with the electric field per photon in the quantization (mode) volume V

$$|E_0| = \sqrt{\frac{\hbar\omega}{2\varepsilon_0 V}}\,,$$

the polarization direction $\vec{e}$, the dipole moment of the emitter $\vec{d}$ and the vacuum permittivity ε_0. If the emitter is in free space, an average value for the scalar product $\vec{d} \cdot \vec{e}$ has to be considered, because there are all different directions of polarizations of the vacuum field modes, which results in $|\vec{d}|/3$. The absolute value of the electric dipole moment is related to the spontaneous decay rate Γ_r by (for simplicity assume a unity quantum yield)

$$|\vec{d}|^2 = \frac{3\hbar\pi c^3 \varepsilon_0}{\omega^3}\Gamma_\mathrm{r}\,.$$

The spectral density of states in the free space volume V is $\rho(\omega) = \omega^2 V/\pi^2 c^3$, so that Fermi's golden rule yields

$$R_\mathrm{spont,free} = \frac{2\pi}{\hbar^2}\int \frac{\omega^2 V}{\pi^2 c^3}\frac{\hbar\omega}{2\varepsilon_0 V}\frac{1}{3}\frac{3\hbar\pi c^3\varepsilon_0}{\omega^3}\Gamma_\mathrm{r} \cdot L(\omega)\,\mathrm{d}\omega = \Gamma_\mathrm{r} \cdot \int L(\omega)\,\mathrm{d}\omega = \Gamma_\mathrm{r}.$$

This is exactly what would be expected, i.e. the free space spontaneous emission rate is given by the excited state spontaneous decay rate.

Assume now that the emitter is placed into a cavity with the mode density

$$\rho(\omega) = \frac{2/\pi\Delta\omega_\mathrm{cav}}{1 + \left(\frac{\omega - \omega_\mathrm{cav}}{\Delta\omega_\mathrm{cav}/2}\right)^2}\,.$$

In the case where the emission bandwidth is much narrower than the cavity linewidth $\Delta\omega_\mathrm{cav}$ and the cavity is on resonance, the integral can be evaluated using $L(\omega) = \delta(\omega - \omega_\mathrm{cav})$ and $\rho(\omega) = 2/\pi\Delta\omega_\mathrm{cav}$, i.e.

$$R_\mathrm{spont,cav} = \frac{1}{4\pi^2}\left(\frac{\lambda_\mathrm{cav}}{\tilde{n}}\right)^3 \cdot \frac{Q}{V} \cdot \Gamma_\mathrm{r} =: \frac{1}{3}F_\mathrm{P} \cdot \Gamma_\mathrm{r}\,.$$

Here the well known Purcell factor F_P was defined, which is a measure for the enhancement of spontaneous emission into the cavity mode. The cavity quality factor is given by $Q = \omega_\mathrm{cav}/\Delta\omega_\mathrm{cav}$. In the other limiting case, where the emission bandwidth is much larger than the cavity linewidth, one can use $\rho(\omega) = \delta(\omega - \omega_\mathrm{cav})$, which results in

$$R_\mathrm{spont,cav} = \frac{c}{4V}\frac{\lambda_\mathrm{cav}^2}{\tilde{n}^3} \cdot \Gamma_\mathrm{r} \cdot L(\omega_\mathrm{cav})\,.$$

Changing variables from ω to λ by $L(\omega) = \lambda^2/2\pi c \cdot L(\lambda)$ gives

$$R_{\text{spont,cav}} = \frac{1}{8\pi V}\frac{\lambda_{\text{cav}}^4}{\tilde{n}^3} \cdot \Gamma_{\text{r}} \cdot L(\lambda_{\text{cav}})\,.$$

This is equal to $\sigma_{\text{e}}(\lambda_{\text{cav}})c/\tilde{n}V$ (cf. eq. (2.44)), so one finds for the relation between the emission cross section and the line shape function

$$L(\lambda_{\text{cav}}) = \frac{8\pi\tau\tilde{n}^3}{\lambda_{\text{cav}}^4} \cdot \frac{\sigma_{\text{e}}(\lambda_{\text{cav}})c}{\tilde{n}}\,.$$

If the broad line shape function is $L(\lambda_{\text{cav}}) \approx 2/\pi\Delta\lambda_{\text{em}}$, with the emission bandwidth $\Delta\lambda_{\text{em}}$, one finds

$$R_{\text{spont,cav}} = \frac{1}{3} \cdot \frac{\Delta\lambda_{\text{cav}}}{\Delta\lambda_{\text{em}}} \cdot F_{\text{P}} \cdot \Gamma_{\text{r}}\,.$$

This is sometimes referred to as the *bad emitter* regime [168] and the enhancement of spontaneous emission in this case is smaller by a factor of $\Delta\lambda_{\text{cav}}/\Delta\lambda_{\text{em}} = \Delta\omega_{\text{cav}}/\Delta\omega_{\text{em}} \approx 2 \cdot 10^{-5}$ ($\Delta\omega_{\text{cav}} \approx 1\,\text{GHz}$, $\Delta\omega_{\text{em}} \approx 50\,\text{THz}$ for the dye-filled microcavity) compared to a narrowband emitter. Note that this result could at first sight suggest, that in fact a larger quality factor of the cavity could lead to a greater enhancement of the spontaneous emission rate. However, as F_{P} increases for larger Q, the prefactor decreases in the same fashion, so that there is no net effect on the spontaneous emission rate.

References

[1] T. H. Maiman, *Stimulated Optical Radiation in Ruby*, Nature **187**, 493–494 (1960).

[2] M. H. Anderson et al., *Observation of Bose-Einstein Condensation in a Dilute Atomic Vapor*, Science **269**, 198–201 (1995).

[3] K. B. Davis et al., *Bose-Einstein Condensation in a Gas of Sodium Atoms*, Phys. Rev. Lett. **75**, 3969–3973 (1995).

[4] A. Einstein, *Quantentheorie des Einatomigen Idealen Gases - Zweite Abhandlung*, Sitzungsberichte der Preußischen Akademie der Wissenschaften, 3–10 (1925).

[5] Bose, *Plancks Gesetz und Lichtquantenhypothese*, Zeitschrift für Physik **26**, 178–181 (1924).

[6] C. C. Bradley, C. A. Sackett and R. G. Hulet, *Bose-Einstein Condensation of Lithium: Observation of Limited Condensate Number*, Phys. Rev. Lett. **78**, 985–989 (1997).

[7] D. G. Fried et al., *Bose-Einstein Condensation of Atomic Hydrogen*, Phys. Rev. Lett. **81**, 3811–3814 (1998).

[8] S. Jochim et al., *Bose-Einstein Condensation of Molecules*, Science **302**, 2101–2103 (2003).

[9] J. Kasprzak et al., *Bose–Einstein Condensation of Exciton Polaritons*, Nature **443**, 409–414 (2006).

[10] J. Klaers, F. Vewinger and M. Weitz, *Thermalization of a Two-Dimensional Photonic Gas in a 'White Wall' Photon Box*, Nature Physics **6**, 512–515 (2010).

[11] J. Klaers et al., *Bose–Einstein Condensation of Photons in an Optical Microcavity*, Nature **468**, 545–548 (2010).

[12] J. Klaers et al., *Bose-Einstein Condensation of Paraxial Light*, Appl. Phys. B: Lasers Opt. **105**, 17–33 (2011).

[13] J. Klaers et al., *Statistical Physics of Bose-Einstein-Condensed Light in a Dye Microcavity*, Phys. Rev. Lett. **108**, 160403 (2012).

[14] J. Schmitt et al., *Observation of Grand-Canonical Number Statistics in a Photon Bose-Einstein Condensate*, Phys. Rev. Lett. **112**, 030401 (2014).

[15] J. Schmitt et al., *Spontaneous Symmetry Breaking and Phase Coherence of a Photon Bose-Einstein Condensate Coupled to a Reservoir*, Phys. Rev. Lett. **116**, 033604 (2016).

[16] T. Damm et al., *Calorimetry of a Bose–Einstein-Condensed Photon Gas*, Nature Communications **7**, 11340 (2016).

[17] J. Marelic and R. A. Nyman, *Experimental Evidence for Inhomogeneous Pumping and Energy-Dependent Effects in Photon Bose-Einstein Condensation*, Phys. Rev. A **91**, 033813 (2015).

[18] S. Greveling, K. L. Perrier and D. van Oosten, *Density Distribution of a Bose-Einstein Condensate of Photons in a Dye-Filled Microcavity*, Phys. Rev. A **98**, 013810 (2018).

[19] R. Weill et al.,
Thermalization of One-Dimensional Photon Gas and Thermal Lasers in Erbium-Doped Fibers,
Optics Express **25**, 18963 (2017).

[20] R. Weill et al., *Bose–Einstein condensation of Photons in an Erbium–Ytterbium co-doped Fiber Cavity*,
Nature Communications **10**, 747 (2019).

[21] R. C. Schofield et al.,
Bose–Einstein Condensation of Light in a Semiconductor Quantum Well Microcavity,
Nature Photonics **18**, 1083–1089 (2024).

[22] M. Pieczarka et al., *Bose–Einstein Condensation of Photons in a Vertical-Cavity Surface-Emitting laser*,
Nature Photonics **18**, 1090–1096 (2024).

[23] M. Greiner et al., *Exploring Phase Coherence in a 2D Lattice of Bose-Einstein Condensates*,
Phys. Rev. Lett. **87**, 160405 (2001).

[24] I. Bloch, *Ultracold Quantum Gases in Optical Lattices*, Nature Physics **1**, 23–30 (2005).

[25] M. Greiner et al.,
Quantum Phase Transition from a Superfluid to a Mott Insulator in a Gas of Ultracold Atoms,
Nature **415**, 39–44 (2002).

[26] M. Albiez et al.,
Direct Observation of Tunneling and Nonlinear Self-Trapping in a Single Bosonic Josephson Junction,
Phys. Rev. Lett. **95**, 010402 (2005).

[27] S. Levy et al., *The AC and DC Josephson Effects in a Bose–Einstein Condensate*,
Nature **449**, 579–583 (2007).

[28] F. S. Cataliotti et al., *Josephson Junction Arrays with Bose-Einstein Condensates*,
Science **293**, 843–846 (2001).

[29] M. Kjaergaard et al., *Superconducting Qubits: Current State of Play*,
Annual Review of Condensed Matter Physics **11**, 369–395 (2020).

[30] K. G. Lagoudakis et al., *Coherent Oscillations in an Exciton-Polariton Josephson Junction*,
Phys. Rev. Lett. **105**, 120403 (2010).

[31] M. Abbarchi et al.,
Macroscopic Quantum Self-Trapping and Josephson Oscillations of Exciton Polaritons,
Nature Physics **9**, 275–279 (2013).

[32] M. Ben Dahan et al., *Bloch Oscillations of Atoms in an Optical Potential*,
Phys. Rev. Lett. **76**, 4508–4511 (1996).

[33] J. Beierlein et al., *Bloch Oscillations of Hybrid Light-Matter Particles in a Waveguide Array*,
Advanced Optical Materials **9**, 2100126 (2021).

[34] D. Dung et al., *Variable Potentials for Thermalized Light and Coupled Condensates*,
Nature Photonics **11**, 565–569 (2017).

[35] C. Kurtscheid et al.,
Realizing Arbitrary Trapping Potentials for Light via Direct Laser Writing of Mirror Surface Profiles,
EPL (Europhys. Lett.) **130**, 54001 (2020).

[36] M. Vretenar, M. Puplauskis and J. Klaers,
Mirror Surface Nanostructuring via Laser Direct Writing—Characterization and Physical Origins,
Advanced Optical Materials **11**, 2202820 (2023).

[37] C. Kurtscheid et al., *Thermally Condensing Photons into a Coherently Split State of Light*,
Science **366**, 894–897 (2019).

[38] M. Vretenar et al., *Controllable Josephson Junction for Photon Bose-Einstein Condensates*,
Phys. Rev. Res. **3**, 023167 (2021).

[39] J. Bloch, I. Carusotto and M. Wouters,
Non-Equilibrium Bose–Einstein Condensation in Photonic Systems,
Nature Reviews Physics **4**, 470–488 (2022).

[40] J. Schmitt et al.,
Thermalization Kinetics of Light: From Laser Dynamics to Equilibrium Condensation of Photons,
Phys. Rev. A **92**, 011602 (2015).

[41] F. Schwabl, *Statistical Mechanics*, Springer Berlin Heidelberg, (2006).

[42] T. Fließbach, *Statistische Physik: Lehrbuch zur Theoretischen Physik IV*,
Springer Spektrum Berlin, Heidelberg, (2018).

[43] H.-J. Miesner et al., *Bosonic Stimulation in the Formation of a Bose-Einstein Condensate*,
Science **279**, 1005–1007 (1998).

[44] C. J. Pethick and H. Smith, *Bose–Einstein Condensation in Dilute Gases*, 2nd ed.,
Cambridge University Press, (2008).

[45] M. Planck, *Über das Gesetz der Energieverteilung im Normalspectrum*,
Annalen der Physik **309**, 553–563 (1901).

[46] A. Einstein, *Strahlungs-Emission und Absorption nach der Quantentheorie*,
Deutsche Physikalische Gesellschaft **18**, 318–323 (1916).

[47] P. Wurfel, *The Chemical Potential of Radiation*,
Journal of Physics C: Solid State Physics **15**, 3967 (1982).

[48] H. Ries and A. McEvoy, *Chemical Potential and Temperature of Light*,
Journal of Photochemistry and Photobiology A: Chemistry **59**, 11–18 (1991).

[49] J. Lakowicz, *Principles of Fluorescence Spectroscopy*, Springer New York, NY, (2006).

[50] M. Taniguchi and J. S. Lindsey, *Database of Absorption and Fluorescence Spectra of > 300 Common Compounds for Use in Photochem CAD*, Photochemistry and photobiology **94**, 290–327 (2018).

[51] J. Franck and E. G. Dymond, *Elementary Processes of Photochemical Reactions*,
Trans. Faraday Soc. **21**, 536–542 (1926).

[52] E. Condon, *A Theory of Intensity Distribution in Band Systems*, Phys. Rev. **28**, 1182–1201 (1926).

[53] A. Penzkofer, W. Falkenstein and W. Kaiser,
Vibronic Relaxation in the S1 State of Rhodamine Dye Solutions,
Chemical Physics Letters **44**, 82–87 (1976).

[54] E. A. Milne, *The Effect of Collisions on Monochromatic Radiative Equilibrium*,
Monthly Notices of the Royal Astronomical Society **88**, 493–502 (1928).

[55] C. V. Shank, *Physics of Dye Lasers*, Rev. Mod. Phys. **47**, 649–657 (1975).

[56] G. G. Stokes, *On the Change of Refrangibility of Light*,
Philosophical Transactions of the Royal Society of London Series I **142**, 463–562 (1852).

[57] E. H. Kennard, *On The Thermodynamics of Fluorescence*, Phys. Rev. **11**, 29–38 (1918).

[58] E. H. Kennard, *On the Interaction of Radiation with Matter and on Fluorescent Exciting Power*,
Phys. Rev. **28**, 672–683 (1926).

[59] B. I. Stepanov,
Universal Relation Between the Absorption Spectra and Luminescence Spectra of Complex Molecules,
Doklady Akademii Nauk, vol. 112, 839–841, Russian Academy of Sciences, (1957).

[60] B. I. Stepanov and L. P. Kazachenko, *Universal Relationship Between Absorption and Emission Spectra Taking the Solvent Effect into Account*, Journal of Applied Spectroscopy **14**, 596–601 (1971).

[61] W. van Roosbroeck and W. Shockley,
Photon-Radiative Recombination of Electrons and Holes in Germanium,
Phys. Rev. **94**, 1558–1560 (1954).

[62] D. E. McCumber, *Einstein Relations Connecting Broadband Emission and Absorption Spectra*, Phys. Rev. **136**, A954–A957 (1964).

[63] R. M. Martin and R. S. Quimby, *Experimental Evidence of the Validity of the McCumber Theory Relating Emission and Absorption for Rare-Earth Glasses*, J. Opt. Soc. Am. B **23**, 1770–1775 (2006).

[64] M. Kasha, *Phosphorescence and the Role of the Triplet State in the Electronic Excitation of Complex Molecules.*, Chemical Reviews **41**, 401–419 (1947).

[65] V. Korobov, V. Shubin and A. Chibisov, *Triplet State of Rhodamine Dyes and its Role in Production of Intermediates*, Chemical Physics Letters **45**, 498–501 (1977).

[66] A. Penzkofer and Y. Lu, *Fluorescence Quenching of Rhodamine 6G in Methanol at High Concentration*, Chemical Physics **103**, 399–405 (1986).

[67] J. P. Webb et al., *Intersystem Crossing Rate and Triplet State Lifetime for a Lasing Dye*, The Journal of Chemical Physics **53**, 4227–4229 (1970).

[68] O. G. Peterson, S. A. Tuccio and B. B. Snavely, *CW Operation of an Organic Dye Solution Laser*, Applied Physics Letters **17**, 245–247 (1970).

[69] A. Bączyński and D. Radomska, *Electronic Spectra of Dye Solutions. I. The Mirror Image Rule*, Journal of Fluorescence **2**, 175–180 (1992).

[70] M. Kasha, *Characterization of Electronic Transitions in Complex Molecules*, Discuss. Faraday Soc. **9**, 14–19 (1950).

[71] R. Kubin and A. Fletcher, *Fluorescence Quantum Yields of some Rhodamine Dyes*, Journal of Luminescence **27**, 455–462 (1982).

[72] D. Magde, G. E. Rojas and P. G. Seybold, *Solvent Dependence of the Fluorescence Lifetimes of Xanthene Dyes*, Photochemistry and Photobiology **70**, 737–744 (1999).

[73] T. J. J. Meyer and T. Markvart, *The Chemical Potential of Light in Fluorescent Solar Collectors*, Journal of Applied Physics **105**, 063110 (2009).

[74] V. DeGiorgio and M. O. Scully, *Analogy between the Laser Threshold Region and a Second-Order Phase Transition*, Phys. Rev. A **2**, 1170–1177 (1970).

[75] M. O. Scully, *Condensation of N Bosons and the Laser Phase Transition Analogy*, Phys. Rev. Lett. **82**, 3927–3931 (1999).

[76] V. V. Kocharovsky et al., *Fluctuations in Ideal and Interacting Bose–Einstein Condensates: From the Laser Phase Transition Analogy to Squeezed States and Bogoliubov Quasiparticles*, vol. 53, 291-411, Academic Press, (2006).

[77] L. Brovelli and U. Keller, *Simple Analytical Expressions for the Reflectivity and the Penetration Depth of a Bragg Mirror between Arbitrary Media*, Optics Communications **116**, 343–350 (1995).

[78] J. Klaers, *The Thermalization, Condensation and Flickering of Photons*, Journal of Physics B: Atomic, Molecular and Optical Physics **47**, 243001 (2014).

[79] A. Kavokin et al., *Microcavities*, Oxford University Press, (2017).

[80] G. Björk, H. Heitmann and Y. Yamamoto, *Spontaneous-Emission Coupling Factor and Mode Characteristics of Planar Dielectric Microcavity Lasers*, Phys. Rev. A **47**, 4451–4463 (1993).

[81] M. A. M. Marte and S. Stenholm, *Paraxial Light and Atom Optics: The optical Schrödinger Equation and Beyond*, Phys. Rev. A **56**, 2940–2953 (1997).

[82] F. Schwabl, *Quantum Mechanics*, Springer Berlin Heidelberg, (2007).

[83] B. T. Walker et al.,
Driven-Dissipative Non-Equilibrium Bose–Einstein Condensation of less than Ten Photons,
Nature Physics **14**, 1173–1177 (2018).

[84] E. Busley et al., *Compressibility and the Equation of State of an Optical Quantum Gas in a Box*,
Science **375**, 1403–1406 (2022).

[85] Christian Philipp Kurtscheid,
Bose-Einstein-Kondensation in einen photonischen Superpositionszustand,
PhD thesis, Rheinische Friedrich-Wilhelms-Universität Bonn, (2022).

[86] E. Stein and A. Pelster,
Thermodynamics of Trapped Photon Gases at Dimensional Crossover from 2D to 1D,
New Journal of Physics **24**, 023013 (2022).

[87] K. Karkihalli Umesh et al., *Dimensional Crossover in a Quantum Gas of Light*,
Nature Physics **20**, 1810–1815 (2024).

[88] P. Kirton and J. Keeling, *Nonequilibrium Model of Photon Condensation*,
Phys. Rev. Lett. **111**, 100404 (2013).

[89] P. Kirton and J. Keeling, *Thermalization and Breakdown of Thermalization in Photon Condensates*,
Phys. Rev. A **91**, 033826 (2015).

[90] J. Keeling and P. Kirton,
Spatial Dynamics, Thermalization, and Gain Clamping in a Photon Condensate,
Phys. Rev. A **93**, 013829 (2016).

[91] J. Marelic et al., *Spatiotemporal Coherence of Non-Equilibrium Multimode Photon Condensates*,
New Journal of Physics **18**, 103012 (2016).

[92] F. E. Ozturk et al., *Fluctuation Dynamics of an Open Photon Bose-Einstein Condensate*,
Phys. Rev. A **100**, 043803 (2019).

[93] F. E. Öztürk et al., *Observation of a Non-Hermitian Phase Transition in an Optical Quantum Gas*,
Science **372**, 88–91 (2021).

[94] B. T. Walker et al., *Noncritical Slowing Down of Photonic Condensation*,
Phys. Rev. Lett. **123**, 203602 (2019).

[95] A. Sazhin et al.,
Observation of Nonlinear Response and Onsager Regression in a Photon Bose-Einstein Condensate,
Nature Communications **15**, 4730 (2024).

[96] A. Siegman, *Lasers*, Sausalito: University Science Books, (1986).

[97] P. Milonni and J. Eberly, *Laser Physics*, Wiley, (2010).

[98] K. Srinivasan et al., *Cavity Q, Mode Volume, and Lasing Threshold in Small Diameter AlGaAs Microdisks with Embedded Quantum Dots*, Opt. Express **14**, 1094–1105 (2006).

[99] A. Yariv and J. Gordon, *The Laser*, Proceedings of the IEEE **51**, 4–29 (1963).

[100] B. Snavely, *Flashlamp-Excited Organic Dye Lasers*, Proceedings of the IEEE **57**, 1374–1390 (1969).

[101] O. G. Peterson et al., *Organic Dye Laser Threshold*, Journal of Applied Physics **42**, 1917–1928 (1971).

[102] E. M. Purcell, *Spontaneous Emission Probabilities at Radio Frequencies*,
Physical Review **69**, 681 (1946).

[103] D. Kleppner, *Inhibited Spontaneous Emission*, Phys. Rev. Lett. **47**, 233–236 (1981).

[104] M. P. van Exter, G. Nienhuis and J. P. Woerdman,
Two Simple Expressions for the Spontaneous Emission Factor β, Phys. Rev. A **54**, 3553–3558 (1996).

[105] P. Meystre and M. Sargent, *Elements of Quantum Optics*, Springer Berlin Heidelberg, (2007).

[106] L. Coldren, S. Corzine and M. Mashanovitch, *Diode Lasers and Photonic Integrated Circuits*,
Wiley, (2012).

[107] M. Jordan et al., *Probing Purcell Enhancement and Photon Collection Efficiency of InAs Quantum Dots at Nodes of the Cavity Electric Field*, Phys. Rev. Res. **6**, L022004 (2024).

[108] B. T. Walker et al., *Non-Stationary Statistics and Formation Jitter in Transient Photon Condensation*, Nature Communications **11**, 1390 (2020).

[109] Erik Busley, *Investigation of Paraxial Light Concentration and Homogeneously Trapped Two-Dimensional Optical Quantum Gases*, PhD thesis, Rheinische Friedrich-Wilhelms-Universität Bonn, (2022).

[110] O. Svelto, *Principles of Lasers*, Springer Science & Business Media, (2010).

[111] A. A. P. Trichet et al., *Topographic Control of Open-Access Microcavities at the Nanometer Scale*, Opt. Express **23**, 17205–17216 (2015).

[112] B. T. Walker et al., *Bespoke Mirror Fabrication for Quantum Simulation with Light in Open-Access Microcavities*, Opt. Express **29**, 10800–10810 (2021).

[113] David Dung, *Variable Potentiale für thermisches Licht und gekoppelte Photonenkondensate*, PhD thesis, Rheinische Friedrich-Wilhelms-Universität Bonn, (2018).

[114] M. Vretenar, C. Toebes and J. Klaers, *Modified Bose-Einstein Condensation in an Optical Quantum Gas*, Nature Communications **12**, 5749 (2021).

[115] M. Y. Ali, W. Hung and F. Yongqi, *A Review of Focused Ion Beam Sputtering*, International Journal of Precision Engineering and Manufacturing **11**, 157–170 (2010).

[116] G. Abadias et al., *Review Article: Stress in Thin Films and Coatings: Current Status, Challenges, and Prospects*, Journal of Vacuum Science & Technology A **36**, 020801 (2018).

[117] L. Anghinolfi et al., *Optical Properties of Uniform, Porous, Amorphous Ta2O5 Coatings on Silica: Temperature Effects*, Journal of Physics D: Applied Physics **46**, 455301 (2013).

[118] A. Paolone et al., *Effects of the Annealing of Amorphous Ta2O5 Coatings Produced by Ion Beam Sputtering Concerning the Effusion of Argon and the Chemical Composition*, Journal of Non-Crystalline Solids **557**, 120651 (2021).

[119] F. Wolf, *Microstructured Multi-Site Potentials for Quantum Gases of Light*, Master's thesis, Rheinische Friedrich-Wilhelms-Universität Bonn, (2021).

[120] D. Malacara, *Optical Shop Testing*, Wiley, (2007).

[121] C. Grossmann, H. Roos and M. Stynes, *Numerical Treatment of Partial Differential Equations*, Springer Berlin Heidelberg, (2007).

[122] H. W. Emmons, *The Numerical Solution of Partial Differential Equations*, Quarterly of Applied Mathematics **2**, 173–195 (1944).

[123] G. R. Harrison, *The Production of Diffraction Gratings: II. The Design of Echelle Gratings and Spectrographs1*, J. Opt. Soc. Am. **39**, 522–528 (1949).

[124] C. Palmer, *Diffraction Grating Handbook*, (2020).

[125] E. Hecht, *Optics*, Pearson Education, Incorporated, (2017).

[126] Rayleigh, *XXXI. Investigations in Optics, with Special Reference to the Spectroscope*, The London, Edinburgh, and Dublin Philosophical Magazine and Journal of Science **8**, 261–274 (1879).

[127] M. Pieczarka et al., *Topological Phase Transition in an All-Optical Exciton-Polariton Lattice*, Optica **8**, 1084–1091 (2021).

[128] F. Schweizer, *Anamorphic Mmagnification of Grating Sectrographs - A Reminder*, Publications of the Astronomical Society of the Pacific **91**, 149 (1979).

[129] A. Chiocchetta, A. Gambassi and I. Carusotto, *Laser Operation and Bose-Einstein Condensation: Analogies and Differences*, *Universal Themes of Bose-Einstein Condensation*, Cambridge University Press, (2017) 409–423.

[130] F. E. Öztürk et al., *Fluctuation-Dissipation Relation for a Bose-Einstein Condensate of Photons*, Phys. Rev. Lett. **130**, 033602 (2023).

[131] H. J. Hesten, R. A. Nyman and F. Mintert, *Decondensation in Nonequilibrium Photonic Condensates: When Less Is More*, Phys. Rev. Lett. **120**, 040601 (2018).

[132] A. Loirette-Pelous and J.-J. Greffet, *Photon Bose–Einstein Condensation and Lasing in Semiconductor Cavities*, Laser & Photonics Reviews **17**, 2300366 (2023).

[133] C. Z. Ning, *What is Laser Threshold?*, IEEE Journal of Selected Topics in Quantum Electronics **19**, 1503604–1503604 (2013).

[134] F. De Martini and G. R. Jacobovitz, *Anomalous Spontaneous–Stimulated-Decay Phase Transition and Zero-Threshold Laser Action in a Microscopic Cavity*, Phys. Rev. Lett. **60**, 1711–1714 (1988).

[135] H. Yokoyama, M. Suzuki and Y. Nambu, *Spontaneous Emission and Laser Oscillation Properties of Microcavities Containing a Dye Solution*, Applied Physics Letters **58**, 2598–2600 (1991).

[136] H. Yokoyama and S. D. Brorson, *Rate Equation Analysis of Microcavity Lasers*, Journal of Applied Physics **66**, 4801–4805 (1989).

[137] R. Jin et al., *Photon-Number Correlations Near the Threshold of Microcavity Lasers in the Weak-Coupling Regime*, Phys. Rev. A **49**, 4038–4042 (1994).

[138] R. A. Nyman and B. T. Walker, *Bose-Einstein Condensation of Photons from the Thermodynamic Limit to Small Photon Numbers*, Journal of Modern Optics **65**, 754–766 (2018).

[139] P. Bojarski et al., *Fluorescent Dimers of Rhodamine 6G in Concentrated Ethylene Glycol Solution*, Chemical Physics **210**, 485–499 (1996).

[140] M. Chapman and W. B. Euler, *Rhodamine 6G Structural Changes in Water/Ethanol Mixed Solvent*, Journal of Fluorescence **28**, 1431–1437 (2018).

[141] F. Bloch, *Über die Quantenmechanik der Elektronen in Kristallgittern*, Zeitschrift Für Physik **52**, 555–600 (1929).

[142] S. Simon, *The Oxford Solid State Basics*, OUP Oxford, (2013).

[143] W. H. Bragg and W. L. Bragg, *The Reflection of X-Rays by Crystals*, Proceedings of the Royal Society of London. Series A, Containing Papers of a Mathematical and Physical Character **88**, 428–438 (1913).

[144] C. Kittel, *Introduction to Solid State Physics*, 8th ed., Wiley, (2004).

[145] J. Hubbard, *Electron Correlations in Narrow Energy Bands*, Proc. Roy. Soc. (London), Ser. A **276**, 237–257 (1963).

[146] J. C. Slater and G. F. Koster, *Simplified LCAO Method for the Periodic Potential Problem*, Phys. Rev. **94**, 1498–1524 (1954).

[147] H. Deng, H. Haug and Y. Yamamoto, *Exciton-Polariton Bose-Einstein Condensation*, Rev. Mod. Phys. **82**, 1489–1537 (2010).

[148] I. H. Malitson, *Interspecimen Comparison of the Refractive Index of Fused Silica*, J. Opt. Soc. Am. **55**, 1205–1209 (1965).

[149] T. J. Bright et al., *Infrared Optical Properties of Amorphous and Nanocrystalline Ta2O5 Thin Films*, Journal of Applied Physics **114**, 083515 (2013).

[150] R. Nyman et al., *Phase Transitions of Light in a Dye-Filled Microcavity: Observations and Simulations*, Journal of Physics: Conference Series **1919**, 012006 (2021).

[151] J. Rodrigues and R. Nyman, *PyPBEC*, `https://github.com/photonbec/PyPBEC`, (2020).

[152] J. D. Rodrigues et al., *Learning the Fuzzy Phases of Small Photonic Condensates*, Phys. Rev. Lett. **126**, 150602 (2021).

[153] R. I. Moodie, P. Kirton and J. Keeling, *Polarization Dynamics in a Photon Bose-Einstein Condensate*, Phys. Rev. A **96**, 043844 (2017).

[154] P. Hohenberg and A. Krekhov, *An Introduction to the Ginzburg–Landau Theory of Phase Transitions and Nonequilibrium Patterns*, Physics Reports **572**, 1–42 (2015).

[155] O. Penrose and L. Onsager, *Bose-Einstein Condensation and Liquid Helium*, Phys. Rev. **104**, 576–584 (1956).

[156] T. Damm et al., *First-Order Spatial Coherence Measurements in a Thermalized Two-Dimensional Photonic Quantum Gas*, Nature Communications **8**, 158 (2017).

[157] W. Verstraelen and M. Wouters, *Temporal Coherence of a Photon Condensate: A Quantum Trajectory Description*, Phys. Rev. A **100**, 013804 (2019).

[158] P. Schnorrenberg, *Räumlich-Selektive Optimierung von Gitterpotentialen für Optische Quantengase*, Bachelor's thesis, Rheinische Friedrich-Wilhelms-Universität Bonn, (2022).

[159] P. St-Jean et al., *Lasing in Topological Edge States of a One-Dimensional Lattice*, Nature Photonics **11**, 651–656 (2017).

[160] C. E. Whittaker et al., *Exciton Polaritons in a Two-Dimensional Lieb Lattice with Spin-Orbit Coupling*, Phys. Rev. Lett. **120**, 097401 (2018).

[161] J. Klaers et al., *Bose-Einstein Condensation of Photons in a Microscopic Optical Resonator: Towards Photonic Lattices and Coupled Cavities*, *Laser Resonators, Microresonators, and Beam Control XV*, vol. 8600, 86000L, International Society for Optics and Photonics, (2013).

[162] F. König, *Nonlinear Kerr Media as a Future Platform for Interacting Photon Condensates*, Master's thesis, Rheinische Friedrich-Wilhelms-Universität Bonn, (2021).

[163] A. Majumdar and D. Gerace, *Single-Photon Blockade in Doubly Resonant Nanocavities with Second-Order Nonlinearity*, Phys. Rev. B **87**, 235319 (2013).

[164] L. Lugiato et al., *Bistability, Self-Pulsing and Chaos in Optical Parametric Oscillators*, Il Nuovo Cimento D **10**, 959–977 (1988).

[165] N. Wolf, *Effective Photon-Photon Interactions from Cascaded Second Order Nonlinearities*, Master's thesis, Rheinische Friedrich-Wilhelms-Universität Bonn, (2022).

[166] W. Verstraelen and M. Wouters, *Classical Critical Dynamics in Quadratically Driven Kerr Resonators*, Phys. Rev. A **101**, 043826 (2020).

[167] B. Romeira and A. Fiore, *Purcell Effect in the Stimulated and Spontaneous Emission Rates of Nanoscale Semiconductor Lasers*, IEEE Journal of Quantum Electronics **54**, 1–12 (2018).

[168] H. Kaupp et al., *Scaling Laws of the Cavity Enhancement for Nitrogen-Vacancy Centers in Diamond*, Phys. Rev. A **88**, 053812 (2013).

Danksagung

An dieser Stelle möchte ich mich herzlich bei allen Menschen bedanken, die mir bei dieser Arbeit auf viele verschiedene Arten geholfen haben.

Zu aller Erst gilt ein großer Dank Prof. Dr. Martin Weitz, für das Angebot des Forschungsthemas in seiner Arbeitsgruppe und die Betreuung während der Arbeit. Prof. Dr. Daqing Wang möchte ich für die Übernahme des Zweitgutachtens danken.

Vielen Dank an die gesamte Arbeitsgruppe für die gute Atmosphäre. Insbesondere möchte ich meinen engsten Kollegen Christian Kurtscheid, Leon Espert Miranda, Kirankumar Karkihalli Umesh und Riccardo Panico für die Hilfe und Diskussionen während und zum Abschluss der Arbeit danken. Das war wirklich eine große Freude und Unterstützung für mich. Janek Fleper und Lukas Ahlheit, die ich als neue und enge Freunde seit dem ersten Tag im Studium kennengelernt habe, möchte ich auch von Herzen danken, für die schöne gemeinsame Zeit an der Universität. Ein großer Dank gilt auch allen Kollegen in der Institutsverwaltung und der Werkstatt, die mit ihrer täglichen Mühe auch maßgeblich zum Erfolg dieser Arbeit beigetragen haben.

Zuletzt möchte ich ein herzliches Dankeschön an meine Familie und Freunde richten und vor allem an meinen Bruder, für den mentalen Beistand und ein offenes Ohr. Ohne euch wäre diese Arbeit für mich auf keinen Fall möglich gewesen.